Photoacoustics for Cardiovascular Applications

Fotoakoestiek voor cardiovasculaire toepassingen
Applications de l'imagerie photoacoustique au domaine cardiovasculaire

Sophinèse Iskander-Rizk

ISBN
978-94-028-1581-8

Lay-out
Promotie In Zicht, Arnhem

Cover
Sara Adel, Ahmed Omar, Sophinese Iskander-Rizk

Print
Ipskamp Printing, Enschede

Photoacoustics for Cardiovascular Applications

Fotoakoestiek voor cardiovasculaire toepassingen

Thesis

to obtain the degree of Doctor from the
Erasmus University Rotterdam
by command of the
rector magnificus
Prof.dr. R.C.M.E. Engels

and in accordance with the decision of the Doctorate Board.

The public defence shall be held on
Friday 5th of July 2019 at 11:30 hours

by

Sophinèse Iskander-Rizk
born in Marrakech, Morocco

Erasmus University Rotterdam

Doctoral Committee

Promotor
Prof.dr.ir. A.F.W. van der Steen

Other members
Prof.dr. N. M. S. de Groot
Prof.dr. M. Kolios
Prof.dr. G. J. Puppels

Copromotor
Dr. G. van Soest

NWO | Exacte en Natuurwetenschappen

This work was part of the *perspectief* program, instruments for Minimally Invasive Techniques, iMIT with project name Photoacoustic guidance for RF ablation of atrial Fibrillation, PARFAIT and project number 12706 which was financed by the Netherlands Organization for scientific Research (NWO)

The work presented in this thesis was carried out at the research group Biomedical Engineering of the department of cardiology, Thorax center, Erasmus Medical Center in Rotterdam, the Netherlands.

A deux âmes qui ont donné sans épargne, deux cœurs qui ont aimé sans relâche
… à vous mes chers parents, du plus profond de mon être.

Financial support by the Dutch Heart Foundation for the publication of this thesis is gratefully acknowledged

Financial support for this thesis was provided by Erasmus Medical Center, Abbott, OPOTEK LLC and InnoLas Laser GmbH

Table of Contents

Chapter 1

Introduction

Sophinese Iskander-Rizk, Antonius F.W. van der Steen, and Gijs van Soest.

Based on

"Photoacoustic imaging for guidance of interventions in cardiovascular medicine." Physics in Medicine & Biology (2019).

Cardiovascular disease (CVD) remains the number one cause of death worldwide, killing 17.7 million people in 2015 [1]. Major risk factors are lifestyle-related: smoking, obesity, diet, and lack of exercise are major determinants for the occurrence of all cardiac and vascular conditions. While most of these factors are modifiable in principle, strategies to alter unhealthy behaviour have had limited success so far.

Incidence of cardiovascular disease is progressive with age. Improved conditions, greater access to sanitation, medication and health care, and overall reduction of poverty have led to a global increase in life expectancy. This development, which overall is excellent news for public health, comes with the widespread adoption of a Western diet and lifestyle which are associated with increased cardiovascular risk. Today, more than 80% of CVD deaths occur in low- and middle-income countries [2]. Increased life expectancy is associated to a higher incidence of heart failure. This association could be explained by a heightened probability of damage to the heart caused by a survived myocardial infarction (MI; a heart attack), for instance, or poorly treated rhythm disorders. Providing adequate and affordable care to patients with CVD worldwide is a major challenge in the coming decades.

Treating all these patients with cardiac disease will depend strongly on technology; more specifically on the development of devices for minimally invasive treatment and for imaging guidance of these interventions. In minimally invasive interventions, functional catheters are advanced to the heart of the patient through a small incision in an artery or vein, to locally treat the condition. Catheter-based treatment strategies have a huge benefit for patients and the healthcare system as a whole. Our ageing population will develop an epidemic of CVD, which requires adequate treatment to maintain quality of life and prevent progression of the disease. The alternative to minimally invasive treatment in the heart is cardiac surgery. Surgery requires opening the sternum, and while this has become a routine operation, the intervention requires hospitalization for at least a week and full recovery takes about a year, including 2-3 months of inability to work.

In contrast, catheter-based treatments can frequently be done without requiring an overnight stay: patients are admitted in the morning and discharged in the evening of the same day provided there were no complications. Recovery takes days rather than months, and the patient experiences much less physical trauma than in the case of an open surgery. The advantages of minimally invasive interventions in cost, demands on the healthcare system, and lost productivity are vast, compared to surgery.

In minimally invasive treatment, interventionists have no direct line-of-sight to neither the instruments in use to treat the patient, nor to the pathology being treated. In today's practice, the most common image guidance tool is X-ray fluoroscopy or angiography. It provides a two-dimensional projection image of the heart and vessels, which are moving organs in three dimensions. Visualization of interventional catheters is frequently poor, depending on the presence of radiopaque markers on the devices. Soft tissues hardly present any image contrast and vessels are visualized by injection

of a contrast dye (angiography), which delineates the lumen but not the artery wall [3]. Moreover, the cavities of the heart can also not be effectively visualized by means of x-ray contrast. Thus, in order to meet the efficacy and safety outcomes of surgical treatment, it is crucial for the interventionist to access real-time, accurate imaging that provides functional image contrast at an adequate resolution. A real-time imaging modality is paramount to (1) support instrument navigation towards the treatment site, to (2) inform the therapeutic strategy, to (3) monitor the progress of the intervention and to (4) check its result.

The term “photoacoustic” was introduced in cardiovascular medicine in the context of laser tissue ablation, for instance in decalcification of aortic valve leaflets [4] or coronary laser angioplasty and clot removal [5-7]. It was used to indicate the photo-mechanical effects of cavitation bubble formation and the subsequent shockwave that caused tissue damage [8-10]. The acoustic signature of these violent events created by high-energy ultraviolet (excimer) or mid-infrared pulse absorption only had an intended therapeutic use. The usage of the word “photoacoustic” has evolved to imply non-destructive applications such as imaging, sensing or tissue characterization, rather than an ablation mechanism. In this thesis, we will discuss photoacoustics as an interventional imaging tool, not as a therapeutic intervention on its own. PA imaging is a hybrid imaging modality, merging advantages of optical and ultrasonic imaging. Optical absorption can provide chemically specific information, for instance on the oxygen saturation of blood. Purely optical imaging methods, however, require a coherent wavefront, which is poorly preserved due to tissue scattering, limiting the imaging depth. Photoacoustics, on the other hand, relies on both optical power and coherence of resulting acoustic waves for imaging, and thus allows one to image chemical information relatively deep (up to several centimetres) in biological structures. Deeper targets may be reached by miniaturization into endoscopic probes. Photo-acoustic (PA) imaging is unique in combining speed, compact instrumentation, and innate tissue type contrast (by optical absorption). These features lend it significant potential for interventional imaging in cardiology. The uniquely tissue-specific image contrast of photoacoustics may, one day, help in unravelling the intricate web of causes and effects in CVD.

This chapter discusses the current state of the art in PA imaging for cardiovascular applications, specifically focusing on techniques that aim at guidance of cardiac and vascular interventions. CVD comprises interrelated and frequently interacting conditions such as vascular disorders, rhythm disorders, structural heart disease, and micro-vascular disease. As a result, conditions may be multifactorial from a clinical standpoint, with sometimes unclear boundaries. In an actual patient, the location of a previous MI may become a nidus for electrical conduction disorders that result in arrhythmias [11]. Atrial fibrillation, one such arrhythmia, can cause circulating thrombi, which can lodge

themselves in the vasculature of the brain, causing an ischemic stroke [12]. This chapter is organized according to the various single-diagnostic applications for which PA imaging technologies have been developed. We summarize the advances in PA research for cardiovascular interventions, also outlining today's practical procedures where PA image guidance may fulfil an unmet need. We discuss image contrast mechanisms, proposed innovative devices, and their envisioned roles in cardiovascular interventions guidance, diagnostics and therapy. Treated single diagnostic interventions include imaging and guidance of atherosclerosis, rhythm disorders, (micro-) vascular structure treatments, and MI characterization.

1.1 Photoacoustic imaging

Prior to introducing the different applications where PA imaging and sensing can make an impact, we briefly outline the principles of the imaging modality. The PA (or optoacoustic) effect describes the generation of sound waves by light absorption. When a chromophore absorbs pulsed, or otherwise time-modulated, light, the absorbed optical energy induces a transient thermoelastic expansion, which causes a pressure (sound) wave to propagate outward from the absorber [13, 14]. This pressure wave can be recorded by an ultrasound (US) transducer and electronic data acquisition system (Figure 1.1a). Acoustic images of optical absorption can be reconstructed from the propagation delays between the light pulse and the arrival of the acoustic wave (Figure 1.1b). Tissue optics determine the intensity distribution in the image (Figure 1.1c).

Parameters affecting the pressure wave characteristics are described by the following PA governing equation:

$$p_0(z,\lambda) = \Gamma(z)\cdot\mu_a(z,\lambda)\cdot F(z,\lambda) \quad (1)$$

where p_0 denotes the source pressure generated at the chromophore location z; μ_a is the absorption coefficient of the medium; F is the local laser fluence and $\Gamma = \beta c^2/C_P$ is the Grüneisen parameter, the conversion factor of thermal to acoustic energy. In this definition, β is the thermal expansion coefficient, c is the speed of sound, and C_P is the specific heat at constant pressure. Thus, the pressure generated by photoacoustics can provide information on the tissue optical properties (through its dependency on fluence and absorption) as well as on tissue thermo-elastic efficiency properties (through the Grüneisen coefficient). Equation (1) holds under the assumption of adiabatic response, which means the pulse duration must be shorter than the acoustic transit time across the absorbing volume (stress confinement) and thermal diffusion time in that region (thermal confinement). Stress and thermal confinement are satisfied in most practical scenarios when using lasers emitting nanosecond(s) pulses.

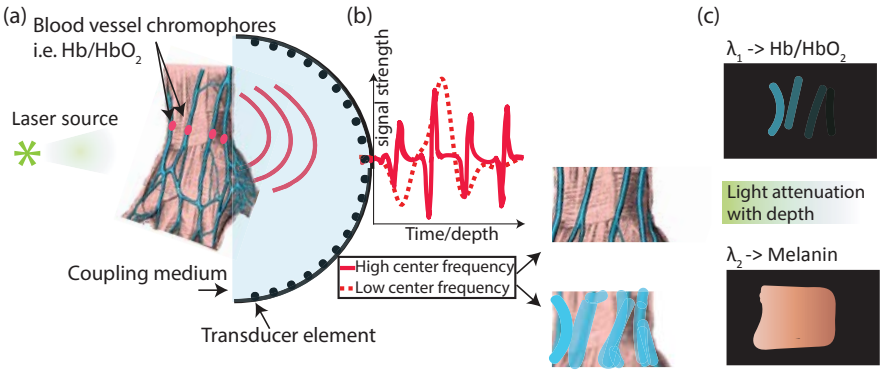

Figure 1.1 Principle of photoacoustic imaging illustrated. (a). A laser source shines on a targeted object and chromophores (e.g. blood vessels) absorb the light, thermoelastically expand, and emit acoustic waves which can be detected by an ultrasound transducer. (b) Typical received electrical signal at the transducer element and resulting image. Four cylindrical objects will display four characteristic waveforms; depending on the transducer bandwidth they may or may not be individually resolved (red solid vs. dashed). The absorber's location can be inferred from the acoustic arrival time, and signal strength is determined by the product of the absorption coefficient and light fluence at the object location. The transducer bandwidth, geometry and illumination parameters determine the resolution of the image. (c). The optical wavelength (λ) determines the image content and penetration depth. Two wavelengths may provide contrast between e.g. blood and melanin. The signal fades with light attenuation. Hb: haemoglobin; HbO_2: oxygenated haemoglobin.

Most PA applications aim at identifying and quantifying a chromophore of known $\mu_a(\lambda)$. The dependence of Eq. (1) on the optical wavelength λ indicates the possibility to perform spectroscopy to retrieve μ_a. Since there are generally several different types of absorbing tissues in a given image, spectral unmixing techniques are needed to identify tissue types and quantify absorber concentrations. In its simplest form these are linear fits of the data to a set of reference spectra, but more advanced methods use computational analyses to minimize the number of wavelengths swept [15-17]. The unknown optics of the medium under investigation, in which spatially varying scattering and absorption parameters modulate the available optical energy (fluence) and thus the generated pressure, create the need for more sophisticated spectral retrieval techniques which take account of modelled tissue optics and acoustics. With carefully designed imaging sequences and analysis algorithms, chromophore concentrations [18, 19] in the imaged specimen can be retrieved, but also other parameters in (1), such as tissue temperature changes [20, 21], tissue optical properties [22, 23], and potentially even thermodynamic properties. For these algorithms to work though, stable laser optical outputs or constant optical output power measurements are needed.

Instrumental requirements of PA imaging are application dependent, and as a result, various optical sources and ultrasonic detectors are reportedly used. The requirements on the optical source wavelength are dictated by the optical absorption spectra of the structures to be identified. The frequency content of the PA signal depends mostly on the size and shape (layer, cylinder, sphere) of a typical absorber [24]: the smaller the source, the higher the generated frequencies. As large objects absorb more energy, they also generate larger pressure amplitudes, and so the ultrasonic PA spectra of mixed-size absorbers tend to be dominated by low-frequency signals, in the order of few megahertz [24].

1.2 Atherosclerosis

Obstructive vascular disorders include coronary artery disease (CAD), peripheral artery disease (PAD), and cerebrovascular disease, which may cause arterial blockages impeding the supply of oxygen and nutrients to vital organs like the heart and the brain. CAD is a manifestation of atherosclerosis- a systemic inflammatory disease of the arteries- causing plaques formation in the innermost layer of the arterial wall. Different plaques may give rise to different symptoms. A gradual narrowing (stenosis) of the vessel by growth of a fibrous or calcific plaque will, upon exertion, cause chest pain (due to cardiac ischemia); a condition called stable CAD. Sudden onset of chest pain, or chest pain at rest, is a symptom of unstable CAD or acute coronary syndrome (ACS), which is associated with thrombus formation on plaques, mostly due to the rupture of a lipid-core lesion. The most severe form of ACS is MI. The same process in the carotid arteries (in the neck) is the most common cause of stroke. Frequently, these disastrous events are the first, and possibly lethal, symptoms arising from vascular disorders, preceded by decades of accumulation of atherosclerotic plaque. In PAD, a similar disease process can affect and even endanger the lower limbs.

Catheter-based treatment of CAD consists in the implantation of a stent: a metallic (or bioresorbable polymer) vessel prosthesis that is usually introduced on a balloon. Inflation of the balloon opens the occluded vessel and expands the stent, which now supports the reopened lesion during the healing process. This procedure is called percutaneous coronary intervention (PCI). It is the standard of care for ACS, and it is also occasionally performed for stable CAD in case of severe symptoms. Imaging of atherosclerotic plaques during PCI is of interest for precisely positioning the stent to cover all of the plaque and for identifying possible lesions that may trigger new symptoms in the future. Intravascular imaging technologies use a vascular catheter to acquire image data, and deliver much higher resolution and image contrast than non-invasive methods for coronary imaging. Recent registries, meta-analyses and randomized trials have demonstrated a reduction of the relative risk of new ACS and

even a reduction in cardiovascular mortality in patients that undergo PCI with intravascular imaging guidance, compared to angiography guidance alone [25, 26].

The current model for unstable or rupture-prone plaques hypothesizes a particular morphology and composition: an eccentric plaque with a lipid-rich necrotic core that is covered by a thin fibrous cap, which is weakened by inflammatory processes. The pathology term for this phenomenology is "thin-cap fibroatheroma" (TCFA) [27-30]. The heterogeneous nature of this plaque type provides several potential imaging markers for specific identification of these lesions by means of intravascular imaging [31].

1.2.1 Intravascular photoacoustic imaging

Plaque composition: imaging of lipids

Intravascular photoacoustic (IVPA) imaging [32] is the most intensely researched application of PA imaging in cardiology. Most groups have focused on visualization of plaque lipids, as these are generally thought to be a key component of unstable or destabilizing plaques, such as TCFA. Being an intravascular modality, IVPA requires a dedicated imaging catheter that has the ability to deliver the excitation light and receive the PA signal. In almost all implementations, the US transducer that performs this latter task, is also used for conventional intravascular ultrasound (IVUS) pulse-echo imaging; this allows for inherent co- registration between the two modalities. IVUS can visualize the artery wall structure from its luminal border, through the vessel wall, and all the way past the outer adventitial layer, enabling the assessment of plaque burden- a powerful predictor of recurring cardiovascular events. It discriminates between soft tissues and calcified lesions but cannot reliably identify soft tissue type. IVPA adds specific contrast for tissue composition, adding chemical specificity to IVUS (Figure 1.2). Together, these two imaging modalities provide a powerful way to image atherosclerotic plaque.

Multi-wavelength imaging has been the default approach in PA imaging of atherosclerotic plaque from the first studies onwards [33, 34]. These studies demonstrated useful spectroscopic tissue type contrast. The choice of excitation wavelengths was initially limited by availability in conventional laser systems [35], demonstrating the concept but yielding mostly morphological imaging with limited specificity for the relevant tissue components.

Atherosclerotic lipids can be imaged with excitation light pulses in either of two prominent absorption bands in the short-wave infrared (SWIR) spectral region, near 1.2 μm and 1.7 μm [36-38]. Both absorption bands correspond to overtones of the C—H stretch vibration which is abundant in hydrocarbons. Imaging of lipids ex vivo in the artery wall of a rabbit model of atherosclerosis provided the first positive identification of a tissue component in atherosclerosis [39]. The first in vivo imaging experiments were likewise performed in a rabbit aorta [40]. In the longer 1.7 μm wavelength window, blood scattering is sufficiently small that imaging lipids in the artery wall with luminal blood is possible [41]. Water absorption limits the imaging depth to a few millimetres [37].

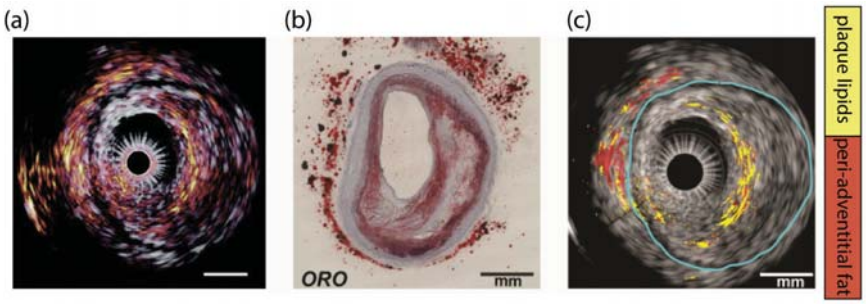

Figure 1.2 (a) IVPA image of human coronary artery ex-vivo and its corresponding Oil red O (ORO) histology evaluation (b). The PA signal in yellow-orange-red scale in (a) clearly identifies the lipid rich plaque within the vessel wall thickening. Reprinted from [47]; *Copyright © 2014 Optical Society of America.* (c) Two wavelengths, 1718 nm and 1734 nm, are sufficient to discriminate plaque lipids from peri-adventitial lipids. The blue line delineates the media/adventitia border. Reprinted from [45]; *Copyright © 2015 Optical Society of America.*

At 1.2 μm, blood optical absorption is lower but the overall optical attenuation due to scattering is strong, reducing the energy available for generating the PA signal [38].

The first IVPA images of human specimens [42] highlighted the lipid content of advanced atherosclerosis by differential imaging at wavelengths on and off the main lipid absorption peak. Follow-up analyses of the detailed absorption spectra revealed variability in the absorption spectrum of plaque lipids, and identified differences in the absorption spectra between the sterol-rich content of atherosclerosis and the fatty-acids in adipose tissue surrounding the vessel [43]. The spectral contrast is sufficiently robust to provide contrast between peri-adventitial fat and plaque lipids with only two wavelengths [44, 45] (Figure 1.2c), capitalising on slight shifts in the resonant frequency depending on the molecular conformation of the vibrating bond [46]. Using the same spectral band (1.6-1.8 μm), spectroscopic PA imaging differentiated collagenous tissue from lipids [38].

In a nutshell, the current advances in IVPA/US lipid-plaque imaging are very close to bringing this method to (pre-)clinical applications. Imaging in-vivo was demonstrated by multiple groups in various animal models (Figure 1.3a) [40, 48, 49] with different catheter designs [47, 50] through blood [51]. Specificity to human atherosclerotic plaque was shown with ex-vivo specimens [43], suggesting that the achievements shown in-vivo on animal models could potentially be achieved on humans. Emphasizing on the latter, the miniaturised catheters were also shown to be flexible enough to be navigated through swine coronaries [48] which is the closest coronary anatomy to human. Only two steps remain prior to the design of studies validating the use and advantages of the imaging method for disease monitoring and intervention guidance. These are intracoronary IVPA/US in-vivo imaging of atherosclerosis, and

demonstration of real time in-vivo *spectral* IVPA/US imaging for defined plaque feature identification.

Plaque composition imaging: other imaging targets

Inflammation is a prominent mechanism driving atherosclerosis. Interventions targeting systemic suppression of inflammatory response have been shown to reduce cardiovascular events and CV mortality [52]. Inflammation, in conjunction with lipid content, may provide important information about the event risk of an atherosclerotic plaque and consequently, could play a role in guiding device- or drug-based interventions. These features of atherosclerosis have been visualized with the aid of exogenous contrast agents, as recently reviewed in [53].

Inflammation is an innate response to injury or stress and is mediated by a complex of signalling molecules and cells. The most prominent of these inflammatory cells are macrophages, which play important roles in plaque biology, interacting with lipid transport and sequestration, efferocytosis, and weakening of connective tissue by secretion of matrix-metalloproteinases (MMP) [54]. Macrophages themselves do not exhibit a clear specific optical absorption feature. Both gold nanoparticles [55] and the FDA approved indocyanin green (ICG) dye [56], taken up by macrophage cells through endocytosis or phagocytosis were shown to enable PA imaging of macrophages in ex-vivo animal arteries. In-vivo imaging has yet to be demonstrated, which may be complicated by the choice of wavelengths, 700 nm, 750 nm and 805 nm, that are highly absorbed by haemoglobin. Tests on gold nanorods cytotoxicity showed that the particles do not particularly alter cellular viability in comparison to control cultures [57-59]. Other PA contrast agents were engineered to identify the presence/absence of metalloproteinases as a marker for plaque vulnerability. Both targeted gold nanorods [59] and MMP-sensitive activatable fluorescent probe [60] were shown to image MMP in atherosclerotic plaques ex-vivo.

Since metals are efficient optical absorbers, IVPA can also image stents as a means of evaluating stent apposition during PCI. In [61], a miniature flexible catheter capable of high-resolution PA imaging was built. The results show a better point spread function (PSF) than obtained with IVUS, with a transverse resolution of 19.6 μm (Figure 1.3b).

Experimental considerations and device design

IVPA can potentially target several of the plaque features of interest: lipids, macrophages and intraplaque haemorrhage [62]. The complementarity with IVUS adds the capability of evaluation of plaque morphology and even stiffness [63]. A combined IVUS/IVPA imaging system is clearly desirable over either modality alone. In general, intravascular images are acquired by stacking arterial cross-section images obtained at different locations while pulling back the catheter from distal to proximal in the artery. Virtually all experimental intravascular catheter prototypes presented to date

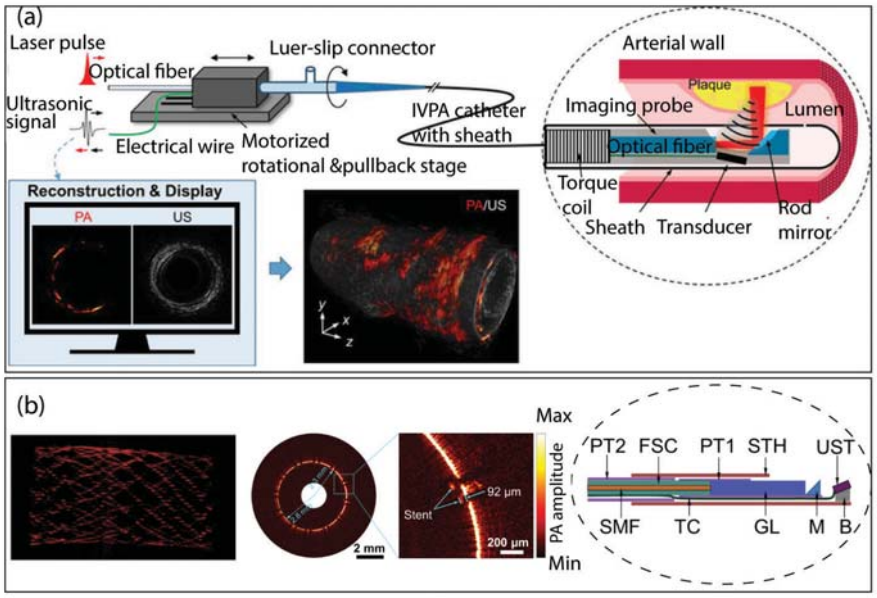

Figure 1.3 (a) In-vivo imaging of a rabbit aorta using a quasi-collinear/beam offset catheter design; reprinted from [49] , *with permission; © CC BY 4.0.* (b) Optical resolution intravascular photoacoustic imaging of a stent ex-vivo. The catheter design focuses the light through the use of a grin lens; reprinted from [61], *with permission © 2014 Bai et al.* FSC: flexible stainless steel coil; PT1: polyimide tube 1 with an inner diameter of 0.7 mm; PT2: polyimide tube 2 with an inner diameter of 0.74 mm; STH: stainless steel tube housing; UST: ultrasonic transducer; SMF, single-mode fibre; TC: transducer cable; GL: gradient-index lens; M: micro-prism; B: metal base.

are side-looking (i.e. the optical and acoustic beams are directed sideways from the catheter in the artery lumen) and image the arterial wall, using a single-element configuration that is rotated around its long axis [64]. A plastic sheath confines the rotating imaging core to provide guidewire compatibility and prevent tissue damage. In the following paragraphs, we discuss some of the key elements of an IVPA/US imaging system.

The rotary scan sequence of common IVPA implementations requires at least one laser pulse for each A-scan. Faster lasers would allow for averaging and thus improved SNR. Thus far the fastest imaging frame rate achieved was 30 fps using a 10 kHz pulse rate laser source at 1064 nm [65] ex-vivo. Parallel detection and electronic beam scanning on multiple transducers can in principle speed that up to hundreds of frames per second [66]. However, the highest frame rate demonstrated in vivo was of 20 fps [48] based on a rotary scan implementation.

The choice of all materials in the beam path, the sheath material in particular, is governed by the optical and acoustic compatibility at the operating wavelengths and frequencies. An ideal catheter sheath minimizes optical absorption, acoustic attenuation, acoustic reverberation and maximizes flexibility. The fact that lipid imaging relies on C—H absorption, a molecular bond that occurs prominently in many polymers, severely complicates this quest. Thus far, polyurethane and specific polyethylenes were found to have acceptable ultrasonic and optical transmission at wavelengths around 1.7 μm [49], but do leave room for improvement. Use of more wavelengths for access to more plaque features is likely to exacerbate this issue.

Lipids occur in tissue in different forms, such as intra-cellular and extra-cellular droplets, dispersed in cell and organelle membranes, and as cholesterol crystals. PA imaging relies on the acoustic wave emitted from an absorbing object upon thermoelastic expansion after exposure to a short laser pulse. The well-known dependence of frequency content and amplitude on the size and shape of the PA source applies, which explains why the PA signals from the lipid-rich plaques have the highest energy in the lower frequency band (< 8 MHz) [67]. Thus far, in all the IVPA/US catheter prototypes the US element was optimized for the resolution requirements set by IVUS imaging, using centre frequencies of 30 MHz and higher. Transducers of lower centre frequency (< 20 MHz) may benefit the SNR of IVPA images. These need to fit within the size required for coronary catheters (≤ 1.1 mm outer diameter). Approaches such as all-optical transduction [68] and dual-element configurations [69] may be successful in the future in achieving the required bandwidth for combined IVUS/PA imaging.

Safety of currently proposed imaging systems is necessary before any potential use on humans. An irradiation limit exists at which laser-tissue interaction becomes harmful. Maximum permissible exposure values are well established for some organs such as the skin or the eye, but are less known for other tissue types. Design for safety should take into account the illumination wavelength, the laser pulse repetition frequency (PRF), power and pulse duration, as well as the system's pullback and rotation speed. Studies on smooth muscle, macrophage and endothelial cell cultures ex-vivo demonstrated that the typical exposure levels used in IVPA imaging were not harmful to the cells (tested wavelengths: 1064 nm, 1197 nm, 1720 nm) [70]. Likewise, in vivo IVPA imaging in the iliac artery of an Ossabaw swine showed no tissue damage through post-experimental histology evaluation of imaged and control vessels [71]. It is also important to demonstrate catheter deliverability, mechanical and electrical safety.

1.2.2 Non-invasive imaging of atherosclerosis

Evaluating the progress of atherosclerosis could be non-invasively performed on carotid or other peripheral arteries. Several features of plaques are similar between the coronary and carotid arteries: thrombi, macrophage infiltration, TCFA cap thickness, lipid content, and so we can expect to see the same features in the images. The imaging

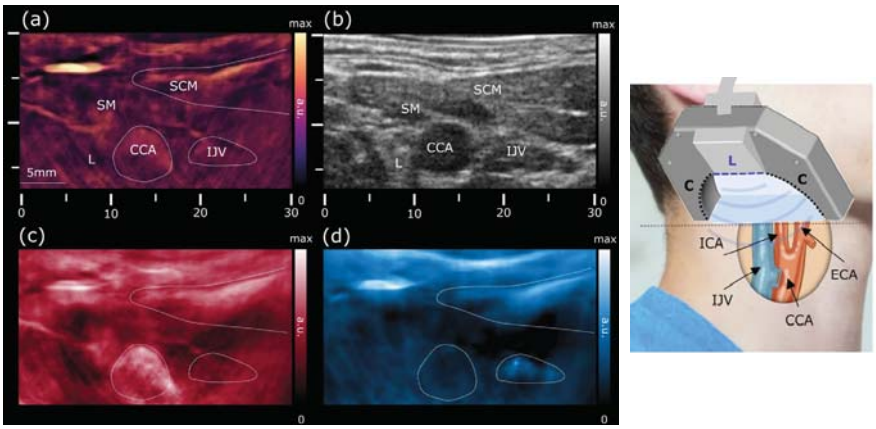

Figure 1.4 Carotid PA/US imaging configuration setup and resulting images with illumination source and acoustic transducer co-located on the neck. (a) PA image at 800 nm the main structures observed are delineated and annotated. (b) Corresponding B-mode US image. (c) Spectrally unmixed image to map oxygenated haemoglobin. (d) Spectrally unmixed image to map deoxygenated haemoglobin. SCM: sternocleidomastoid muscles; SM: strap muscle; ICA: internal carotid artery. ECA: external carotid artery; IJV: internal jugular vein; CCA: common carotid artery. Image reprinted from [74], with permission, *Copyright © 2018 The Authors, CC BY-NC-ND*.

system is fundamentally different, though: the peripheral arteries are accessible to linear-array-based US imaging. PA imaging can be performed using the same transducer, such that parallel detection on many or all elements results in a full PA image from one laser pulse (subject to SNR requirements which may encourage averaging of multiple pulses), where catheter-based imaging required at least one pulse for each A-line.

For carotid imaging, a commercially available US array is positioned on the neck of the patient to receive the PA signals from the carotid artery as well as to perform routine US (B-mode and Doppler) imaging. Light can be delivered externally, next to the transducer array on the side of the neck, which results in a longer light path (equivalent to stronger optical and acoustic attenuation paths to reach the imaging target) but allows the use of larger pulse energies (Figure 1.4) [72]. Alternatively, the illumination source can be positioned in the pharynx and/or oesophagus (Figure 1.5) [73], leading to a more efficient delivery but a smaller illuminated volume.

In-vivo PA imaging of the carotid artery and jugular vein was demonstrated on healthy volunteers [74-76]. These show the feasibility of generating sufficient signal from the target vessels, at an imaging depth of 12-15 mm through the skin layers with external illumination, showing features such as the carotid bifurcation. Use of an ultrasonic transducer centred at about 5 MHz in combination with an excitation light

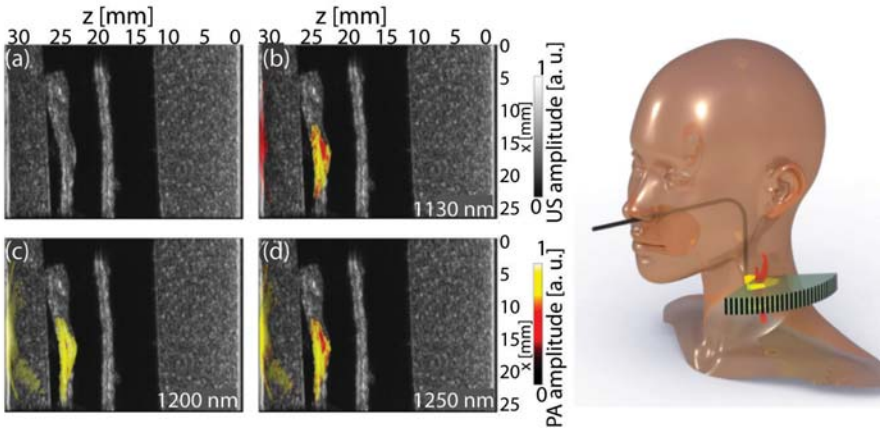

Figure 1.5 Carotid PA/US imaging configuration setup and resulting images with the illumination source located in the pharynx and the acoustic transducer on the neck. (a) US B-mode image of a neck phantom. (b) PA image at 1130 nm overlaid on US. (c) PA image at 1200 nm overlaid on US. (d) PA image at 1250 nm overlaid on US. Plaque lipids signals are located based on spectral unmixing from the surrounding collagen signals. Image reprinted from [73], with permission, © *Copyright 2018 Society of Photo-Optical Instrumentation Engineers (SPIE), CC BY 3.0*

of ~800 nm and of fluence compatible with optical exposure limits, enabled the imaging of multiple structures such as the jugular vein and the strap muscles (Figure 1.4). The chosen wavelength of 800 nm may, however, not be ideal for detecting atherosclerotic plaque, especially near the large blood pool in major vessels. Such issues may potentially be resolved by spectral unmixing. PA images at seven wavelengths between 700 and 850 nm distinguished between arterial and venous blood (Figure 1.4) [74], but could potentially also contain contrast for plaque haemorrhage. Indeed, PA signals of ex-vivo carotid plaque specimens at 808 nm correlated with intraplaque haemorrhage on histology [62]. In addition, four wavelengths between 808 and 980 nm distinguished between cholesterol crystals, porcine blood and thrombus in an ex-vivo phantom using blind source spectral unmixing methods [77]. Imaging results reported on intraplaque haemorrhage would however prove more valuable for clinical translation if demonstrated on vulnerable plaque specimen with luminal blood.

Other studies imaged atherosclerotic carotid arteries at relevant lipid differentiating wavelengths. PA imaging of a human carotid plaque specimen was mimicked using a phantom that replicated the anatomy of the neck, and explored illumination through the pharynx [73]. They showed feasibility of imaging plaque lipids at the illumination wavelengths around 1200 nm, using safe optical fluence levels ($\sim$ 12 mJ/cm^2 $<$ maximum permissible exposure for the skin of $\sim$ 55mJ/cm^2). At 1200 nm, external illumination through the skin would not be realistically achievable, due to the long optical path length and high absorption and scattering of skin. However, illumination

through the pharynx at 1200 nm should be in practice achievable (optical path of ~ 30-40 mm), though full carotid, wall-to-wall illumination and in-vivo imaging, needs to be confirmed.

1.2.3 Perspective on therapeutic interventions and risk assessment

From a cardiovascular intervention point of view, the presented research, shows that IVPA/IVUS is a strong candidate to determine optimal stent placement, stent sizing, and for pre-emptive treatment of high-risk sites during a PCI. Angiography can often identify the culprit lesion, but the addition of IVPA/US may help to define the entire implicated segment, and to identify other (asymptomatic) vulnerable plaques. This comprehensive assessment of the disease severity and extent within the artery may inform a better (pre-emptive) treatment plan. IVPA imaging can image plaque composition, while the structural information from IVUS relates them to the overall vessel wall architecture. The multimodal structural and chemical information provided by IVPA/US has the greatest potential for assessing plaque vulnerability to rupture. In clinics, other imaging technologies exist for diagnostic assessment of coronary atherosclerosis, such as IVUS, optical coherence tomography (OCT) and near-infrared spectroscopy (NIRS) [31]. However, none of these has adequate sensitivity for all plaque features that are known to correlate with vulnerability. For instance, plaque size can be determined by IVUS and lipid content can be assessed by IVPA as discussed in the previous section. Measurement of cap thickness, which requires an imaging resolution of < 50 µm, has not been demonstrated but is not beyond the realm of possibility [61, 78].

The eventual proof of clinical efficacy of an IVPA/US imaging would be a demonstration of fewer ACS cases in patients undergoing IVPA-guided PCI compared to those receiving standard of care treatment. Such trials are now emerging with IVUS, more than 20 years after the clinical introduction of the technology [26, 79]. Until then, intermediate steps would include a quantitative characterization of culprit lesions compared to non-culprit sites, and a natural history study documenting plaque changes over time. These trials with imaging endpoints will serve to define the IVPA-based treatment criteria that can be evaluated in an outcomes-based trial.

Non-invasive imaging may serve a dual role: since carotid atherosclerosis is the most common cause for stroke, detailed imaging of plaque content may improve risk assessment for patients. In today's practice, imaging technologies such as echo, X-ray CT and MRI are used for this purpose, but these are limited in their ability to predict future events and can be expensive. PA imaging may provide a highly chemically detailed image of plaque composition that may augment this picture. Another potential application may be the monitoring of systemic atherosclerotic disease status. Atherosclerosis in peripheral arteries have been identified as a proxy for coronary artery disease, and the carotid artery has been particularly popular for this purpose [80, 81].

1.3 Arrhythmias: atrial fibrillation

The field of interventional electrophysiology has only started to mature over the past 30 years, pushed by the advances made in intracardiac recording technology [82]. Interventional electrophysiology has opened the cardiac electrophysiology field to new curative approaches as opposed to traditional solutions concerned only with the management of the disease and pharmacology. Medication for atrial fibrillation consists of anti-coagulants to prevent blood clots, and decrease risks of ischemic stroke. Other prescribed drugs are anti-arrhythmic treatments to control the heart rhythm. Research aiming to elucidate heart rhythm disturbance mechanisms has led to identification, classification and better understanding of different types of arrhythmias, each requiring its own specific therapeutic approach. For instance, bradyarrhythmias (lower than optimal heart rate) are often treated with pacemaker implants. Tachycardias (fast or irregular heart rates) often require ablation: induced tissue scarring to stop aberrant conductive pathways. While treatment of tachycardias initially required an open-chest surgery, it nowadays can be performed percutaneously with minimal risk in a procedure named catheter-based ablation. Such procedures rely heavily on imaging technology and intracardiac electrophysiological mapping for guidance and treatment delivery, and this is where PA imaging can make an impact.

Atrial fibrillation is one such tachycardia. The pathology of atrial fibrillation is associated with other heart diseases such as atherosclerotic heart disease, valvular heart disease and diabetes mellitus. These comorbidities contribute to an increased mortality rate [83]. Factors predisposing the disease onset include excessive alcohol consumption, smoking, obesity, diastolic dysfunction and ageing. Symptoms affect patient's quality of life and may include chest pain, shortness of breath, palpitations, fatigue or heart failure. Atrial fibrillation is also associated with an increased risk of stroke and thromboembolism, which could be fatal. In fact, 1.5% of strokes for people between 50-59 years old, and 24% of those aged between 80-89 are associated with atrial fibrillation [83]. The prevalence of atrial fibrillation is predicted to increase, due to an ageing population and the mutually reinforcing CVD health factors discussed above [84].

1.3.1 Catheter-based ablation as a treatment for atrial fibrillation

Atrial fibrillation can nowadays be treated with catheter-based ablation, mostly obviating the complicated open surgical intervention. It is by far one of the most complicated arrhythmias to treat, with procedures often lasting longer than 4 hours. Since atrial fibrillation is the most common sustained arrhythmia, affecting 0.5% of the global population in 2010 [84], with the highest complication rates, research into PA guidance of catheter-based ablations mostly target procedures for atrial fibrillation.
Pharmaceutical management of the disease is nowadays being shown to be inferior to a curative ablation approach [85]. Ablation uses heat or extreme cold to destroy

tissue substrates responsible for cardiac rhythm disturbance. In a minimally invasive procedure, an ablation catheter as well as other electrophysiological catheters (e.g. for recording surface potentials), are inserted through the femoral vein to the atria to deliver treatment locally under fluoroscopy and echocardiography guidance. In catheter-based ablation for atrial fibrillation, the targeted ablation tissue is usually at the ostia of the pulmonary veins in the left atrium. Catheter-based ablation procedures for atrial fibrillation often last longer than 4 hours.

In catheter-based ablation procedures, technology is crucial. Long procedures under fluoroscopy guidance lead to excess exposure of radiation for the patient. Insertion of the catheter sheath from the right to the left atrium is performed under intracardiac echography (ICE) imaging. Guidance of the procedure relies on electro-anatomical maps (EAM), which identify the irregular conductive pathways and determine the regions to be treated. Such EAMs are made by tracking the position of the electrophysiology catheter as it is dragged along the atrial wall to record local electrograms. Real-time feedback on treatment evaluation relies on electrophysiological catheters (for instance, a lasso catheter) to determine cessation of conductivity as well as on sensors at the ablation catheter tip for feedback on energy delivery. These sensors comprise, among others, temperature, impedance and contact-force sensors which can indirectly predict the efficacy of conversion of the energy delivered into the tissue, with the aim to induce scarring.

Feedback on energy delivered is important. In about 4.5 % of the procedures, complications arise due to the ablation of untargeted areas: excessive energy delivery (over-ablation) reaching the oesophagus or the phrenic nerve causing serious injury to the patient [86]. Lesion size is also important because it is believed that the low interventional success rate of 60-70% is due to incomplete ablation (under-ablation), [87, 88]. Gaps between lesions, healing of tissue oedema, shallow lesions and difficulties in ectopic foci identification will lead to tissue reconduction. Thus, the cornerstones of catheter-based ablation intervention success are assumed to be (1) full and correct identification of ectopic foci (2) transmural ablation lesion formation and (3) continuous lesion formation for electrical isolation.

1.3.2 Photoacoustic imaging for ablation lesion characterization

The major complications happening during the catheter-based ablation procedures are related to control of energy delivery, and many innovative solutions aim to provide a means to better control the ablation, in order to make the catheter-based intervention faster and safer. The types of feedback provided by today's technologies (e.g. temperature, contact impedance power delivered, and duration of energy delivery settings), can only help the cardiologists to *estimate* the size of the lesions they have created. To this day, no commercially available technology provides full visualization and characterization of ablation lesions' long-term electrical functionality, and its lateral and transmural extent. It is however of extreme importance for the electrophys-

iologist to follow the progress of the tissue changes induced by the ablation process. Direct monitoring of energy delivery and visualization of its effect on tissue changes could improve the outcome of the procedure [89].

Photoacoustic tissue contrast

Initial studies of visualizing RF ablation lesions with PA imaging showed very promising results [90-92]. Governed by Eq. (1), the detected pressure as a result of transient absorption depends mainly on the tissue optical properties. To visualize lesions, it is thus necessary to determine optical wavelengths that exhibit robust absorption contrast between the lesion chromophores and the surrounding tissue. The signal contrast may visualize treated areas among healthy tissue. The first report of spectral contrast between ablated swine myocardium and healthy ventricular myocardium was shown in a PA spectroscopic study [91]. From then on, other groups have further confirmed capability of lesion visualization of cardiac tissue ex-vivo in 3D. Imaging contrast was shown for ventricular tissue [92] (Figure 1.6), with imaging depths reaching up to 6 mm [90]. Though imaging contrast was shown on swine models, the results are expected to translate to human tissue because of the optical similarity between the two, as was shown in [93]. Nonetheless, a systematic study on signal strength and contrast for different tissues and cardiac anatomic sites is still needed. Endocardium, myocardium and epicardium thickness, smoothness and orientation vary with location, affecting tissue scattering and optical propagation paths.

It is important to bear in mind that all PA studies of RF ablation lesions to date were on non-vascularized porcine tissue. Haemoglobin being the most dominant chromophore in the near infrared range could affect the lesion imaging capability, in terms of image contrast, image depth [94] and thus lesion delineation and correct identification. To avoid this potential drawback, different imaging methods were proposed. For instance, spectral correlation methods were used to differentiate background signal from lesions focussing on the peak signature of haemoglobin at 760 nm [92]. Though promising, further studies are needed to prove robustness of these methods to separating blood-generated PA signal from the lesion PA signals, as well as to quantify the effect of optical propagation and optical deposition in perfused tissue.

Clinically-approved techniques other than RF ablation include balloon-based methods, such as cryo-ablation which applies extreme cold to locally freeze the tissue [95], or laser ablation and coagulation [96]. Studies have shown the equivalence in histology of the lesions formed through different techniques [97]. One may therefore expect that the lesion-specific chromophores be the same, regardless of the method of ablation. It is important, however, to consider that the strength and polarity of the PA signal are temperature dependent, because of its dependence on the thermal expansion coefficient. This dependence may affect the generalization of results obtained with RF ablation to other energy modalities. With proper characterization, the temperature dependence of the signal could also be used for in-depth temperature

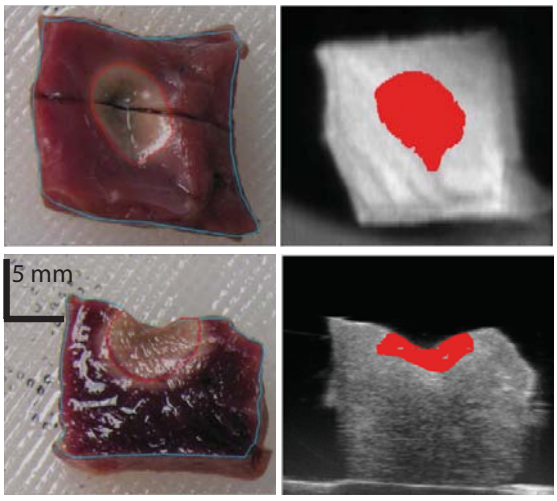

Figure 1.6 Photoacoustic imaging of ablation lesion on porcine ventricular tissue. Photographs of the imaged lesion (left panel) and their corresponding PA image (red scale) overlaid on ultrasound (grayscale). Figure reprinted from [92], *Copyright (2014), with permission from Elsevier.*

profiling [98]. Currently, cardiologists rely on a surface measurement which is of limited use with flushed catheters, or when underlying vessels cool the tissue. This is an interesting feature to explore as the tissue temperature is a key factor for the quality of the lesion that is produced.

Instrumentation development

Different imaging configurations were evaluated in published studies to date. PA monitoring of cardiac ablation needs to operate in or on the blood-filled cavities of the heart. The optical source and acoustic transducers have been realized as one integrated device [90], but separated optical and acoustic configurations have also been demonstrated [92]. Dual modality, US-PA images were formed using transducers of various centre frequencies, extending from low frequencies (< 3MHz) to high frequencies (21 MHz), but not covering the intracardiac echography (ICE) central frequency of ~6 MHz. Imaging was feasible for different imaging configurations with the transducer positioned at different locations with respect to the tissue and illumination source, showcasing that PA has the potential to image the ablation process for different cardiac locations spanning from the trans-septal wall to the pulmonary veins. Current proposed imaging solutions consist of (1) intracardiac illumination with trans-thoracic reception of PA signals and (2) a combined catheter enabling intracardiac echo, RF ablation and PA imaging; both implementations have yet to be realistically demonstrated.

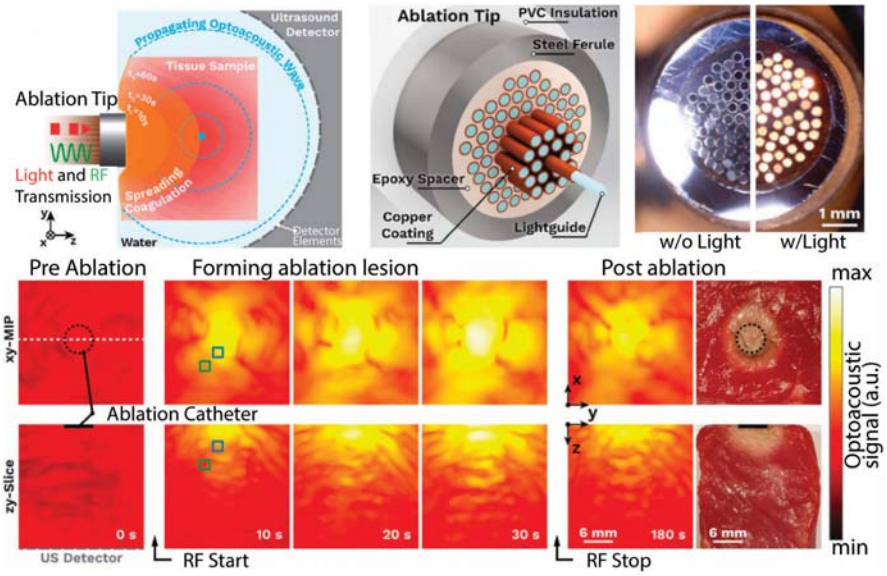

Figure 1.7. Photoacoustic-enabled ablation catheter. The optical fibres are coated with copper to deliver both RF current and laser light. Monitoring of lesion formation/ temperature profile was also achieved with the presented prototype using laser tuned to 780 nm. Image reprinted from [98], *© 2018 Optical Society of America.*

PA imaging and RF ablation with a dedicated PA-enabled ablation catheter delivers light directly at the ablation site (Figure 1.7) [98]. This configuration offers the advantage of delivering light directly at the ablated site, minimizing the impact of blood. It is also a solution that minimizes disruption to currently established procedural flow. Another design [99] consisted of an ablation catheter that enables both PA and US imaging, but it was not evaluated for tissue ablation imaging yet. From a manufacturability point of view, PA-enabled catheters at a size that is compatible with today's interventions appear to be feasible.

1.3.3 Looking forward to electrical mapping

Electrical mapping is the cornerstone of interventional electrophysiology. Not only is it the base for syndrome diagnosis and treatment planning but it also has the potential of being a tool to predict future fibrillary substrates. A popular adage claims that "atrial fibrillation begets atrial fibrillation", referring to the fact that AF, when persistent for a long period of time (> 24h), has the capability of regenerating itself after termination. This is due to the electrophysiological remodelling induced by the persistence of the AF. In such cases, cells may display shorter refractory periods than normal and may induce AF again. This mechanism means it is more difficult to restore

the sinus rhythm in prolonged AF and identification of such substrate might be of interest to the cardiologists for preventive measures. A potential advantage of imaging of electric potentials over current electrode-based potential measurements is the extension to volumetric mapping. Unravelling endocardial to epicardial signalling is indeed an important feature for current electrophysiology research [100].

In absence of native electrical contrast, PA imaging methods are not able to image cardiac electrophysiological potentials without contrast agents. However, with the use of PA sensitive contrast agents, it may be possible to visualize tissue electric potential variations. Indeed, PA signals were found to be correlated to calcium dynamics of cardiomyocytes in culture when using a dye named Arsenazo III [101]. Electrical polarization of the muscle cell being strongly related to cellular calcium flow, positions this dye-based imaging method as a contender for cardiac electrophysiological potential monitoring. In vivo application of this contrast agent will however be limited by its absorption in the visible range, which is difficult to reconcile with imaging through blood or in perfused tissue. PA voltage sensitive dyes were mostly investigated on brain tissue. Engineering of a near-infrared PA voltage-sensitive dye improved the depth at which brain tissue electrical potentials could be measured [102]. In addition to that, electrical potentials at the surface of the mouse brain were successfully disentangled from tissue hemodynamic signals using spectroscopic methods [103]. This latter feature is potentially also useful in cardiac tissue to distinguish between perfusion and contractility signalling, while the former is likely to improve imaging of cardiac signalling at depth. Today, the research on PA voltage mapping of cardiac tissue is sparse, but with the right voltage sensitive dye, electrical mapping is not beyond the limits of PA technology. Current challenges lie in the engineering of the dye's absorption wavelength and dynamics to optimize for PA spatio-temporal electric potential resolution at various depths. Needless to say that cytotoxicity and flushing mechanisms must also be taken into account.

1.4 Vascular imaging

Most of the PA imaging literature capitalizes on blood as a dominant chromophore and target contrast. Blood is the main biological absorber of light in the visible and near-infrared wavelength range and stands out from the other background biological absorbers with spectroscopic contrast between oxygenated and deoxygenated haemoglobin. An innovation in cardiovascular and intensive care medicine that capitalizes on this contrast develops a PA monitoring tool of the oxygen saturation of the venous blood in the pulmonary artery by transoesophageal illumination and acoustic reception[104, 105]. Extension of the functionality of such a device to guidance of atrial ablations is conceivable.

Microvasculature is a popular imaging target in animal models [106-108] and humans [109] through focused excitation or reception of signals. Nonetheless, high resolution imaging of vasculature works only superficially, is time consuming, and requires bulky scanners. The high resolution of such systems can be put to use for PA flow cytometry [110], demonstrated in vivo on small animal models to detect and differentiate between circulating red blood cell aggregates, white blood cell aggregates, and platelets [111, 112]. Moreover, the technique was used to monitor the formation of blood clots during surgical procedures [111, 113, 114]. Other applications are new in vitro diagnostics for various blood conditions, including the ability to sort cells with the recent feasibility demonstration of PA circulating cell focusing [115].

The main application of these techniques lies in the monitoring of intensive care unit patients. The measured parameters directly relate to blood coagulability and hemodynamic stability, which is frequently compromised in patients with acute cardiovascular disorders, and so these data may in fact inform interventions in that population in the future. Other reviews have extensively discussed PA flowmetry and its applications [110, 116, 117].

1.5 Myocardial infarct

A myocardial infarction (MI) is the name given to the irreversible damage to the myocardium by prolonged ischemia. The damage can span from loss of contractility to necrosis as a result of a coronary artery blockage. Myocardial tissue necrosis may lead in the long term to heart failure. At the onset of symptoms, the first tests to confirm a myocardial infarct are a diagnostic ECG to localize the area of infarct and a blood test to determine presence of biochemical markers for cardiomyocyte death. Medication is given to dilate the blood vessels and minimize thrombus formation. Emergency or staged PCI, usually with stent placement, are the next steps of treatment.

Several new mitigating or curative interventions are currently in development, including endovascular hypothermia application in conjunction with PCI (~ 33°C, cold saline before reperfusion), which may reduce the infarct size [118]. Several stem cell therapy approaches have also been proposed but remain highly speculative.

There are no PA imaging studies to date that show concrete translational potential in the localization and treatment guidance of myocardial infarcts in humans. Full murine heart perfusion or oxygenation [18, 119-121], which are surrogate estimates of MI features, corresponded well with measurements provided by left ventricular ejection fraction and MRI/SPECT images. However, the demonstrated non-invasive illumination, feasible through the thin murine chest wall, would not translate well to the human anatomy and size. A potential solution may include catheter-based optical delivery as was demonstrated in intra-atrial imaging. Tissue perfusion is also accessible with

myocardial contrast echography (MCE), which has been performed in patients. The PA alternative has the advantages of using endogenous contrast and conveys blood oxygenation.

PA imaging of intramyocardial stem cell injection treatment for cardiac repair following an MI [122] was explored by tracking fluorescently labelled stem cells in an animal model with multispectral optoacoustic tomography (MSOT). Stem cell therapy for MI repair being currently debatable, positions PA imaging of stem cell treatment as a promising tool for researching, understanding and improving future treatments.

Of particular interest to cardiac interventions is the capability of non-invasively monitoring patients with elevated cardiovascular risk [123]. The degree of myocardial necrosis can initially be detected through blood tests determining levels of biomarkers such as troponins or creatine phosphokinase [124]. Some of these byproducts are eliminated from the blood through the lungs in the exhaled air. In general, gas rebreathing techniques can measure and detect the presence of a multitude of biomarkers which may be related to specific diseases and/or indicate certain physiological imbalance [125, 126]. Presence of acetone, pentene, nitric oxide, carbon monoxide, isoprene, pentane and ethane (byproducts of oxidative stress and subsequent lipid peroxidation), in the breath were shown to be related to heart failure [127-130]. Non-invasive PA breath gas analysis techniques are thus a viable option to evaluate heart failure development in MI (Figure 1.8). For instance, ethylene, also shown to be related to oxidative stress, can be detected in the breath with PA gas rebreathing measurements. In fact, measures of expired ethylene using gas rebreathing measurement methods during coronary artery bypass grafting procedures and valvular surgery related well to organ reperfusion injury and to regional myocardial ischemia [131]. PA breath gas analysis can also measure cardiac output non-invasively, in real-time at rest and/or during exercise, to diagnose the severity of heart failure [132-134]. Monitoring cardiac output by the presence of specific biomarkers such as ethylene, ammonia or other products of lipid peroxidation were proven useful during surgery and at the bedside. Patented PA spectrometry-based gas rebreathing technology has been successfully commercialized by a company named Innovision in Denmark. More specifically targeted PA gas analyser, such as ethylene sensors, can be bought from Sensor Sense in the Netherlands. Compared to traditional breath analysers based on mass spectrometry PA based spectrometers are more portable and less complex.

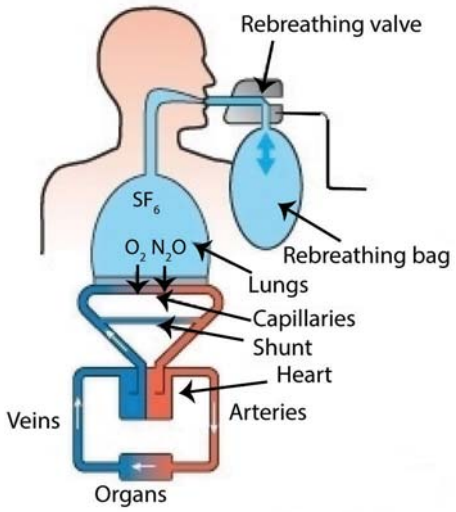

Figure 1.8 Gas rebreathing measurement principle. Concentrations of two inert gases, blood soluble and insoluble are measured to calculate cardiac output while taking into account lung volume among other correcting factors. Source: http://www.innovision.dk/Products/Innocor/, with permission. O_2: oxygen, N_2O: Nitrous oxide SF_6: Hexafluoride.

1.6 Directions for future instrumentation development

Development of a PA imaging system is a multimodal optimization problem defined by the application: light needs to reach and penetrate the targeted absorbing biological structure, while the US transducer needs to accommodate for the large bandwidth and low pressures of the PA signals, and all components need to be integrated into a clinically translatable imaging system. Translation of PA imaging to any clinical application, including cardiovascular ones, depends critically on maturity of the technology. Being intrinsically multimodal, integration to robust, stable and safe devices that are suitable for regulatory approval is challenging. Optical delivery, acoustic functionality, data acquisition and the laser source need to be integrated into one system with validated performance and functionality.

To date, most research activity in the field has focused on intravascular imaging for the characterization of atherosclerosis and for intracardiac imaging of ablation lesions. These areas depend critically on invasive imaging tools, which means that the engineering challenge includes the economics of disposable devices. Nevertheless, the proof-of-concept studies, such as those discussed in this chapter, show that there is unique tissue contrast to be attained with PA imaging which may fulfil pressing clinical needs in the guidance of cardiovascular interventions, and that stable operation is possible.

Besides the challenges of multimodal systems and device engineering, a critical component of any PA imaging system is the light source. Historically, the field has developed on the ample availability of Q-switched solid-state lasers, which provide short pulses and high energies for a limited set of wavelengths, which usually are not the optimal ones for biomedical imaging. The popularity of solid-state lasers for PA imaging has furthered the development of sophisticated tuneable optical parametric oscillator systems (OPOs) pumped by Q-switched lasers. These deliver high-energy nanosecond pulses at any wavelength (in the visible, NIR and SWIR ranges) the biological system under study happens to require for optimal image contrast. Such lasers are versatile and powerful, but also expensive, noisy, fragile and with fluctuating optical pulse energy. They are scientific instruments, and not primarily suitable as components in a clinical imaging system that needs to be robust, portable, user-friendly, and economical. In addition, the pulse repetition frequency of many OPO systems tends to be on the low side for many applications (< 100 Hz). The first target for researchers interested in clinical translation of PA technology to a clinical setting is to identify an alternative to the tuneable laser that will deliver sufficient pulsed power at the right wavelengths.

A few inroads have been made towards solving this problem. One approach has been to shift a standard wavelength using an efficient stimulated Raman scattering medium to create a light source at the relevant frequency. The combination of the fundamental Nd:YAG wavelength and $Ba(NO_3)_2$ has been used for IVPA imaging at 1197 nm [135, 136]. Many Raman active materials are available, and they may be coupled to a variety of base oscillators to access a range of biologically relevant wavelengths. Alternatively, diode lasers, pulsed or continuous wave [137], may be part of the future solutions [137, 138]. There appears to be potentially usable contrast in imaging of atherosclerosis using these devices at standard wavelengths [139, 140], and other wavelengths may become available in the future if there is sufficient demand. Light emitting diodes (LEDs) are also being explored for PA imaging, and may be a contender for some broad-illumination applications [141, 142]. Compared to most PA lasers, LEDs are safer and allow for faster imaging frame rates, because they offer low-energy (nJ to μJ) pulses at high (several kHz) repetition rates.

For diode lasers as well as LEDs, generation of sufficiently energetic pulses of pulse duration that satisfies stress confinement is nontrivial. Efficient fiber coupling of these sources can be daunting. These considerations limit the utility of diodes for many of the applications discussed in this review. With suitably optimized optical delivery, these sources may find their way into handheld devices for applications such as described in Figure 1.4. A review on the state of the art of photoacoustic imaging with laser diodes and LEDs can be found in [143].

Another prominent engineering challenge that arises in many PA applications is the relative weakness of PA signals and the lack of control over their frequency content. As laser power can only be increased to the safety limit, and tends to be an

expensive commodity, the solution must be found in sensitive detection. The ultrasound scanners and transducers that are used for PA signal detection have usually been optimized for pulse-echo imaging. Alternative transducer types such as capacitive and piezoelectric micromachined ultrasound transducers (CMUT, PMUT) and interferometric sensors are currently being investigated to accommodate both the broadband nature of the PA signals generated and for the device integration/fabrication challenges [99, 144, 145]. The power spectral density of PA signals tends to decrease with increasing frequency. Dedicated transducers with integrated amplification [146] or dedicated, high-impedance data acquisition hardware [147] aim to optimize the detection path for sensitivity. These technical hurdles must be scaled to ascertain informative, robust and affordable imaging in a clinical setting.

1.7 Thesis objective and outline

Cardiovascular interventions pose many imaging needs, which can potentially be tackled with PA imaging. This unique capability to visualize tissue contrast means that PA imaging has a role in cardiovascular medicine research, and new applications are still emerging; especially with the on-going developments of more portable, safer, and faster laser sources. PA imaging is thus a promising, ionizing-radiation-free, contrast-agent-free solution for interventional imaging in cardiovascular interventions

Since the first applications in imaging blood vessels ex vivo, PA imaging has revealed a number of unique features in cardiovascular medicine that may be put to use in the guidance and monitoring of therapy. In atherosclerosis research, PA imaging can play a major role in determining the plaque features predicting vulnerability. This is based on the capability of relating macroscopic spectroscopic PA signals to microscopic features [148] in an experimental setup and capability of using these spectral features for in-vivo identification of plaque composition. A certain number of steps are still needed, though, before taking IVPA/IVUS to the clinics, requiring more technical innovation in the catheter and imaging system, in vivo validation of the images, and corroboration on the safety of the laser exposure.

Guidance of intracardiac ablation is another application where PA imaging can provide image contrast that is not available by any other means. Imaging of ablation lesions was reported using different methods, promising to unveil the progress of lesion formation in real-time to an otherwise blind cardiologist relying on model-based theory and experience. Evaluation of lesion gaps, discontinuity and in-depth electrical mapping could help the electrophysiology research field in understanding the patterns of atrial fibrillation and determining new methods to improve procedural success rates. In order for PA imaging to contribute to RF ablation lesion imaging for atrial fibrillation, a few points remain to be researched and confirmed such as (1) Validation of PA lesion contrast on atrial tissue and for different atrial sites

(2) Robustness of PA imaging methods to localize, delineate and evaluate lesion transmurality and continuity (3) Discrimination between lesion types such as differentiation between PA signals from edema, and thrombi (4) Evaluation of imaging through blood (5) Feasibility of a realistic translatable photoacoustic imaging solution and lastly (6) Characterization of PA information on depth-resolved temperature gradients.

In this thesis, we showcase the potential of PA imaging in the future of cardiovascular research by pushing further the current achievements in PA imaging for the two aforementioned particular diseases: atherosclerosis and atrial fibrillation.

Chapter 2 characterizes the photoacoustic signal from RF ablation lesions. The imaging wavelength maximizing contrast to noise ratio is determined. A dual wavelength photoacoustic method, which allows high specificity and sensitivity discrimination of lesion extent and presence was developed.

Chapter 3 compares two designs of photoacoustic-enabled radiofrequency ablation catheters. Tissue illumination geometry effect on imaging CNR and imaging area was determined. The capability of simultaneously ablating and illuminating tissue for PA imaging was established.

Chapter 4 demonstrates imaging of RF ablation lesion progression with clinically translatable instruments. An intracardiac echography catheter was used to collect the PA signals generated while forming ultrasound images in real-time. Dual-wavelength imaging was proved to be robust against cardiac motion, blood and catheter tip artefacts.

Chapter 5 presents an IVPA/IVUS catheter design which reduces coupling damage at the rotary joint interface and improves light delivery to the tissue. The catheter was characterized for imaging capability in water and D_2O media on ex-vivo human coronary samples. Catheter sheaths were evaluated for optimum imaging.

Chapter 6 evaluates the designed IVPA/IVUS catheter in an atherosclerotic pig model in-vivo. Using the previously in-house developed IVPA/IVUS system, we show capability of imaging lipid-rich plaques in-vivo. Imaging depth and effect of luminal blood is evaluated. The images are compared to NIRS/IVUS and OCT images.

Chapter 7 explores a technique based on PA spectral imaging to super-localize PA sources of different optical absorption confounded within one same image resolution cell. By taking the difference between the PA sources radiofrequency (RF) signal's phase and performing a number of calculations across an array of transducers

(acoustic detectors) the separation distance between the sources can be recovered with high accuracy.

Chapter 8 summarizes the work presented in this thesis and discusses the future steps for pre-clinical developments.

References

[1] WHO. (2015, May 30). *Cardiovascular diseases fact sheet*. Available: http://www.who.int/mediacentre/factsheets/fs317/en/

[2] I. Abubakar, T. Tillmann, and A. Banerjee, "**Global, regional, and national age-sex specific all-cause and cause-specific mortality for 240 causes of death, 1990-2013: A systematic analysis for the global burden of disease study 2013,**" *Lancet,* vol. **385**, pp. 117-171, 2015.

[3] G. S. Mintz and G. Guagliumi, "**Intravascular imaging in coronary artery disease,**" *Lancet,* vol. **390**, pp. 793-809, Aug 19 2017.

[4] W. A. Williamson, H. T. Aretz, G. Weng, D. M. Shahian, W. M. Hamilton, M. M. Pankratov, and S. M. Shapshay, "**In vitro decalcification of aortic valve leaflets with the er:Ysgg laser, ho:Yag laser, and the cavitron ultrasound surgical aspirator,**" *Lasers in Surgery and Medicine,* vol. **13**, pp. 421-8, 1993.

[5] K. J. Quan and J. M. Hodgson, "**Comparison of tissue disruption caused by excimer and midinfrared lasers in clinical simulation,**" *Catheterization and Cardiovascular Diagnosis,* vol. **38**, pp. 50-5, May 1996.

[6] O. Topaz, M. McIvor, G. W. Stone, M. W. Krucoff, E. C. Perin, A. E. Foschi, J. Sutton, R. Nair, and E. deMarchena, "**Acute results, complications, and effect of lesion characteristics on outcome with the solid-state, pulsed-wave, mid-infrared laser angioplasty system: Final multicenter registry report. Holmium:Yag laser multicenter investigators,**" *Lasers in Surgery and Medicine,* vol. **22**, pp. 228-39, 1998.

[7] O. Topaz, A. J. Minisi, C. Morris, P. K. Mohanty, and M. E. Carr, "**Photoacoustic fibrinolysis: Pulsed-wave, mid-infrared laser-clot interaction,**" *Journal of Thrombosis and Thrombolysis,* vol. **3**, pp. 209-214, September 01 1996.

[8] T. G. van Leeuwen, J. H. Meertens, E. Velema, M. J. Post, and C. Borst, "**Intraluminal vapor bubble induced by excimer laser pulse causes microsecond arterial dilation and invagination leading to extensive wall damage in the rabbit,**" *Circulation,* vol. **87**, pp. 1258-63, Apr 1993.

[9] J. M. Isner, J. G. Pickering, and M. Mosseri, "**Laser-induced dissections: Pathogenesis and implications for therapy,**" *Journal of the American College of Cardiology,* vol. **19**, pp. 1619-1621, 1992.

[10] T. G. van Leeuwen, L. van Erven, J. H. Meertens, M. Motamedi, M. J. Post, and C. Borst, "**Origin of arterial wall dissections induced by pulsed excimer and mid-infrared laser ablation in the pig,**" *Journal of the American College of Cardiology,* vol. **19**, pp. 1610-1618, 1992.

[11] S. D. Roes, C. J. W. Borleffs, R. J. van der Geest, J. J. M. Westenberg, N. A. Marsan, T. A. M. Kaandorp, J. H. C. Reiber, K. Zeppenfeld, H. J. Lamb, A. de Roos, M. J. Schalij, and J. J. Bax, "**Infarct tissue heterogeneity assessed with contrast-enhanced mri predicts spontaneous ventricular arrhythmia in patients with ischemic cardiomyopathy and implantable cardioverter-defibrillator,**" *Circulation: Cardiovascular Imaging,* vol. **2**, p. 183, 2009.

[12] P. A. Wolf, T. R. Dawber, H. E. Thomas, Jr., and W. B. Kannel, "**Epidemiologic assessment of chronic atrial fibrillation and risk of stroke: The framingham study,**" *Neurology,* vol. **28**, pp. 973-7, Oct 1978.

[13] L. V. Wang, ***Photoacoustic imaging and spectroscopy***: CRC press, 2009.

[14] S. Manohar and D. Razansky, "**Photoacoustics: A historical review,**" *Advances in Optics and Photonics,* vol. **8**, pp. 586-617, Dec 31 2016.

[15] D. Razansky, C. Vinegoni, and V. Ntziachristos, "**Multispectral photoacoustic imaging of fluorochromes in small animals,**" *Opt. Lett.,* vol. **32**, pp. 2891-2893, 2007.

[16] J. Glatz, N. C. Deliolanis, A. Buehler, D. Razansky, and V. Ntziachristos, "**Blind source unmixing in multi-spectral optoacoustic tomography,**" *Opt. Express,* vol. **19**, pp. 3175-3184, 2011.

[17] G. P. Luke and S. Y. Emelianov, "**Optimization of in vivo spectroscopic photoacoustic imaging by smart optical wavelength selection,**" *Optics Letters,* vol. **39**, pp. 2214-2217, 2014/04/01 2014.

[18] H. A. Lin, X. L. Dean-Ben, I. Ivankovic, M. A. Kimm, K. Kosanke, H. Haas, R. Meier, F. Lohofer, M. Wildgruber, and D. Razansky, "**Characterization of cardiac dynamics in an acute myocardial infarction model by four-dimensional optoacoustic and magnetic resonance imaging,**" *Theranostics,* vol. **7**, pp. 4470-4479, 2017.

[19] R. J. Zemp, "**Quantitative photoacoustic tomography with multiple optical sources,**" *Applied Optics,* vol. **49**, pp. 3566-72, Jun 20 2010.

[20] J. Yao, J. Xia, and L. V. Wang, "**Multiscale functional and molecular photoacoustic tomography,**" *Ultrasonic imaging,* p. 0161734615584312, 2015.

[21] F. J. O. Landa, X. L. Dean-Ben, R. Sroka, and D. Razansky, "**Volumetric optoacoustic temperature mapping in photothermal therapy,**" *Scientific Reports,* vol. **7**, p. 9695, Aug 29 2017.

[22] S. Iskander-Rizk, P. Kruizinga, A. F. W. van der Steen, and G. van Soest, "**Spectroscopic photoacoustic imaging of radiofrequency ablation in the left atrium,**" *Biomedical Optics Express,* vol. **9**, pp. 1309-1322, Mar 1 2018.

[23] F. M. Brochu, J. Brunker, J. Joseph, M. R. Tomaszewski, S. Morscher, and S. E. Bohndiek, "**Towards quantitative evaluation of tissue absorption coefficients using light fluence correction in optoacoustic tomography,**" *IEEE Transactions on Medical Imaging,* vol. **36**, pp. 322-331, Jan 2017.

[24] G. J. Diebold, T. Sun, and M. I. Khan, "**Photoacoustic monopole radiation in 1-dimension, 2-dimension, and 3-dimension,**" *Physical Review Letters,* vol. **67**, pp. 3384-3387, Dec 9 1991.

[25] J.-S. Jang, Y.-J. Song, W. Kang, H.-Y. Jin, J.-S. Seo, T.-H. Yang, D.-K. Kim, K.-I. Cho, B.-H. Kim, Y. H. Park, H.-G. Je, and D.-S. Kim, "**Intravascular ultrasound-guided implantation of drug-eluting stents to improve outcome: A meta-analysis,**" *JACC: Cardiovascular Interventions,* vol. **7**, pp. 233-243, 2014.

[26] S. J. Hong, B. K. Kim, D. H. Shin, C. M. Nam, J. S. Kim, Y. G. Ko, D. Choi, T. S. Kang, W. C. Kang, A. Y. Her, Y. H. Kim, S. H. Hur, B. K. Hong, H. Kwon, Y. Jang, M. K. Hong, and I.-X. Investigators, "**Effect of intravascular ultrasound-guided vs angiography-guided everolimus-eluting stent implantation: The ivus-xpl randomized clinical trial,**" *JAMA,* vol. **314**, pp. 2155-2163, Nov 24 2015.

[27] E. Falk, M. Nakano, J. F. Bentzon, A. V. Finn, and R. Virmani, "**Update on acute coronary syndromes: The pathologists' view,**" *European Heart Journal,* vol. **34**, pp. 719-728, 2013.

[28] R. Virmani, F. D. Kolodgie, A. P. Burke, A. Farb, and S. M. Schwartz, "**Lessons from sudden coronary death - a comprehensive morphological classification scheme for atherosclerotic lesions,**" *Arteriosclerosis Thrombosis And Vascular Biology,* vol. **20**, pp. 1262-1275, May 2000.

[29] R. Virmani, A. P. Burke, A. Farb, and F. D. Kolodgie, "**Pathology of the vulnerable plaque,**" *Journal of the American College Of Cardiology,* vol. **47**, pp. C13-C18, Apr 2006.

[30] J. A. Schaar, J. E. Muller, E. Falk, R. Virmani, V. Fuster, P. W. Serruys, A. Colombo, C. Stefanadis, W. S. Casscells, P. R. Moreno, A. Maseri, and A. F. W. van der Steen, "**Terminology for high-risk and vulnerable coronary artery plaques,**" *European Heart Journal,* vol. **25**, pp. 1077-1082, June 2, 2004 2004.

[31] G. van Soest, L. Marcu, B. E. Bouma, and E. Regar, "**Intravascular imaging for characterization of coronary atherosclerosis,**" *Current Opinion in Biomedical Engineering,* vol. **3**, pp. 1-12, 2017/09/01/ 2017.

[32] K. Jansen, G. van Soest, and A. F. W. van der Steen, "**Intravascular photoacoustic imaging: A new tool for vulnerable plaque identification,**" *Ultrasound in Medicine & Biology,* vol. **40**, pp. 1037-1048, 2014.

[33] P. C. Beard and T. N. Mills, "**Characterization of post mortem arterial tissue using time-resolved photoacoustic spectroscopy at 436, 461 and 532 nm,**" *Phys Med Biol,* vol. **42**, pp. 177-98, Jan 1997.

[34] S. Sethuraman, J. H. Amirian, S. H. Litovsky, R. W. Smalling, and S. Y. Emelianov, "**Spectroscopic intravascular photoacoustic imaging to differentiate atherosclerotic plaques,**" *Opt Express,* vol. **16**, pp. 3362-7, Mar 3 2008.

[35] S. Sethuraman, J. H. Amirian, S. H. Litovsky, R. W. Smalling, and S. Y. Emelianov, "**Ex vivo characterization of atherosclerosis using intravascular photoacoustic imaging,**" *Opt Express,* vol. **15**, pp. 16657-66, Dec 10 2007.

[36] B. Wang, J. L. Su, J. Amirian, S. H. Litovsky, R. Smalling, and S. Emelianov, "**Detection of lipid in atherosclerotic vessels using ultrasound-guided spectroscopic intravascular photoacoustic imaging,**" *Optics Express,* vol. **18**, pp. 4889-4897, Mar 1 2010.

[37] K. Jansen, M. Wu, A. F. van der Steen, and G. van Soest, "**Photoacoustic imaging of human coronary atherosclerosis in two spectral bands,**" *Photoacoustics,* vol. **2**, pp. 12-20, Mar 2014.

[38] P. Wang, H. W. Wang, M. Sturek, and J. X. Cheng, "**Bond-selective imaging of deep tissue through the optical window between 1600 and 1850 nm,**" *Journal of Biophotonics,* vol. **5**, pp. 25-32, Jan 2012.

[39] B. Wang, J. L. Su, J. Amirian, S. H. Litovsky, R. Smalling, and S. Emelianov, "**Detection of lipid in atherosclerotic vessels using ultrasound-guided spectroscopic intravascular photoacoustic imaging,**" *Opt Express,* vol. **18**, pp. 4889-97, Mar 1 2010.

[40] B. Wang, A. Karpiouk, D. Yeager, J. Amirian, S. Litovsky, R. Smalling, and S. Emelianov, "**In vivo intravascular ultrasound-guided photoacoustic imaging of lipid in plaques using an animal model of atherosclerosis,**" *Ultrasound Med Biol,* vol. **38**, pp. 2098-103, Dec 2012.

[41] B. Wang, A. Karpiouk, D. Yeager, J. Amirian, S. Litovsky, R. Smalling, and S. Emelianov, "**Intravascular photoacoustic imaging of lipid in atherosclerotic plaques in the presence of luminal blood,**" *Optics Letters,* vol. **37**, pp. 1244-6, Apr 1 2012.

[42] K. Jansen, A. F. van der Steen, H. M. van Beusekom, J. W. Oosterhuis, and G. van Soest, "**Intravascular photoacoustic imaging of human coronary atherosclerosis,**" *Opt Lett,* vol. **36**, pp. 597-9, Mar 1 2011.

[43] K. Jansen, A. F. van der Steen, M. Wu, H. M. van Beusekom, G. Springeling, X. Li, Q. Zhou, K. K. Shung, D. P. de Kleijn, and G. van Soest, "**Spectroscopic intravascular photoacoustic imaging of lipids in atherosclerosis,**" *J Biomed Opt,* vol. **19**, p. 026006, Feb 2014.

[44] K. Jansen, M. Wu, A. F. van der Steen, and G. van Soest, "**Lipid detection in atherosclerotic human coronaries by spectroscopic intravascular photoacoustic imaging,**" *Opt Express,* vol. **21**, pp. 21472-84, Sep 9 2013.

[45] M. Wu, K. Jansen, A. F. van der Steen, and G. van Soest, "**Specific imaging of atherosclerotic plaque lipids with two-wavelength intravascular photoacoustics,**" *Biomed Opt Express,* vol. **6**, pp. 3276-86, Sep 1 2015.

[46] R. T. Holman and P. R. Edmondson, "**Near-infrared spectra of fatty acids and some related substances,**" *Analytical Chemistry,* vol. **28**, pp. 1533-1538, 1956.

[47] M. Wu, K. Jansen, G. Springeling, A. F. van der Steen, and G. van Soest, "**Impact of device geometry on the imaging characteristics of an intravascular photoacoustic catheter,**" *Appl Opt,* vol. **53**, pp. 8131-9, Dec 1 2014.

[48] M. Wu, G. Springeling, M. Lovrak, F. Mastik, S. Iskander-Rizk, T. S. Wang, H. M. M. van Beusekom, A. F. W. van der Steen, and G. Van Soest, "**Real-time volumetric lipid imaging in vivo by intravascular photoacoustics at 20 frames per second,**" *Biomedical Optics Express,* vol. **8**, pp. 943-953, Feb 1 2017.

[49] Y. Cao, A. Kole, J. Hui, Y. Zhang, J. Mai, M. Alloosh, M. Sturek, and J. X. Cheng, "**Fast assessment of lipid content in arteries in vivo by intravascular photoacoustic tomography,**" *Sci Rep,* vol. **8**, p. 2400, Feb 5 2018.

[50] A. B. Karpiouk, B. Wang, J. Amirian, R. W. Smalling, and S. Y. Emelianov, "**Feasibility of in vivo intravascular photoacoustic imaging using integrated ultrasound and photoacoustic imaging catheter,**" *J Biomed Opt,* vol. **17**, pp. 96008-1, Sep 2012.

[51] B. Wang, A. Karpiouk, D. Yeager, J. Amirian, S. Litovsky, R. Smalling, and S. Emelianov, "**Intravascular photoacoustic imaging of lipid in atherosclerotic plaques in the presence of luminal blood,**" *Opt Lett,* vol. **37**, pp. 1244-6, Apr 1 2012.

[52] P. M. Ridker, B. M. Everett, T. Thuren, J. G. MacFadyen, W. H. Chang, C. Ballantyne, F. Fonseca, J. Nicolau, W. Koenig, S. D. Anker, J. J. P. Kastelein, J. H. Cornel, P. Pais, D. Pella, J. Genest, R. Cifkova, A. Lorenzatti, T. Forster, Z. Kobalava, L. Vida-Simiti, M. Flather, H. Shimokawa, H. Ogawa, M. Dellborg, P. R. F. Rossi, R. P. T. Troquay, P. Libby, and R. J. Glynn, "**Antiinflammatory therapy with canakinumab for atherosclerotic disease,**" *New England Journal of Medicine,* vol. **377**, pp. 1119-1131, 2017.

[53] T. Sowers and S. Emelianov, "**Exogenous imaging contrast and therapeutic agents for intravascular photoacoustic imaging and image-guided therapy,**" *Physics in Medicine and Biology,* vol. **63**, Nov 2018.

[54] C. Silvestre-Roig, M. P. de Winther, C. Weber, M. J. Daemen, E. Lutgens, and O. Soehnlein, "**Atherosclerotic plaque destabilization mechanisms, models, and therapeutic strategies,**" *Circulation Research,* vol. **114**, pp. 214-226, Jan 2014.

[55] B. Wang, E. Yantsen, T. Larson, A. B. Karpiouk, S. Sethuraman, J. L. Su, K. Sokolov, and S. Y. Emelianov, "**Plasmonic intravascular photoacoustic imaging for detection of macrophages in atherosclerotic plaques,**" *Nano Letters,* vol. **9**, pp. 2212-7, Jun 2009.

[56] N. Q. Bui, K. K. Hlaing, Y. W. Lee, H. W. Kang, and J. Oh, "**Ex vivo detection of macrophages in atherosclerotic plaques using intravascular ultrasonic-photoacoustic imaging,**" *Phys Med Biol,* vol. **62**, pp. 501-516, Jan 21 2017.

[57] H. Qin, T. Zhou, S. Yang, Q. Chen, and D. Xing, "**Gadolinium(iii)-gold nanorods for mri and photoacoustic imaging dual-modality detection of macrophages in atherosclerotic inflammation,**" *Nanomedicine (Lond),* vol. **8**, pp. 1611-24, Oct 2013.

[58] L. M. Ricles, S. Y. Nam, E. A. Trevino, S. Y. Emelianov, and L. J. Suggs, "**A dual gold nanoparticle system for mesenchymal stem cell tracking,**" *J Mater Chem B,* vol. **2**, pp. 8220-8230, Dec 14 2014.

[59] H. Qin, Y. Zhao, J. Zhang, X. Pan, S. Yang, and D. Xing, "**Inflammation-targeted gold nanorods for intravascular photoacoustic imaging detection of matrix metalloproteinase-2 (mmp2) in atherosclerotic plaques,**" *Nanomedicine,* vol. **12**, pp. 1765-1774, Oct 2016.

[60] D. Razansky, N. J. Harlaar, J. L. Hillebrands, A. Taruttis, E. Herzog, C. J. Zeebregts, G. M. van Dam, and V. Ntziachristos, "**Multispectral optoacoustic tomography of matrix metalloproteinase activity in vulnerable human carotid plaques,**" *Mol Imaging Biol,* vol. **14**, pp. 277-85, Jun 2012.

[61] X. Bai, X. Gong, W. Hau, R. Lin, J. Zheng, C. Liu, C. Zeng, X. Zou, H. Zheng, and L. Song, "**Intravascular optical-resolution photoacoustic tomography with a 1.1 mm diameter catheter,**" *PLoS One,* vol. **9**, p. e92463, 2014.

[62] M. U. Arabul, M. Heres, M. C. Rutten, M. R. van Sambeek, F. N. van de Vosse, and R. G. Lopata, "**Toward the detection of intraplaque hemorrhage in carotid artery lesions using photoacoustic imaging,**" *Journal of Biomedical Optics,* vol. **22**, p. 41010, Apr 1 2017.

[63] J. A. Schaar, C. L. de Korte, F. Mastik, R. Baldewsing, E. Regar, P. de Feyter, C. J. Slager, A. F. W. van der Steen, and P. W. Serruys, "**Intravascular palpography for high-risk vulnerable plaque assessment,**" *Herz,* vol. **28**, pp. 488-+, Sep 2003.

[64] Y. Li and Z. P. Chen, "**Multimodal intravascular photoacoustic and ultrasound imaging,**" *Biomedical Engineering Letters,* vol. **8**, pp. 193-201, May 2018.

[65] D. VanderLaan, A. B. Karpiouk, D. Yeager, and S. Emelianov, "**Real-time intravascular ultrasound and photoacoustic imaging,**" *IEEE Transactions on Ultrasonics, Ferroelectrics, and Frequency Control,* vol. **64**, pp. 141-149, Jan 2017.

[66] X. Wu, J. L. Sanders, X. Zhang, F. Y. Yamaner, and O. Oralkan, "**An fpga-based backend system for intravascular photoacoustic and ultrasound imaging,**" *IEEE Trans Ultrason Ferroelectr Freq Control,* vol. **66**, pp. 45-56, Jan 2019.

[67] V. Daeichin, C. Chen, Q. Ding, M. Wu, R. Beurskens, G. Springeling, E. Noothout, M. D. Verweij, K. W. van Dongen, J. G. Bosch, A. F. van der Steen, N. de Jong, M. Pertijs, and G. van Soest, "**A broadband polyvinylidene difluoride-based hydrophone with integrated readout circuit for intravascular photoacoustic imaging,**" *Ultrasound Med Biol,* vol. **42**, pp. 1239-43, May 2016.

[68] S. J. Mathews, C. Little, C. D. Loder, R. D. Rakhit, W. F. Xia, E. Z. Zhang, P. C. Beard, M. C. Finlay, and A. E. Desjardins, "**All-optical dual photoacoustic and optical coherence tomography intravascular probe,**" *Photoacoustics,* vol. **11**, pp. 65-70, Sep 2018.

[69] R. Yamazaki, K. Ogasawara, M. Fujiwara, K. Kobayashi, and Y. Saijo, "**Macrophage with gold nanorod visualized by optical-resolution and acoustic-resolution photoacoustic microscopes,**" *Conf Proc IEEE Eng Med Biol Soc,* vol. **2015**, pp. 2387-90, 2015.

[70] T. Sowers, D. VanderLaan, A. Karpiouk, E. M. Donnelly, E. Smith, and S. Emelianov, "**Laser threshold and cell damage mechanism for intravascular photoacoustic imaging,**" *Lasers in Surgery and Medicine,* p. doi:10.1002/lsm.23026, Oct 10 2018.

[71] A. Kole, Y. Cao, J. Hui, I. A. Bolad, M. Alloosh, J.-X. Cheng, and M. Sturek, "**Comparative quantification of arterial lipid by intravascular photoacoustic-ultrasound imaging and near-infrared spectroscopy-intravascular ultrasound,**" *Journal of cardiovascular translational research,* pp. 1-10, 2018.

[72] A. Dima, N. C. Burton, and V. Ntziachristos, "**Multispectral optoacoustic tomography at 64, 128, and 256 channels,**" *J Biomed Opt,* vol. **19**, p. 36021, Mar 2014.

[73] P. Kruizinga, A. F. van der Steen, N. de Jong, G. Springeling, J. L. Robertus, A. van der Lugt, and G. van Soest, "**Photoacoustic imaging of carotid artery atherosclerosis,**" *J Biomed Opt,* vol. **19**, p. 110504, Nov 2014.

[74] E. Mercep, X. L. Dean-Ben, and D. Razansky, "**Imaging of blood flow and oxygen state with a multi-segment optoacoustic ultrasound array,**" *Photoacoustics,* vol. **10**, pp. 48-53, Jun 2018.

[75] A. Dima and V. Ntziachristos, "**Non-invasive carotid imaging using optoacoustic tomography,**" *Optics Express,* vol. **20**, pp. 25044-57, Oct 22 2012.

[76] I. Ivankovic, E. Mer ep, C.-G. Schmedt, X. L. Deán-Ben, and D. Razansky, "**Real-time volumetric assessment of the human carotid artery: Handheld multispectral optoacoustic tomography,**" *Radiology,* vol. **291**, pp. 45-50, 2019.

[77] M. Ü. Arabul, "**Multi-wavelength photoacoustic imaging of the atherosclerotic carotid artery: A preclinical feasibility study. Phd thesis**," PhD, Technical University Eindhoven, 2018.

[78] X. Li, W. Wei, Q. Zhou, K. K. Shung, and Z. Chen, "**Intravascular photoacoustic imaging at 35 and 80 mhz,**" *Journal of Biomedical Optics,* vol. **17**, p. 106005, Oct 2012.

[79] J. Zhang, X. Gao, J. Kan, Z. Ge, L. Han, S. Lu, N. Tian, S. Lin, Q. Lu, X. Wu, Q. Li, Z. Liu, Y. Chen, X. Qian, W. Juan, D. Chai, C. Chen, X. Li, B. D. Gogas, T. Pan, S. Shan, F. Ye, and S.-L. Chen, "**Intravascular ultrasound-guided versus angiography-guided implantation of drug-eluting stent in all-comers: The ultimate trial,**" *Journal of the American College of Cardiology,* 2018/09/24/ 2018.

[80] T. E. Craven, J. E. Ryu, M. A. Espeland, F. R. Kahl, W. M. Mckinney, J. F. Toole, M. R. Mcmahan, C. J. Thompson, G. Heiss, and J. R. Crouse, "**Evaluation of the associations between carotid-artery atherosclerosis and coronary-artery stenosis - a case-control study,**" *Circulation,* vol. **82**, pp. 1230-1242, Oct 1990.

[81] G. I. Cohen, R. Aboufakher, R. Bess, J. Frank, M. Othman, D. Doan, N. Mesiha, H. S. Rosman, and S. Szpunar, "**Relationship between carotid disease on ultrasound and coronary disease on ct angiography,**" *Jacc-Cardiovascular Imaging,* vol. **6**, pp. 1160-1167, Nov 2013.

[82] A. Myat, A. H. Gershlick, and T. Gershlick, ***Landmark papers in cardiovascular medicine***: Oxford University Press, 2012.

[83] A. Bajpai, I. Savelieva, and A. J. Camm, "**Epidemiology and economic burden of atrial fibrillation,**" *US Cardiovasc Dis,* vol. **1**, pp. 14-17, 2007.

[84] S. S. Chugh, R. Havmoeller, K. Narayanan, D. Singh, M. Rienstra, E. J. Benjamin, R. F. Gillum, Y. H. Kim, J. H. McAnulty, Z. J. Zheng, M. H. Forouzanfar, M. Naghavi, G. A. Mensah, M. Ezzati, and C. J. L. Murray, "**Worldwide epidemiology of atrial fibrillation a global burden of disease 2010 study,**" *Circulation,* vol. **129**, pp. 837-847, Feb 25 2014.

[85] U. N. Srivatsa, B. Danielsen, E. A. Amsterdam, N. Pezeshkian, Y. B. Yang, E. Nordsieck, D. L. Fan, N. Chiamvimonvat, and R. H. White, "**Caabl-af (california study of ablation for atrial fibrillation): Mortality and stroke, 2005 to 2013,**" *Circulation-Arrhythmia and Electrophysiology,* vol. **11**, Jun 2018.

[86] G. Steinbeck, M. F. Sinner, M. Lutz, M. Muller-Nurasyid, S. Kaab, and H. Reinecke, "**Incidence of complications related to catheter ablation of atrial fibrillation and atrial flutter: A nationwide in-hospital analysis of administrative data for germany in 2014,**" *Eur Heart J,* vol. **39**, pp. 4020-4029, Dec 1 2018.

[87] F. Ouyang, M. Antz, S. Ernst, H. Hachiya, H. Mavrakis, F. T. Deger, A. Schaumann, J. Chun, P. Falk, D. Hennig, X. Liu, D. Bansch, and K. H. Kuck, "**Recovered pulmonary vein conduction as a dominant factor for recurrent atrial tachyarrhythmias after complete circular isolation of the pulmonary veins: Lessons from double lasso technique,**" *Circulation,* vol. **111**, pp. 127-35, Jan 18 2005.

[88] L. Ganjehei, M. Razavi, and A. Rasekh, "**Catheter-based ablation of atrial fibrillation: A brief overview,**" *Tex Heart Inst J,* vol. **38**, pp. 361-3, 2011.

[89] M. Wright, "**Real-time atrial wall imaging,**" *Heart Rhythm,* vol. **12**, pp. 1836-1837, 2015.

[90] G. A. Pang, E. Bay, X. L. Dean-Ben, and D. Razansky, "**Three-dimensional optoacoustic monitoring of lesion formation in real time during radiofrequency catheter ablation,**" *J Cardiovasc Electrophysiol,* vol. **26**, pp. 339-45, Mar 2015.

[91] R. Bouchard, N. Dana, L. Di Biase, A. Natale, and S. Emelianov, "**Photoacoustic characterization of radiofrequency ablation lesions,**" *Proc SPIE Int Soc Opt Eng,* vol. **8223**, Jan 21 2012.

[92] N. Dana, L. Di Biase, A. Natale, S. Emelianov, and R. Bouchard, "**In vitro photoacoustic visualization of myocardial ablation lesions,**" *Heart Rhythm,* vol. **11**, pp. 150-7, Jan 2014.

[93] R. P. Singh-Moon, C. C. Marboe, and C. P. Hendon, "**Near-infrared spectroscopy integrated catheter for characterization of myocardial tissues: Preliminary demonstrations to radiofrequency ablation therapy for atrial fibrillation,**" *Biomedical Optics Express,* vol. **6**, pp. 2494-2511, Jul 1 2015.

[94] A. H. Gandjbakhche, R. F. Bonner, A. E. Arai, and R. S. Balaban, "**Visible-light photon migration through myocardium in vivo,**" *Am J Physiol,* vol. **277**, pp. H698-704, Aug 1999.

[95] C. Schmitt, I. Deisenhofer, and B. Zrenner, ***Catheter ablation of cardiac arrhythmias: A practical approach***: Springer Science & Business Media, 2006.

[96] S. R. Dukkipati, K.-H. Kuck, P. Neuzil, I. Woollett, J. Kautzner, H. T. McElderry, B. Schmidt, E. P. Gerstenfeld, S. K. Doshi, R. Horton, A. Metzner, A. d'Avila, J. N. Ruskin, A. Natale, and V. Y. Reddy, "**Pulmonary vein isolation using a visually guided laser balloon catheter: The first 200-patient multicenter clinical experience,**" *Circulation: Arrhythmia and Electrophysiology,* vol. **6**, pp. 467-472, June 1, 2013 2013.

[97] H. Aupperle, N. Doll, T. Walther, C. Ullmann, H.-A. Schoon, F. J. I. c. Wilhelm Mohr, and t. surgery, "**Histological findings induced by different energy sources in experimental atrial ablation in sheep,**" vol. **4**, pp. 450-455, 2005.

[98] J. Rebling, F. J. Oyaga Landa, X. L. Dean-Ben, A. Douplik, and D. Razansky, "**Integrated catheter for simultaneous radio frequency ablation and optoacoustic monitoring of lesion progression,**" *Opt Lett,* vol. **43**, pp. 1886-1889, Apr 15 2018.

[99] A. Nikoozadeh, J. W. Choe, S. R. Kothapalli, A. Moini, S. S. Sanjani, A. Kamaya, O. Oralkan, S. S. Gambhir, and P. T. Khuri-Yakub, "**Photoacoustic imaging using a 9f microlinear cmut ice catheter,**" *2012 Ieee International Ultrasonics Symposium (Ius),* pp. 24-27, 2012.

[100] N. de Groot, L. van der Does, A. Yaksh, E. Lanters, C. Teuwen, P. Knops, P. van de Woestijne, J. Bekkers, C. Kik, A. Bogers, and M. Allessie, "**Direct proof of endo-epicardial asynchrony of the atrial wall during atrial fibrillation in humans,**" *Circulation: Arrhythmia and Electrophysiology,* vol. **9**, p. e003648, May 2016.

[101] N. Dana, R. A. Fowler, A. Allen, J. Zoldan, L. Suggs, and S. Emelianov, "**In vitrophotoacoustic sensing of calcium dynamics with arsenazo iii,**" *Laser Physics Letters,* vol. **13**, p. 075603, Jul 2016.

[102] H. C. K. Zhang, P. Yan, J. Kang, D. S. Abou, H. N. D. Le, A. K. Jha, D. L. J. Thorek, J. U. Kang, A. Rahmim, D. F. Wong, E. M. Boctor, and L. M. Loew, "**Listening to membrane potential: Photoacoustic voltage-sensitive dye recording,**" *Journal of Biomedical Optics,* vol. **22**, Apr 2017.

[103] B. Rao, R. Zhang, L. Li, J. Y. Shao, and L. V. Wang, "**Photoacoustic imaging of voltage responses beyond the optical diffusion limit,**" *Sci Rep,* vol. **7**, p. 2560, May 31 2017.

[104] L. Li and G. J. Tearney, "**Apparatus, systems and methods for characterizing, imaging and/or modifying an object**," ed: Google Patents, 2017

[105] U. Herken, A. Silver, C. Kaufman, and G. A. Freeman, "**Transesophageal or transtracheal cardiac monitoring by optical spectroscopy**," ed: Google Patents, 2016

[106] S. Hu and L. V. Wang, "**Photoacoustic imaging and characterization of the microvasculature,**" *Journal of Biomedical Optics,* vol. **15**, p. 011101, Jan-Feb 2010.

[107] S. Hu, K. Maslov, and L. V. Wang, "**Noninvasive label-free imaging of microhemodynamics by optical-resolution photoacoustic microscopy,**" *Optics Express,* vol. **17**, pp. 7688-93, Apr 27 2009.

[108] P. Beard, "**Biomedical photoacoustic imaging,**" *Interface Focus,* vol. **1**, pp. 602-31, Aug 6 2011.

[109] J. Aguirre, M. Schwarz, N. Garzorz, M. Omar, A. Buehler, K. Eyerich, and V. Ntziachristos, "**Precision assessment of label-free psoriasis biomarkers with ultra-broadband optoacoustic mesoscopy,**" *Nature Biomedical Engineering,* vol. **1**, p. 0068, 05/10/online 2017.

[110] E. I. Galanzha and V. P. Zharov, "**Photoacoustic flow cytometry,**" *Methods,* vol. **57**, pp. 280-96, Jul 2012.

[111] E. I. Galanzha, M. Sarimollaoglu, D. A. Nedosekin, S. G. Keyrouz, J. L. Mehta, and V. P. Zharov, "**In vivo flow cytometry of circulating clots using negative photothermal and photoacoustic contrasts,**" *Cytometry A,* vol. **79**, pp. 814-24, Oct 2011.

[112] E. I. Galanzha and V. P. Zharov, "**In vivo photoacoustic and photothermal cytometry for monitoring multiple blood rheology parameters,**" *Cytometry A,* vol. **79**, pp. 746-57, Oct 2011.

[113] M. A. Juratli, Y. A. Menyaev, M. Sarimollaoglu, A. V. Melerzanov, D. A. Nedosekin, W. C. Culp, J. Y. Suen, E. I. Galanzha, and V. P. Znarov, "**Noninvasive label-free detection of circulating white and red blood clots in deep vessels with a focused photoacoustic probe,**" *Biomedical Optics Express,* vol. **9**, pp. 5667-5677, Nov 1 2018.

[114] M. A. Juratli, Y. A. Menyaev, M. Sarimollaoglu, E. R. Siegel, D. A. Nedosekin, J. Y. Suen, A. V. Melerzanov, T. A. Juratli, E. I. Galanzha, and V. P. Zharov, "**Real-time label-free embolus detection using in vivo photoacoustic flow cytometry,**" *Plos One,* vol. **11**, May 26 2016.

[115] E. I. Galanzha, M. G. Viegas, T. I. Malinsky, A. V. Melerzanov, M. A. Juratli, M. Sarimollaoglu, D. A. Nedosekin, and V. P. Zharov, "**In vivo acoustic and photoacoustic focusing of circulating cells,**" *Scientific Reports,* vol. **6**, Mar 16 2016.

[116] P. J. van den Berg, K. Daoudi, and W. Steenbergen, "**Review of photoacoustic flow imaging: Its current state and its promises,**" *Photoacoustics,* vol. **3**, pp. 89-99, Sep 2015.

[117] V. V. Tuchin, A. Tarnok, and V. P. Zharov, "**In vivo flow cytometry: A horizon of opportunities,**" *Cytometry A,* vol. **79**, pp. 737-45, Oct 2011.

[118] K. Reddy, A. Khaliq, and R. J. Henning, "**Recent advances in the diagnosis and treatment of acute myocardial infarction,**" *World Journal of Cardiology,* vol. **7**, pp. 243-276, May 26 2015.

[119] R. A. Mukaddim, A. Rodgers, T. A. Hacker, A. Heinmiller, and T. Varghese, "**Real-time in vivo photoacoustic imaging in the assessment of myocardial dynamics in murine model of myocardial ischemia,**" *Ultrasound Med Biol,* vol. **44**, pp. 2155-2164, Oct 2018.

[120] R. J. Zemp, L. Song, R. Bitton, K. K. Shung, and L. V. Wang, "**Realtime photoacoustic microscopy of murine cardiovascular dynamics,**" *Optics Express,* vol. **16**, pp. 18551-6, Oct 27 2008.

[121] J. Lv, Y. Peng, S. Li, Z. Guo, Q. Zhao, X. Zhang, and L. Nie, "**Hemispherical photoacoustic imaging of myocardial infarction: In vivo detection and monitoring,**" *European Radiology,* vol. **28**, pp. 2176-2183, May 2018.

[122] M. T. Berninger, P. Mohajerani, M. Wildgruber, N. Beziere, M. A. Kimm, X. Ma, B. Haller, M. J. Fleming, S. Vogt, M. Anton, A. B. Imhoff, V. Ntziachristos, R. Meier, and T. D. Henning, "**Detection of intramyocardially injected dir-labeled mesenchymal stem cells by optical and optoacoustic tomography,**" *Photoacoustics,* vol. **6**, pp. 37-47, Jun 2017.

[123] F. G. Marcondes-Braga, G. L. Batista, I. G. Gutz, P. H. Saldiva, S. Mangini, V. S. Issa, S. M. Ayub-Ferreira, E. A. Bocchi, A. C. Pereira, and F. Bacal, "**Impact of exhaled breath acetone in the prognosis of patients with heart failure with reduced ejection fraction (hfref). One year of clinical follow-up,**" *PLoS One,* vol. **11**, p. e0168790, Dec 28 2016.

[124] S. Mythili and N. Malathi, "**Diagnostic markers of acute myocardial infarction,**" *Biomed Rep,* vol. **3**, pp. 743-748, Nov 2015.

[125] M. J. Navas, A. M. Jimenez, and A. G. Asuero, "**Human biomarkers in breath by photoacoustic spectroscopy,**" *Clin Chim Acta,* vol. **413**, pp. 1171-8, Aug 16 2012.

[126] J. Pereira, P. Porto-Figueira, C. Cavaco, K. Taunk, S. Rapole, R. Dhakne, H. Nagarajaram, and J. S. Camara, "**Breath analysis as a potential and non-invasive frontier in disease diagnosis: An overview,**" *Metabolites,* vol. **5**, pp. 3-55, Mar 2015.

[127] F. G. Marcondes-Braga, G. L. Batista, F. Bacal, and I. Gutz, "**Exhaled breath analysis in heart failure,**" *Current Heart Failure Reports,* vol. **13**, pp. 166-71, Aug 2016.

[128] F. S. Cikach, Jr. and R. A. Dweik, "**Cardiovascular biomarkers in exhaled breath,**" *Prog Cardiovasc Dis,* vol. **55**, pp. 34-43, Jul-Aug 2012.

[129] S. Cheng, D. Enserro, V. Xanthakis, L. M. Sullivan, J. M. Murabito, E. J. Benjamin, J. F. Polak, C. J. O'Donnell, P. A. Wolf, G. T. O'Connor, J. F. Keaney, and R. S. Vasan, "**Association of exhaled carbon monoxide with subclinical cardiovascular disease and their conjoint impact on the incidence of cardiovascular outcomes,**" *European Heart Journal,* vol. **35**, pp. 2980-2987, Nov 7 2014.

[130] Z. W. Weitz, A. J. Birnbaum, P. A. Sobotka, E. J. Zarling, and J. L. Skosey, "**High breath pentane concentrations during acute myocardial-infarction,**" *Lancet,* vol. **337**, pp. 933-935, Apr 20 1991.

[131] S. M. Cristescu, R. Kiss, S. Hekkert, M. Dalby, F. J. Harren, T. H. Risby, and N. Marczin, "**Real-time monitoring of endogenous lipid peroxidation by exhaled ethylene in patients undergoing cardiac surgery,**" *Am J Physiol Lung Cell Mol Physiol,* vol. **307**, pp. L509-15, Oct 1 2014.

[132] P. Agostoni, G. Cattadori, A. Apostolo, M. Contini, P. Palermo, G. Marenzi, and K. Wasserman, "**Noninvasive measurement of cardiac output during exercise by inert gas rebreathing technique: A new tool for heart failure evaluation,**" *J Am Coll Cardiol,* vol. **46**, pp. 1779-81, Nov 1 2005.

[133] C. C. Lang, P. Karlin, J. Haythe, L. Tsao, and D. M. Mancini, "**Ease of noninvasive measurement of cardiac output coupled with peak vo2 determination at rest and during exercise in patients with heart failure,**" *Am J Cardiol,* vol. **99**, pp. 404-5, Feb 1 2007.

[134] A. Gabrielsen, R. Videbaek, M. Schou, M. Damgaard, J. Kastrup, and P. Norsk, "**Non-invasive measurement of cardiac output in heart failure patients using a new foreign gas rebreathing technique,**" *Clinical Science (London, England: 1979),* vol. **102**, pp. 247-52, Feb 2002.

[135] R. Li, M. N. Slipchenko, P. Wang, and J.-X. Cheng, "**Compact high power barium nitrite crystal-based raman laser at 1197 nm for photoacoustic imaging of fat,**" *Journal Of Biomedical Optics,* vol. **18**, pp. 040502-040502, 2013.

[136] P. Wang, T. Ma, M. N. Slipchenko, S. Liang, J. Hui, K. K. Shung, S. Roy, M. Sturek, Q. Zhou, Z. Chen, and J.-X. Cheng, "**High-speed intravascular photoacoustic imaging of lipid-laden atherosclerotic plaque enabled by a 2-khz barium nitrite raman laser,**" *Sci. Rep.,* vol. **4**, p. 6889 2014.

[137] A. Stylogiannis, L. Prade, A. Buehler, J. Aguirre, G. Sergiadis, and V. J. P. Ntziachristos, "**Continuous wave laser diodes enable fast optoacoustic imaging,**" vol. **9**, pp. 31-38, 2018.

[138] P. K. Upputuri and M. Pramanik, "**Fast photoacoustic imaging systems using pulsed laser diodes: A review,**" *Biomedical Engineering Letters,* vol. **8**, pp. 167-181, May 01 2018.

[139] M. Arabul, "**Multi-wavelength photoacoustic imaging of the atherosclerotic carotid artery: A preclinical feasibility study,**" 2018.

[140] M. U. Arabul, M. Heres, M. C. Rutten, M. R. van Sambeek, F. N. van de Vosse, and R. G. Lopata, "**Toward the detection of intraplaque hemorrhage in carotid artery lesions using photoacoustic imaging,**" *J Biomed Opt,* vol. **22**, p. 41010, Apr 1 2017.

[141] Y. Zhu, G. Xu, J. Yuan, J. Jo, G. Gandikota, H. Demirci, T. Agano, N. Sato, Y. Shigeta, and X. Wang, "**Light emitting diodes based photoacoustic imaging and potential clinical applications,**" *Scientific Reports,* vol. **8**, p. 9885, 2018.

[142] W. Xia, M. K. A. Singh, E. Maneas, N. Sato, Y. Shigeta, T. Agano, S. Ourselin, S. J. West, and A. E. Desjardins, "**Handheld real-time led-based photoacoustic and ultrasound imaging system for accurate visualization of clinical metal needles and superficial vasculature to guide minimally invasive procedures,**" *Sensors,* vol. **18**, p. 10.3390/s18051394, 2018.

[143] H. T. Zhong, T. Y. Duan, H. R. Lan, M. Zhou, and F. Gao, "**Review of low-cost photoacoustic sensing and imaging based on laser diode and light-emitting diode,**" *Sensors,* vol. **18**, Jul 2018.

[144] A. Nikoozadeh, C. L. Chang, J. W. Choe, A. Bhuyan, B. C. Lee, A. Moini, and P. T. Khuri-Yakub, "**An integrated ring cmut array for endoscopic ultrasound and photoacoustic imaging,**" *2013 Ieee International Ultrasonics Symposium (Ius),* pp. 1170-1173, 2013.

[145] R. Ansari, E. Z. Zhang, A. E. Desjardins, and P. C. Beard, "**All-optical forward-viewing photoacoustic probe for high-resolution 3d endoscopy,**" *Light Sci Appl,* vol. **7**, p. 75, 2018.

[146] V. Daeichin, C. Chen, Q. Ding, M. Wu, R. Beurskens, G. Springeling, E. Noothout, M. D. Verweij, K. W. A. van Dongen, J. G. Bosch, A. F. W. van der Steen, N. de Jong, M. Pertijs, and G. van Soest, "**A broadband polyvinylidene difluoride-based hydrophone with integrated readout circuit for intravascular photoacoustic imaging,**" *Ultrasound in Medicine and Biology,* vol. **42**, pp. 1239-1243, May 2016.

[147] E. Mer ep, G. Jeng, S. Morscher, L. Pai-Chi, and D. Razansky, "**Hybrid optoacoustic tomography and pulse-echo ultrasonography using concave arrays,**" *Ultrasonics, Ferroelectrics, and Frequency Control, IEEE Transactions on,* vol. **62**, pp. 1651-1661, 2015.

[148] M. Seeger, A. Karlas, D. Soliman, J. Pelisek, and V. Ntziachristos, "**Multimodal optoacoustic and multiphoton microscopy of human carotid atheroma,**" *Photoacoustics,* vol. **4**, pp. 102-111, Sep 2016.

Chapter 2

Spectroscopic characterization of RF ablation lesions

Sophinese Iskander-Rizk, Pieter Kruizinga, Antonius F.W. van der Steen and Gijs van Soest.

Published in
Biomedical optics express, 9(3), 2018

Abstract

Catheter-based radiofrequency ablation for atrial fibrillation has long-term success in 60-70% of cases. A better assessment of lesion quality, depth, and continuity could improve the procedure's outcome. We investigate here photoacoustic contrast between ablated and healthy atrial-wall tissue in vitro in wavelengths spanning from 410 nm to 1000 nm. We studied single- and multi-wavelength imaging of ablation lesions and we demonstrate that a two-wavelength technique yields precise detection and delineation of lesions, achieving a diagnostic accuracy of 97%. We compare this with a best single-wavelength (640 nm) analysis that correctly identifies 82% of lesions. We discuss the origin of relevant spectroscopic features and perspectives for translation to clinical imaging.

2.1 Introduction

2.1.1 Atrial fibrillation

Atrial fibrillation (AF) is a cardiac arrhythmia which arises as a result of electrical activation patterns originating from the atrial wall, rather than the sino-atrial node. The atrium contracts more frequently and asynchronous from the ventricles, leading to reduced overall pump efficiency and vortex flow. Approximately 5% of people over 55 in Western countries suffer from AF, while prevalence increases with age [1, 2]. The pathology is associated with a variety of cardiovascular symptoms, such as a higher probability of thromboembolism and stroke, and heart failure, unfolding into increased mortality. Current treatment strategies include pharmaceutical treatment, surgical interventions, and minimally-invasive catheter-based ablation.

In catheter-based radiofrequency (RF) ablation, errant conduction loops are interrupted by inducing tissue necrosis through application of thermal energy. The scar tissue that subsequently forms is non-conductive and effects restoration of a regular contraction pattern. Patients who do not respond to pharmaceutical therapy (~60% [3]), or who are at high risk for surgery, are candidates for catheter-based ablation. It is also advised as a more economical alternative for therapy in younger patients, who would otherwise require lifelong medication [4]. However, current catheter- based ablation procedures have a success rate of about 60-70% [5]. The intervention frequently fails as a result of tissue electrical reconduction, arising in the days, weeks or months after ablation. Causes for reconduction are insufficient ablation, ablation gaps and tissue remodelling. On the other hand, complications due to over-ablation include venous stenosis, thrombus formation, and tamponade; which explains the tendency for interventionists to err on the side of caution and ablate conservatively. Feedback on lesion progression is currently indirect: lesion extent is assessed via impedance changes, as well as temperature and contact force values, all measured at the catheter tip. Finally, the end point of ablation is determined by the cessation of electrical activity at the ectopic foci after pacing. Better monitoring and control of the ablation process, quantifying both extent and functionality of the lesion is one way to reduce the duration and improve the outcome of the procedure [6].

2.1.2 RF ablation lesion imaging in the literature

In the quest of improving the success rate of catheter-based ablation procedures, much research has been directed towards assessment of the lesions created by ablation. Multiple imaging modalities have been explored; the most successful thus far being CMR (cardiac magnetic resonance) gadolinium enhanced imaging. However, CMR, compared to other imaging modalities, is difficult to apply during an intervention, as it requires an MRI-equipped cardiac electrophysiology catheterization room, and MRI-compatible instruments [7]. It has mediocre image resolution (resolution cell ≈ 1-2 mm ≈ atrial wall depth), leading to a poor assessment of lesion area, volume and transmurality [8], and is relatively expensive.

Optical methods which were explored for lesion delineation include Optical Coherence Tomography (OCT) [9], Near Infrared Spectroscopy (NIRS) [10] and auto-Fluorescence Hyperspectral Imaging (aHSI) [11]. These methods are based on scattered, reflected and emitted light from the tissue. However, despite demonstration of contrast between lesion and non-ablated tissue in all three modalities, they lack reliable evaluation of lesion extent in depth.

Other imaging modalities which were explored for ablation lesion monitoring are conventional ultrasound [12-15] as well as ultrasound elastography [16-18]. Visibility of lesions on grayscale ultrasound has been disputed in literature, with contradictory reports of both decrease and increase in echogenicity in lesion areas. Elastography, on the other hand, seems more successful at lesion identification and looks quite promising. However, monitoring lesion progression with shear wave elastography is still a challenge due to the estimation of atrial wall curvature for wave propagation progression and the difficulty in aligning the ultrasound beam to the lesion site across the ablation catheter [18].

2.1.3 Photoacoustic imaging for lesion progression monitoring

Previous studies have shown optical, mechanical as well as acoustic contrast between lesions and the remaining non-ablated tissue; yet the challenge of the development of an accurate lesion delineation method that is easily translatable to the clinical setting remains. Photoacoustic (PA) imaging incorporates all aforementioned types of contrast. The PA source pressure $p_0(z) = \Gamma(z)\cdot\mu_a(z,\lambda)\cdot F(z,\lambda)$ is the product of the local optical fluence F, the local optical absorption coefficient μ_a, and the Grüneisen coefficient Γ. The absorption and fluence depend on wavelength and tissue optical properties. The Grüneisen coefficient is the conversion factor between optical energy to thermo-elastic strain, and potentially provides information on tissue stiffness and temperature. PA imaging is unique in its access to such a wide array of tissue properties which may play a role in lesion characterization.

Intracardiac echo (ICE) is frequently used to guide septal puncture in ablation procedures for atrial fibrillation. The ultrasound catheter, with a typical centre frequency of about 7 MHz, could also be used for detection of PA signals if light could be delivered through a modified ablation catheter for instance. The potential for clinical translation and enhanced contrast encouraged us to look further into photoacoustic imaging as a means of monitoring lesion formation.

Two groups have previously performed PA imaging of RF ablation lesions on porcine cardiac tissue ex-vivo [19, 20]. Pang et al. [19] have identified a maximum lesion to non-ablated tissue contrast at 780 nm using a 3 MHz transducer. Dana et al.[20] revealed a spectral signature providing contrast at wavelengths near 760 nm (which was attributed to the haemoglobin spectral signature disappearing) using a 21 MHz transducer. Both studies evaluated lesion formation in ventricular tissue, which is not directly generalizable to atrial ablation.

In this study we analysed the PA signal from healthy and ablated porcine left atrial tissue including endocardial and epicardial layers. We acquired PA signals with a linear array transducer of centre frequency matching that of ICE catheters to verify bandwidth compatibility. We performed PA spectroscopic imaging prior to, and after ablation. We identify the spectral changes between fresh and ablated tissue in order to visualize the induced changes in tissue composition, as well as identify wavelengths for optimal contrast, imaging depth and signal to noise ratio (SNR). We demonstrate robust contrast for identification of ablation lesions and quantify the diagnostic accuracy by computing the receiver-operator curve for lesion detection, using either a single wavelength or an optimal combination of two wavelengths.

2.2 Materials and methods

2.2.1 Sample materials and tissue handling

We evaluated PA image contrast after RF ablation of fresh excised porcine left atria (0-24 h post mortem), obtained from a local butcher and from the Dept. of Experimental Cardiology in our institute. We collected 23 spectra (23 lesions) from 14 different tissue samples originating from 12 different hearts. The average depth/thickness of the tissue examined was of 2.7 mm with a maximum of 8 mm and a minimum of 400 µm, as measured from US images.

Tissues were mounted in a water tank, suspended by wires. For ablation we used an EPT 1000 XP APM system (Boston Scientific, Marlborough, Massachusetts, United States) with a Blazer II HTD, Asym #4 (model: 5031 THN4) catheter. We delivered ablation energy to localized site(s) of the endocardium in the imaging plane, using appropriate settings (Power ≥ 20W, Temperature ≥ 60˚C, time ≥ 20s). We kept ablating the same lesion site (n ≥ 1) until a visible lesion was produced on the endocardium side. After PA imaging, we sectioned the tissue through the lesion for visual inspection. We determined the imaged plane by inserting needles that are visible on the ultrasound image. Throughout the measurement, the tissue was kept in a HEPES buffer mixed with saline solution of pH 7.4 at room temperature.

2.2.2 Setup Description

We performed photoacoustic spectroscopy with a pulsed laser source (10 Hz) tuned from 410 nm to 708 nm, and 712 nm to 1000 nm (Vibrant B-355II, Opotek, Santa Clara, CA, USA) in steps of 2 nm. The setup consisted of a linear array transducer (192 channels, L12-3v, f_c = 7.8 MHz, Verasonics, Kirkland, Washington) connected to a Verasonics Vantage 256 research system. The acquisition was programmed to overlay images created from pulse echo plane wave ultrasound (US) at 3 different angles (-18˚, 0˚, +18˚), and from photoacoustic signals averaged over 6 laser pulses. During the photoacoustic acquisition, the time-gain compensation (TGC) was set to

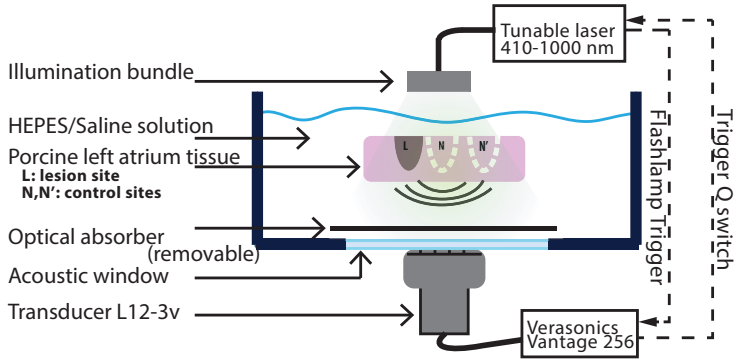

Figure 2.1 Transmission PA imaging setup for spectroscopic analysis of RF ablation lesions. The tissue is suspended and stretched with the aid of wires. A fibre bundle illuminates the atrium sample from the endocardial side. A 192 element 7.8 MHz centre frequency transducer records the generated PA signal. A black plastic sheet (optical absorber) provides a reference signal to assess optical attenuation. We analyse spectroscopic differences in PA response in lesion (L) and control (N,N') sites.

its maximum value (not changing with depth), to optimize examination of the signal attenuation with depth. The tissue was mounted in a transmission-mode PA setup (Figure 2.1), with the endocardium facing a broad illumination source. We performed spectroscopic imaging, before and after ablating the tissue, keeping the relative position of the tissue and the transducer as stable as possible, in order to compare the signal before and after ablation from the same portion of tissue. After acquiring tissue spectroscopy data, we measured the OPO tuning curve for calibration of the PA signal. The fluence varied between 0.3 and 1 mJ/cm^2 depending on the wavelength.

2.2.3 Extraction and validation of photoacoustic spectra

From the beamformed photoacoustic images, we averaged the intensity (I) in a user-defined image region of interest (ROI, I_{ROI}), as a function of excitation wavelength. We identified regions in co-registered images generated prior to and after ablation. The lesion position was identified as the location of the ablation catheter and the lesion extent was defined from the visual inspection of the tissue cross section after the experiment. In post-ablation images, we selected two regions, a lesion site (L, post) and a non-ablated site (N/N', post). Definition of ROIs on the illuminated endocardial side minimizes the impact of spectral colouring when evaluating the tissue spectral photoacoustic features. ROI size ranged from 3×3 pixels (= 0.3×0.6 mm axial × lateral) to 10×10 pixels (= 1×2 mm) depending on visual lesion size.

We averaged all spectra extracted from three identified region classes: lesion (L, post), lesion site prior to ablation (L, pre), and control after ablation (N, post),

shown in Figure 2.2. We equalized the means across the spectrum to account for day-to-day variations prior to averaging all the traces and computing the standard deviations. We also normalized to the OPO tuning curve verified after each experiment. We validated our methodology by corroborating the water absorption spectrum at the water-air interface to those reported in the literature [21, 22].

We assessed spectral optical attenuation by recording the signal form a highly absorbing black plastic phantom behind the tissue as shown in Figure 2.1. Reliable volumetric imaging of ablation lesions is only possible in those spectral regions that allow sufficient penetration of excitation light. Wavelengths which reliably generate a signal from the black target behind the tissue are suitable for transmural imaging, which was true for $\lambda > 600$ nm, reflecting the familiar decrease of optical attenuation with increasing wavelength.

2.2.4 Quantitative evaluation of imaging parameters

Contrast in single wavelength images

We calculated the signal ratio (SR_L) as the ratio I_L/I_N (subscripts refer to the regions as indicated in Figure 2.1) on post-ablation images, which characterizes lesion delineation (contrast with neighbouring tissue). We observed that at most wavelengths in our investigated spectral range, the PA signal increased by ablation (independent of temperature), in agreement with literature, so normally $SR_L > 1$. In our data set, we have included multiple different tissue and lesion models (i.e. superficial lesions, tissue slabs with 1 to 3 lesions, trabeculae structure). The mean of the collected SR from all lesion samples thus reflects the general signal contrast due to the ablation process, and the standard deviation indicates the expected variability in this contrast due to different tissue types and ablation strategies. The SR_N for non-lesion sites is a control variable to estimate the variability in signal within one tissue sample among different non-ablated sites. The SR_N was computed as the signal ratio between two different control areas I_N/I_N' on post-ablation images; the mean provides information about the signal variation across the tissue due to the tissue intra variability and the standard deviation is caused by the variation in signal due to different left atrium tissue sites.

Wavelength selection criteria for dual wavelength imaging

We explored a dual wavelength imaging method, which takes the ratio of two subsequent frames acquired at different wavelengths, aiming at differentiating lesion sites from untreated tissue. The final dual wavelength image was obtained by subtracting the mean noise value from the overall image to equalize the background among the data set acquired. The rationale behind a two colour imaging method is to develop an easily interpretable image that directly identifies and delineates ablation lesions. A two-colour ratio image would be insensitive to both temperature effects, and, if the two wavelengths are sufficiently closely spaced, to variation in fluence due

to tissue attenuation, approximating $p_0(z,\lambda_1) / p_0(z,\lambda_2) = \mu_a(z,\lambda_1) / \mu_a(z,\lambda_2)$. A dual wavelength imaging method would eliminate the need for modelling the impact of tissue optics or temperature (which both change during ablation) on the photoacoustic signal.

In order to determine the wavelength pair that provides the highest, most reliable lesion contrast, we first defined the two-wavelength signal ratio for control ($Ø_N$) and lesion ($Ø_L$) areas:

$$Ø_N = \frac{I_N(\lambda_1)}{I_N(\lambda_2)} \tag{1}$$

$$Ø_L = \frac{I_L(\lambda_1)}{I_L(\lambda_2)} \tag{2}$$

We restricted the wavelengths to 630 nm $< \lambda <$ 1000 nm to ensure a homogeneous illumination in a slab of 3 mm by excluding highly attenuated wavelengths, and avoiding the spectral range around the OPO tuning degeneracy gap, near 709 nm (702-724 nm, because of low output fluence $<$ 0.3 mJ/cm^2 and thus limited SNR). Variability in medium optical properties can be prevented by limiting the spectral separation between the two wavelengths.

We then determined the best pair of wavelengths for a ratio image by evaluating:

$$\{\lambda_1, \lambda_2\} = \arg \max_{\Delta\lambda<150\text{nm}} \left\langle \frac{Ø_L}{Ø_N} \right\rangle, \text{ such that } \left\langle \frac{Ø_L}{Ø_N} \right\rangle > 2 \cdot \sigma \left(\frac{Ø_L}{Ø_N} \right) \tag{3}$$

$\langle \cdot \rangle$ denotes the mean over all measurements. Images constructed from the PA signal at an optimal combination of two wavelengths highlight lesions against a background of unaffected tissue. Eq. (3) maximizes the contrast between these two tissue classes, while limiting the variability due to the disparity of tissue and ablation strategy.

Evaluation of dual and single wavelength images for lesion formation

We compared the performance of a dual wavelength to a single wavelength imaging method for detecting whether a lesion has been created. Diagnostic accuracy can be evaluated by receiver-operator characteristic (ROC) analysis. As the imaged quantities are different for both imaging approaches, we need to define different criteria for lesion identification. We calculated the number of true positives (TP; correctly identified lesions) in a dual wavelength image, as the amount of lesion sets for which the ratio exceeds a certain threshold $Ø_{thr}$:

$$Ø_{L,post} > Ø_{thr} \tag{4}$$

False positives (FP) are areas in which this threshold is reached prior to ablation:

$$Ø_{L,pre} > Ø_{thr} \tag{5}$$

In single wavelength images, we can only compare PA signal amplitude in lesion areas post and pre-ablation. We defined the true positives as:

$$Z_L = \frac{I_{L,post}}{I_{L,pre}} > Z_{thr} \quad (6)$$

and the false positives as control areas exceeding this threshold:

$$Z_N = \frac{I_{N,post}}{I_{N,pre}} > Z_{thr} \quad (7)$$

We divided the number of TP and FP observations by the number of lesion samples we have collected to obtain TP/FP rates. The total number of controls was equal to the number of lesions collected. Both Z and Ø are amplitude ratios and so are comparable variables. Ideally, the two wavelengths chosen for the dual wavelength images should yield a featureless image prior to ablation, and clearly discernible areas corresponding to lesion sites in post-ablation images. An equivalent representation in a single wavelength imaging scheme would occur if we divide the post-ablation frame with the pre-ablation one.

Evaluation of dual and single wavelength images for lesion delineation

Delineation of lesions is important to assess lesion continuity in ablation procedures. This can be evaluated as the contrast between lesion areas and neighbouring tissue after ablation. We evaluated delineation capability of single and dual wavelength imaging by ROC analysis. For two-wavelength imaging, we defined the true positives as in (Equ. 4), while false positives are control areas satisfying the threshold criterion:

$$Ø_{N,post} > Ø_{thr} \quad (8)$$

In single-wavelength images, the true positives (lesions are clearly delineated from the rest of the tissue) are defined as the lesions for which the SR_L exceeds the threshold ratio Z_{thr}, while false positives are control areas SR_N meeting that norm.

2.3 Results

2.3.1 Photoacoustic signal variation with illumination wavelength

In Figure 2.2, we plot the average of PA signals normalized to the mean variation over the imaging wavelengths at different tissue sites. The orange and green curves in Figure 2.2 present spectra of non-ablated sites on tissue before and after ablation respectively. These curves show that ablation modifies the spectral absorption features at the ablated site only: the control site after ablation has the same appearance as the lesion before. In the spectra we identify spectral features representing the characteristics of myoglobin with distinctive peaks at 555 nm and 760 nm. The flattened peak around 550 nm indicates that the observed spectrum is resulting from a mix of oxymyoglobin and myoglobin.

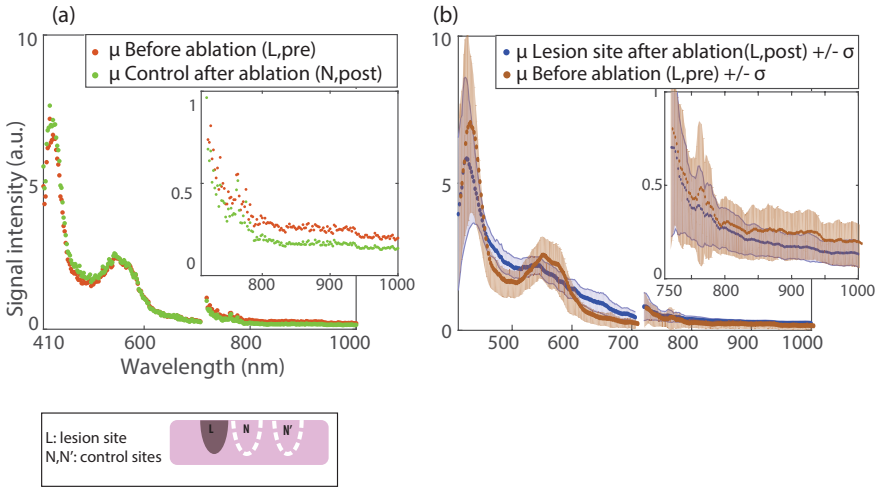

Figure 2.2 Average (μ) of spectra extracted from 23 tissue sites. (a) Comparison of non-lesion sites before and after ablation. (b) Lesion sites before and after ablation.

In our spectroscopic characterization of ablation lesions (Figure 2.2a,b) we observe that there are no distinct absorption peaks in the spectral range we investigated, with the exception of that at 420 nm, which appears the same as in the non-ablated tissue. The PA response at wavelengths around 500 and 600 nm is higher than that of fresh tissue. In the near infrared range, as in [20], we find that the lesion is characterized by an attenuation of the 760 nm peak associated with the optical absorption of haemoglobin and myoglobin.

2.3.2 Imaging parameters

SR and SNR

The most characteristic parameter available for identification and delineation of lesions within a single-wavelength PA image is the SR_L. In Figure 2.3, the mean SR_L exceeds the control (SR_N in red) for the range of 600 nm onward. The variability of the SR_L in our data set is large, likely resulting from intrinsic variability in tissue response at different locations. This impacts the reliability of lesion delineation. Nevertheless, from Figure 2.3 we can identify the wavelengths for maximum lesion to non-lesion contrast in single wavelength images to be 640, 680, 800 and 730 nm in decreasing contrast. From the transmission measurements using the black absorbing target behind the tissue, we conclude that the imaging range for full tissue illumination ranges from 600 to 1000 nm.

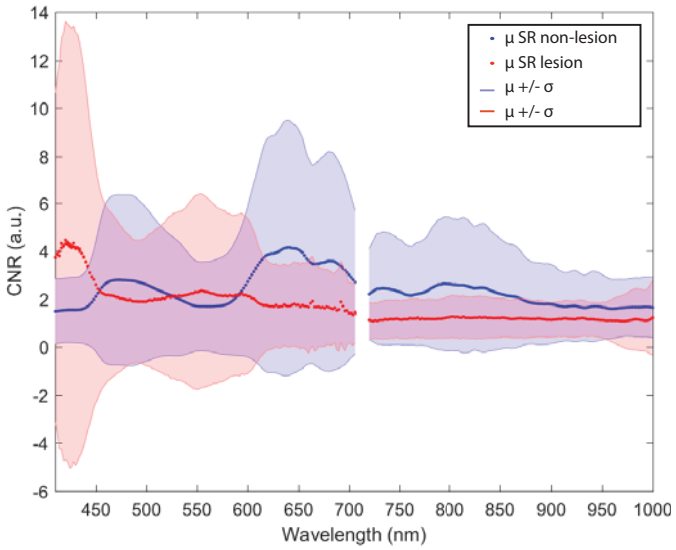

Figure 2.3 Variation of the SR across wavelengths for lesion and control sites. σ represents the standard deviation; μ represents the mean.

2.3.3 Imaging lesions

Single wavelength imaging

The analysis in section 2.3.2 suggests that the most suitable single wavelength for RF ablation lesion imaging, detection and delineation, is 640 nm. Figure 2.4a and Figure 2.5a show PA images of two different tissue samples (Figure 2.4d, Figure 2.5d), pre- and post-ablation at selected wavelengths including 640 nm. In Figure 2.4, two lesions were made, while in Figure 2.5, a single lesion is present. The photoacoustic images are normalized to the 95th percentile and displayed on a logarithmic scale. Inspection of the single-wavelength images in Figure 2.4a,c1 and Figure 2.5a,c2 shows that there is a variable increase of PA contrast in lesion sites by 2—10 dB, as observed in the SR assessment. In Figure 2.4a, focal enhancements can be appreciated in ablated sites, while in Figure 2.5a, there appears to be a homogeneous signal increase after ablation.

A movie of the ablation process in the right-hand lesion site in Figure 2.4 is available as Visualization 1 (Figure 2.4c1) . The frame rate is $\sim$ 0.4/s. We observe a slight increase in tissue thickness during ablation on ultrasound imaging. In the video, the lesion progress is perceptible as a gradual increase in PA signal but the lesion extent is poorly visible. Single wavelengths PA images acquired after the tissue cooled down show that the signal increase observed in Visualization 1 is not necessarily permanent. In Figure 2.5a, the lesion is indiscernible from the surrounding tissue. Lesion visibility was inconsistent over the data sets we have collected, reflecting the high standard deviations observed in our analysis in 2.3.2.

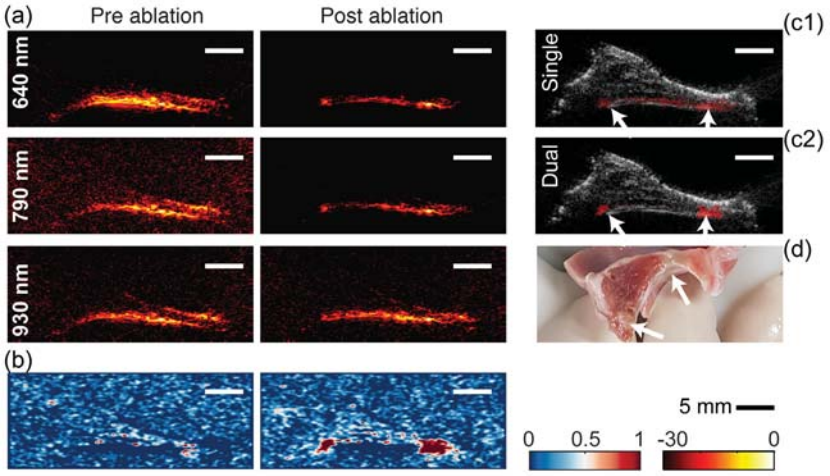

Figure 2.4 (a) Pre- and post-ablation PA images of a tissue sample at 640, 790 and 930 nm. (b) Dual wavelength images pre- and post-ablation. (c) Single wavelength (c1, Visualization 1) and dual wavelength (c2) images overlaid on ultrasound. (d) Photo of the tissue sample. Arrows point at the ablation sites.

Dual wavelength imaging

The slope of the signal variation with wavelengths in the near infrared range is different in the lesion areas than that in the non-ablated areas (Figure 2.2). We investigate the utility of this difference for identification and delineation of lesions by taking the ratio of signals at two wavelengths to distinguish lesion from untreated tissue. We evaluate the ratio of two-wavelength contrast ratios $Ø_L/Ø_N$ as described in 2.2.4, which we display in Figure 2.6. We look for maxima in this matrix, excluding the range where the standard deviation is greater than half the mean (white border), which would lead to increased sensitivity to the innate variability identified previously. The optimal wavelength pair emerging from this analysis is 790 +/- 10 nm and 930 +/- 10 nm.

We evaluate the imaging performance of a dual wavelength ratio imaging method using this optimal pair. We divide the fluence-corrected PA image at 790 nm by that acquired at 930 nm in both pre- and post-ablation acquisitions. We create images from this ratio, subtracting the background which arises from the (variable) noise in the PA image. Images of the example tissues we examined before are shown in Figure 2.4b and 2.5b. We observe that on pre-ablation images we see a uniform signal indicating the absence of lesions, and on post-ablation images we see bright signal at the lesion spots. In Figure 2.5, the lesion was not visible on any of the single wavelength post-ablation images, but becomes quite clear with the dual wavelength ratio imaging method. Figure 2.4b shows a case where the lesions' presence, lateral

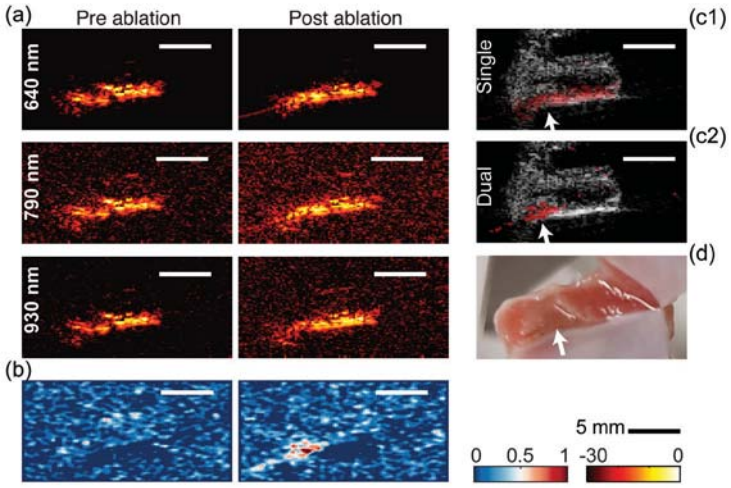

Figure 2.5 (a) Pre- and post-ablation PA images of a tissue sample at 640, 790 and 930 nm. (b) Dual wavelength images pre- and post-ablation. (c) Single wavelength (c1) and dual wavelength (c2) images overlaid on ultrasound. (d) Photo of the tissue sample. The arrow points at the ablation site.

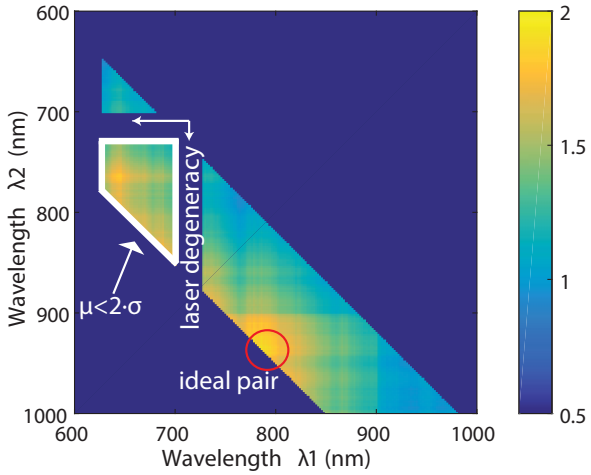

Figure 2.6 $\varnothing_L/\varnothing_N$ over all eligible wavelengths.

extent and transmurality is clearly visible with the proposed imaging method, compared to uncertain identification and impossible delineation with a single wavelength.

Quantitative performance evaluation

We quantitatively evaluate the performance of the proposed two-wavelength imaging technique by computing receiver-operator characteristic (ROC) curves. We apply different criteria for lesion identification and delineation, defined in 2.2.4. We compare two-wavelength imaging with two single-wavelength analyses, the optimal wavelength of 640 nm we identified based on the SR analysis, and 780 nm, which was previously identified as providing optimal contrast. The analysis is shown in Figure 2.7a and 2.7b.

The dual-wavelength analysis achieves an overall diagnostic accuracy of 0.97 for identification of lesions (comparing pre-/post-ablation) and also 0.97 for delineation (comparing lesions to neighboring control sites). The sensitivity and specificity at the operating point are 0.88 and 1.0, respectively, at a threshold of 0.39. The performance of any single wavelength imaging technique is inferior, with the optimal area under the curve (AUC) equal to 0.82 for lesion identification and 0.87 for delineation. We also find that 640 nm is consistently more effective than 780 nm for imaging RF ablation lesions.

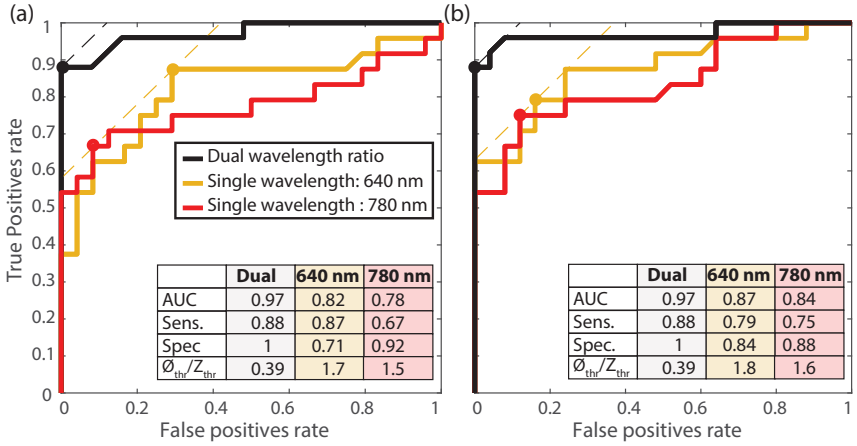

Figure 2.7 Comparison between the Receiver Operating Characteristics (ROC) curves for lesion detection (A) and lesion delineation (B) of dual wavelength imaging, and single wavelength imaging at 640 and 780 nm. (AUC: area under the curve, Sens.: sensitivity, Spec.: specificity).

The ROC analysis shows that the dual wavelength is more robust at detecting lesions. It also confirms that the dual wavelength imaging method proposed can highlight the lesion extent from the surrounding tissue better than a single wavelength imaging method.

2.4 Discussion

2.4.1 Contribution of this work

In this work, we present a photoacoustic spectroscopic characterization of ablation lesions in left atrial tissue. We introduce a dual wavelength (790/930 nm) imaging method which forms an image based on two consecutive frames acquired at two optical wavelengths. Advantages over single wavelength imaging approaches presented before [19, 20] are insensitivity to fluence and temperature variations, resulting in more robust lesion detection and delineation (important for assessing transmurality). Quantitatively, we find that the best-performing single wavelength is 640 nm, in contrast to 780 nm that was suggested previously, based on qualitative assessment in single lesions [19].

We also found the reproducibility of lesion visibility with a single wavelength monitoring to be inferior to our proposed dual wavelength imaging method. Indeed, the proposed method reduces the number of false negatives making it a more suitable imaging method for both lesion formation monitoring and depth extent evaluation as well as for post-ablation mapping. The proposed method reduces the variability in signal strength due to the differences in tissue sites and geometry (trabeculae vs. smooth). Further studies will be needed to evaluate the balance between these benefits and the increased cost of dual wavelength imaging.

The signal change from 790 nm to 930 nm for lesions follows a negative slope, while that of untreated tissue is rather constant. The ratio of the signal at these two wavelengths is > 1 for lesions and ≈ 1 elsewhere. Blood has oxy/haemoglobin as its main chromophores, which are spectrally very similar to oxy/myoglobin. The absorption ratio at the chosen wavelengths is ≤ 1, making dual wavelength imaging more robust than single wavelength image in a blood environment, as it is based on highlighting signal from chromophores with a negative slope in that same range.

We confirm the spectral signature observed by Dana et al. [20], as well as the increase in signal from ablated tissue observed by Pang et al. [19]. However, we find that the correlation based imaging proposed in [20] highlights also the artefacts caused by image reconstruction and that the correlation to non-ablated tissue remains high making it difficult at instances to identify lesions from the rest of the tissue.

2.4.2 Interpretation of spectra

The main chromophores in healthy myocardium tissue are myoglobin, cytochrome c and hemoglobin in their reduced, oxygenated and oxidized states, as well as water, lipid and collagen. Myoglobin dominates the optical absorption response of cardiac tissue in the examined range but the contributions of lipid, water and collagen become more significant in the near infrared. Our spectroscopy results of non-ablated tissue do consistently reflect this mix of chromophores. We identified oxygenation effects in the shape of myoglobin features: the more the tissue is exposed to air,

the more oxymyoglobin is formed. Therefore, the oxymyoglobin spectral signature in the visible range provides information on the freshness of the specimens received from the butcher. In fact, the flatness of the peak observed in our data set is representative of approximately 20% oxymyoglobin and 80% myoglobin on average. Sometimes there is also variability within the content of a sample (variation in tissue color Figure 2.4d). Indeed, in Figure 2.3, we note that the variability in SR_N is mainly representative of the variability of oxymyoglobin and myoglobin content of the tissue. The sharp variability observed at 690 and 660 nm could be associated with metmyoglobin formation.

RF ablation is a process where the tissue is heated over the transmission of radiofrequency current ($\sim$ 500kHz) through a resistive pathway to the indifferent electrode. The result of this process is the formation of coagulation necrosis associated with the denaturation of proteins [23]. Previous work on RF ablation lesion imaging based on optical methods, such as [24], reported lesions to be more optically scattering and to correspond better spectroscopically with the formation of metmyoglobin. Metmyoglobin is an oxidized form of myoglobin (where the heme iron within the porphyrin ring is oxidized to Fe^{3+}) [25]. The rate of auto-oxidation of myoglobin is accelerated at higher temperatures under specific pH conditions. However, this state is reversible and is not an indication of proper lesion formation [26]. In the larger spectral range we investigated, we found that the optical absorption changes effected by ablation are not consistent with metmyoglobin formation. The denaturation process occurring during RF ablation is one in which proteins decompose and lose their spatial conformation. In the case of myoglobin, two of the resultants of such a process are denatured globin (optically transparent) and heme groups that form new compounds called hemichromes [27]. The spectrum we observe in lesions corresponds to that reported of hemichromes [28].

We performed our experiments on porcine cardiac tissue, which is a commonly used model for human cardiac tissue. We expect our proposed method to work on human tissue; indeed as reported by [10] the optical changes in porcine and human tissue due to ablation are similar with the human tissue being slightly more scattering. AF is often associated with an underlying disease called atrial fibrosis [29]. In this disease tissue is mechanically and structurally remodelled to contain more collagen; the targeted tissue is thus perhaps slightly different in structure and composition in comparison with the healthy pigs we have used. Nevertheless, the spectral absorption of collagen in the range of 790 to 930 nm would also yield a negative ratio value as opposed to the positive ratio value found for lesions. The denaturation of collagen results in gelatine [30] which would result in a positive ratio value [31], similar to the lesions we observed.

2.4.3 Future work and considerations for application

Future studies will explore the relation between ratio values and degree of ablation. Other studies such as [24, 32] noticed that the change in signal within the ranges of 600 to 700 nm, and 800 to 960 nm could possibly be an indicator of the degree of ablation. Moreover, we will also analyze lesion features on ultrasound for a more robust lesion assessment relying on a dual imaging modality scheme with the proposed PA dual wavelength imaging.

Finally, we have demonstrated the ability to visualize RF ablation lesions on ex vivo porcine tissue. We do anticipate similar results on cryo and microwave ablation lesions as they were reported to be histologically similar to RF ablation lesion [33]. Our setup likely has higher image resolution and greater sensitivity than can be expected from intracardiac echography probes, and represents a motionless and bloodless environment. Nevertheless, we foresee that our method should work in a clinical environment. Indeed, lesion formation is a slow process ($\sim$ 30, 60 s), and current laser repetition rates and pulse-to-pulse wavelength tuning should be enough to monitor ablation. Irrigated catheters effectively displace the blood at the ablation site. In order to translate this work to a more practical catheter-based illumination setup, we will focus on dedicated catheters for PA-guided ablation.

2.5 Conclusion

We have characterized the photoacoustic signal from fresh and ablated porcine left atria tissue specimens over the range of 410 to 1000 nm. The changes we observe can be interpreted in terms of known irreversible processes occurring in thermal protein denaturation. We have demonstrated that imaging lesion formation using the ratio of two wavelengths achieves a diagnostic accuracy of 97% and displays a sensitivity of 88% and specificity of 100% at detecting and delineating lesions from the surrounding tissue, for an optimal wavelength pair of 790 and 930 nm. This method outperforms single-color imaging at any wavelength in the investigated range: ablated tissue generates a higher PA signal than untreated tissue but the variability in the enhancement is too large to provide reliable image contrast. Dual-wavelength ratio-based imaging removes the need of modelling the PA signal variation with tissue attenuation and temperature, which are relatively independent of temperature. The technique we explore in this study can be translated to intracardiac imaging with the application of modified ablation catheters for light delivery and ICE probes for signal detection.

Acknowledgements

The authors would like to thank Paul Knops, Robert Beurskens, Ayla Hoogendoorn, Maaike te Lintel Hekkert, Patricia Spicht, Klazina Kooiman and Richard van Duin for their help with the setup preparation.

Disclosure

The authors declare that there are no conflicts of interest related to this article.

References

[1] J. Heeringa, D. A. M. van der Kuip, A. Hofman, J. A. Kors, G. van Herpen, B. H. C. Stricker, T. Stijnen, G. Y. H. Lip, and J. C. M. Witteman, "**Prevalence, incidence and lifetime risk of atrial fibrillation: The rotterdam study,**" *European heart journal,* vol. **27**, pp. 949-953, 2006.

[2] A. Bajpai, I. Savelieva, and A. J. Camm, "**Epidemiology and economic burden of atrial fibrillation,**" *US Cardiovasc Dis,* vol. **1**, pp. 14-7, 2007.

[3] S. H. Hohnloser and Y. G. Li, "**Drug treatment of atrial fibrillation: What have we learned?,**" *Current Opinion in Cardiology,* vol. **12**, pp. 24-32, Jan 1997.

[4] C. Blomstrom-Lundqvist, M. M. Scheinman, E. M. Aliot, J. S. Alpert, H. Calkins, A. J. Camm, W. B. Campbell, D. E. Haines, K. H. Kuck, B. B. Lerman, D. D. Miller, C. W. Shaeffer, W. G. Stevenson, G. F. Tomaselli, E. M. Antman, S. C. Smith, J. S. Alpert, D. P. Faxon, V. Fuster, R. J. Gibbons, G. Gregoratos, L. F. Hiratzka, S. A. Hunt, A. K. Jacobs, R. O. Russell, S. G. Priori, J. J. Blanc, A. Budaj, E. F. Burgos, M. Cowie, J. W. Deckers, M. A. A. Garcia, W. W. Klein, J. Lekakis, B. Lindahl, G. Mazzotta, J. C. A. Morais, A. Oto, O. Smiseth, and H. J. Trappe, "**Acc/aha/esc guidelines for the management of patients with supraventricular arrhythmias - executive summary a report of the american college of cardiology/american heart association task force on practice guidelines and the european society of cardiology committee for practice guidelines (writing committee to develop guidelines for the management of patients with supraventricular arrhythmias),**" *Circulation,* vol. **108**, pp. 1871-1909, Oct 14 2003.

[5] L. Ganjehei, M. Razavi, and A. Rasekh, "**Catheter-based ablation of atrial fibrillation: A brief overview,**" *Tex Heart Inst J,* vol. **38**, pp. 361-3, 2011.

[6] M. Wright, "**Real-time atrial wall imaging,**" *Heart Rhythm,* vol. **12**, pp. 1836-1837, 2015.

[7] A. C. Lardo, E. R. McVeigh, P. Jumrussirikul, R. D. Berger, H. Calkins, J. Lima, and H. R. Halperin, "**Visualization and temporal/spatial characterization of cardiac radiofrequency ablation lesions using magnetic resonance imaging,**" *Circulation,* vol. **102**, pp. 698-705, Aug 8 2000.

[8] R. J. Hunter, D. A. Jones, R. Boubertakh, L. C. Malcolme-Lawes, P. Kanagaratnam, C. F. Juli, D. W. Davies, N. S. Peters, V. Baker, M. J. Earley, S. Sporton, L. C. Davies, M. Westwood, S. E. Petersen, and R. J. Schilling, "**Diagnostic accuracy of cardiac magnetic resonance imaging in the detection and characterization of left atrial catheter ablation lesions: A multicenter experience,**" *Journal of Cardiovascular Electrophysiology,* vol. **24**, pp. 396-403, Apr 2013.

[9] C. P. Fleming, L. M. Barwick, K. J. Quan, and A. M. Rollins, "**In-vitro characterization of ablation lesions using oct,**" *Circulation,* vol. **118**, pp. S831-S832, Oct 28 2008.

[10] R. P. Singh-Moon, C. C. Marboe, and C. P. Hendon, "**Near-infrared spectroscopy integrated catheter for characterization of myocardial tissues: Preliminary demonstrations to radiofrequency ablation therapy for atrial fibrillation,**" *Biomedical Optics Express,* vol. **6**, pp. 2494-2511, Jul 1 2015.

[11] D. A. Gil, L. M. Swift, H. Asfour, N. Muselimyan, M. A. Mercader, and N. A. Sarvazyan, "**Autofluorescence hyperspectral imaging of radiofrequency ablation lesions in porcine cardiac tissue,**" *J Biophotonics,* Aug 22 2016.

[12] M. Granier, P. F. Winum, M. Granier, P. Liaud, G. Cayla, P. Messner, J.-L. Pasquie, and I. Schuster, "**Real-time atrial wall imaging during radiofrequency ablation in a porcine model,**" *Heart Rhythm,* vol. **12**, pp. 1827-1835, 2015.

[13] T. Szili-Torok, G. P. Kimman, D. Theuns, J. Res, J. R. Roelandt, and L. J. Jordaens, "**Visualisation of intra-cardiac structures and radiofrequency lesions using intracardiac echocardiography,**" *Eur J Echocardiogr,* vol. **4**, pp. 17-22, Mar 2003.

[14] M. Wright, E. Harks, S. Deladi, F. Suijver, M. Barley, A. van Dusschoten, S. Fokkenrood, F. Zuo, F. Sacher, M. Hocini, M. Haissaguerre, and P. Jais, "**Real-time lesion assessment using a novel combined ultrasound and radiofrequency ablation catheter,**" *Heart Rhythm,* vol. **8**, pp. 304-12, Feb 2011.

[15] J. F. Ren, F. E. Marchlinski, D. J. Callans, and E. S. Zado, "**Echocardiographic lesion characteristics associated with successful ablation of inappropriate sinus tachycardia,**" *Journal of Cardiovascular Electrophysiology,* vol. **12**, pp. 814-818, Jul 2001.

[16] S. A. Eyerly, M. Vejdani Jahromi, D. M. Dumont, G. E. Trahey, and P. D. Wolf, "**The evolution of tissue stiffness at radiofrequency ablation sites during lesion formation and in the peri ablation period,**" *Journal of cardiovascular electrophysiology,* vol. **26**, pp. 1009-1018, 2015.

[17] W. Shi, A. Anand, S. Sethuraman, S. W. Huang, H. Xie, H. Agarwal, P. Yan, J. Azevedo, J. Kruecker, G. Ng, V. Shamdasani, W. Pritchard, J. Karanian, and B. Wood, "**Monitoring of radiofrequency ablation with shear wave delay mapping,**" *2015 Ieee International Ultrasonics Symposium (Ius),* 2015.

[18] W. Kwiecinski, J. Provost, R. Dubois, F. Sacher, M. Haissaguerre, M. Legros, N. D. An, R. Dufait, M. Tanter, and M. Pernot, "**Quantitative evaluation of atrial radio frequency ablation using intracardiac shear-wave elastography,**" *Medical Physics,* vol. **41**, Nov 2014.

[19] G. A. Pang, E. Bay, X. DeÁN-Ben, and D. Razansky, "**Three-dimensional optoacoustic monitoring of lesion formation in real time during radiofrequency catheter ablation,**" *Journal of cardiovascular electrophysiology,* vol. **26**, pp. 339-345, 2015.

[20] N. Dana, L. Di Biase, A. Natale, S. Emelianov, and R. Bouchard, "**In vitro photoacoustic visualization of myocardial ablation lesions,**" *Heart Rhythm,* vol. **11**, pp. 150-157, 2014.

[21] G. M. Hale and M. R. Querry, "**Optical constants of water in the 200-nm to 200-µm wavelength region,**" *Applied optics,* vol. **12**, pp. 555-563, 1973.

[22] J. S. Prahl Scott. (17-07-2017). *Optical absorption of water compendium*. Available: http://omlc.org/spectra/water/abs/index.html

[23] S. K. S. Huang and M. A. Wood, ***Catheter ablation of cardiac arrhythmias e-book***: Elsevier Health Sciences, 2014.

[24] J. Swartling, S. Palsson, P. Platonov, S. B. Olsson, and S. Andersson-Engels, "**Changes in tissue optical properties due to radio-frequency ablation of myocardium,**" *Medical & Biological Engineering & Computing,* vol. **41**, pp. 403-409, Jul 2003.

[25] P. Tomicki, ***Thermal stability and color change of myoglobin in model systems***: University of Guelph, 1999.

[26] M. C. Hunt, O. Sørheim, and E. Slinde, "**Color and heat denaturation of myoglobin forms in ground beef,**" *Journal of Food Science,* vol. **64**, pp. 847-851, 1999.

[27] L. Kristensen and H. J. Andersen, "**Effect of heat denaturation on the pro-oxidative activity of metmyoglobin in linoleic acid emulsions,**" *Journal of agricultural and food chemistry,* vol. **45**, pp. 7-13, 1997.

[28] R. H. Bremmer, A. Nadort, T. G. van Leeuwen, M. J. C. van Gemert, and M. C. G. Aalders, "**Age estimation of blood stains by hemoglobin derivative determination using reflectance spectroscopy,**" *Forensic Science International,* vol. **206**, pp. 166-171, Mar 20 2011.

[29] B. Burstein and S. Nattel, "**Atrial fibrosis: Mechanisms and clinical relevance in atrial fibrillation,**" *Journal of the American College of Cardiology,* vol. **51**, pp. 802-809, Feb 26 2008.

[30] F. Bettelheim, W. Brown, M. Campbell, S. Farrell, and O. Torres, ***Introduction to general, organic and biochemistry***: Nelson Education, 2012.

[31] S. K. V. Sekar, I. Bargigia, A. Dalla Mora, P. Taroni, A. Ruggeri, A. Tosi, A. Pifferi, and A. Farina, "**Diffuse optical characterization of collagen absorption from 500 to 1700 nm,**" *Journal of Biomedical Optics,* vol. **22**, p. 015006, 2017.

[32] J. J. Xia, A. Weaver, D. E. Gerrard, and G. Yao, "**Heating induced optical property changes in beef muscle,**" *Journal of Food Engineering,* vol. **84**, pp. 75-81, Jan 2008.

[33] H. Aupperle, N. Doll, T. Walther, C. Ullmann, H. A. Schoon, and F. Wilhelm Mohr, "**Histological findings induced by different energy sources in experimental atrial ablation in sheep,**" *Interact Cardiovasc Thorac Surg,* vol. **4**, pp. 450-5, Oct 2005.

Chapter 3

Photoacoustic-enabled RF ablation catheters for lesion monitoring

Sophinese Iskander-Rizk, Geert Springeling, Pieter Kruizinga,
Robert H.S. Beurskens, Antonius F.W.van der Steen and Gijs van Soest.

Published in
IEEE International Ultrasonics Symposium (IUS), 2018

Abstract

Atrial fibrillation is a cardiac arrhythmia stemming from abnormal electrical conduction/ impulse formation in the atria. To restore cardiac rhythm an RF ablation (RFA) procedure, interrupting aberrant electrical patterns, is commonly performed. One way of improving the procedure (current success rate ~ 60%) is to enable visual feedback on lesion progression, thereby reducing complications linked to over- ablation and mitigating recurrent conductivity due to under-ablation. To visualize the ablation process, we propose photoacoustic (PA) imaging using an ablation catheter for light delivery and an ICE (Intracardiac Echo) catheter for signal reception In this work, we demonstrate two PA-enabled ablation catheters which provide sufficient optical intensity to image fresh and ablated porcine tissue ex vivo.

3.1 Introduction

Atrial fibrillation is a cardiac arrhythmia stemming from abnormal electrical conduction/impulse formation in the atria. To restore cardiac rhythm an RF ablation procedure, interrupting aberrant electrical patterns, is commonly performed. During the procedure the ablation catheter is inserted into the left atrium through a transeptal puncture guided by an intracardiac echo (ICE) probe. Electroanatomical maps (EAM), which are volumetric rendering of the atrial cavity structure and potentials, are generally used to guide and record treatment at identified electrically abnormal areas. Information on delivered treatment (i.e. induced lesions) is deduced from a combination of parameters provided by different sensors at the ablation catheter tip [1]. Indeed, RF ablation (RFA) catheters carry nowadays more and more functionality. They provide temperature, impedance, contact force estimates and can also integrate electromagnetic sensor for localization and angular apposition determination. RF energy is generally delivered in a unipolar mode through an irrigated tip catheter, which features a flush channel to cool the tissue surface while ablating. The development of different catheter types and sensory feedback at the ablation catheter tip was driven by the need to improve RF energy transfer to tissue, mainly for adequate and predictable lesion formation, but also to avoid complications related to excess of energy delivery [2, 3]. Different catheters may generate different lesion profiles, and the ablation system can be used in two modes, namely power controlled or temperature controlled. Cardiologists need to interpret multiple sensor feedbacks to determine the end point of ablation for different cardiac loci and to prevent potential threats to patient safety (formation of steam pops, delivering energy to underlying nerves structures or organs etc.). However, the presence of fat or vessels can change the profile of the delivered energy and temperatures reached in the tissue, complicating the interpretation of the various sensor readouts. This yields incomplete lesion profiles, or worse excess of energy delivery leading to unwanted complications such as tamponade. One way to reduce potential procedural risks and to ensure good lesion formation profiles is to develop an imaging tool for direct lesion visualization and ablation evaluation.

Optically, to the naked eye, ablation lesions are quite discernible from the rest of the tissue, both from the surface of the endocardium and through the depth of the myocardium. Absorption of a nanosecond laser pulse by tissue generates (photo) acoustic waves detectable by ultrasound transducers. Based on this principle, photoacoustic imaging maps the absorption of light by tissue. It was previously shown that lesions and untreated tissue have different photoacoustic absorption spectra, and that these spectral differences are sufficient to image lesions and distinguish them from the rest of the tissue [4-6]. In addition to that, previous work characterized signals generated from PA-enabled ablation catheters [7, 8]. Unlike in [7] we propose separating the illumination source from the receive transducer. Also, unlike [8], we propose modifying an RFA catheter to deliver light, and receiving the

generated photoacoustic signals (PA) with an ICE to visualize the lesion formation process and identify lesion loci and extent. In this work, we investigate and evaluate two RF ablation catheter designs enabling photoacoustic imaging of ablation lesions. We evaluate light delivery capability, signal generation extent as well as lesion identification capability within this restricted illumination geometry. Finally, we discuss the impact of the metallic electrode on the photoacoustic imaging capability.

3.2 Methods and materials

3.2.1 RF ablation catheter design and evaluation

We modified commercially available RFA catheters (Blazer, EPT9620K2 Boston Scientific Marlborough, MA, USA) and replaced the irrigation channel either with one single optical fiber of 400 µm, 0.39 NA (FT400EMT, Thorlabs, Newton, NJ, USA) at the center of the catheter tip (Design A) or three 200 µm optical fibers of 0.5 NA (FP 200ERT, Thorlabs, Newton, NJ, USA) surrounding the catheter tip (Design B). A new electrode made of stainless steel was glued instead of the original one. This way, we retained the steering capability of the catheter while allowing the delivery of light for PA signal generation. The positions of the fibres are such that the illumination direction is parallel to the direction of the catheter shaft, as shown in Figure 3.1a,b. The ablation catheters were compatible with the EPT 1000 XP APM ablation system (Boston Scientific, Marlborough, MA, USA).

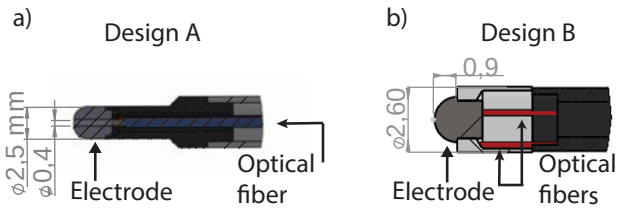

Figure 3.1 (a) Catheter design including one single optical fiber through its center: design A. (b) Catheter design including three optical fibers surrounding the ablation electrode : design B.

To evaluate light delivery, we coupled the modified RF ablation catheters to a tungsten halogen lamp (LS-1, Ocean optics, Largo, FL, USA) and measured the beam profile (BP209, Thorlabs, Newton, NJ, USA) at about 2 mm distance from the catheter tip. For characterization of tissue imaging capability, we analyzed PA images obtained with both catheters and evaluated imaging depth and signal extent. Finally, to further evaluate the effect of the illumination spot size on the signal generated we acquired images at different catheter-tissue distances pre and post ablation.

3.2.2 Imaging setup

We imaged fresh porcine left atrium specimens in a transmission mode photoacoustic setup (Fig. 3.4d). We positioned the prototype catheter at the endocardium side and the transducer at the epicardium side. We used a linear array transducer (192 channels, L12-3v, Verasonics, Redmond, Washington) connected to a Verasonics Vantage 256 research ultrasound system to collect the photoacoustic signals. The laser source (Vibrant B-355II, Opotek, Santa Clara, CA, USA) was tuned between 790 nm and 930 nm. We acquired two sets of images, before ablation and after ablation. The tissue was submerged in a HEPES buffer. Ablation settings were $P \leq 28W$, $t \leq 45s$. We positioned a black plastic absorber, from plastisol, after the tissue to assess transmission of light through the tissue. Detecting PA signal from the black plastic absorber means that enough light is transmitted from the catheter to penetrate the tissue slab and reach the surface of the phantom. One imaging frame was composed of pulse echo plane wave ultrasound (US) at 3 different angles (-18˚, 0, +18˚). The photoacoustic signals were averaged over 6 laser pulses per wavelength (λ). The final images were normalized to the 95th percentile signal.

3.3 Results

3.3.1 Evaluation of catheter designs

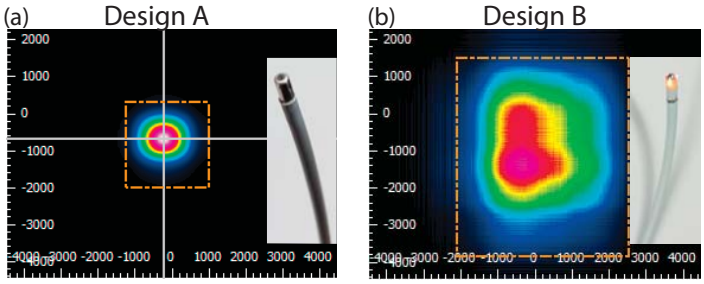

Figure 3.2 (a) Beam profile ~2 mm from the tip of catheter design A shown in the photograph inset. (b) Beam profile ~2 mm from the tip of catheter design B shown in the photograph inset. The axis units are in μm.

From a design and fabrication point of view, the single fiber catheter, design A, is simpler (Fig. 3.1). It is easier to couple to a laser source with less risks of damage at the catheter input. The laser light needs only to be shaped to match the opening angle of the one single fiber, while for the multiple fibers bundled with glue, this won't be achievable. In addition to that, the multiple fiber catheter damage threshold is lower

than its single fiber counterpart, limited by the glue damage threshold. Therefore, the coupling efficiency achieved with the catheter incorporating three fibers, design B, is only 60% of that of the single fiber design. However, catheter design B has the advantage of illuminating a larger tissue area, but at the cost of a lower fluence. In Figure 3.2, we observe that the illumination spot for catheter design A is about 1.5 x 1.5 mm diameter (Gaussian) at a distance of 2 mm, while that of catheter design B is about 4.5 x 4.2 mm at a similar distance as measured by the device software. The illumination profile from catheter design A is quite symmetrical and Gaussian, but that from catheter design B presents asymmetrical peak fluence spots. The catheters were tested for ablation and illumination and both capabilities were achieved. Lesion profiles achieved with both catheters were slightly different, but due to the multi-factorial nature (contact, force, angle, tissue width etc.) of the lesion formation process we cannot conclude whether the difference observed was directly related to the dissimilarities between electrodes or not.

3.3.2 Imaging capability

Each design compromised one of two aspects, namely illuminated area and fluence distribution, as can be seen on Figure 3.2. Thus to evaluate the influence of the two parameters we compared images obtained with the two catheters on fresh and ablated porcine left atria with the catheter held far away from the tissue surface.

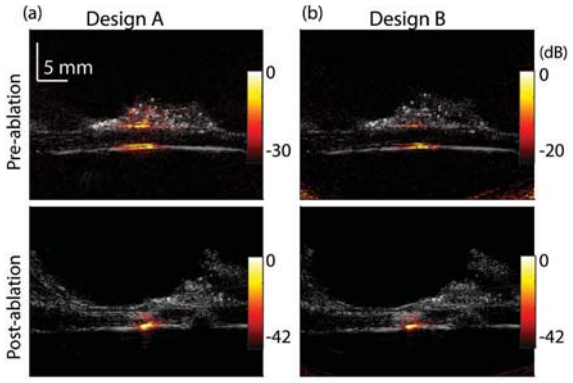

Figure 3.3 Comparison of different catheter illumination geometries on the PA image. Overlay of US image in gray scale over PA image in yellow-red scale (dynamic range US 40 dB), (a) using catheter design A for illumination and (b) using catheter design B for illumination.

Figure 3.3 shows that, prior to ablation, regardless of the catheter design, both walls (endocardium and epicardium) generated signal. After ablation we observed signal from the lesion area only. The PA signal after ablation was in general higher than prior

to ablation. The fluence from catheter design A was ~ 120 mW/cm^2 at 10 Hz and that of design B was ~ 6 mW/cm^2 at 10 Hz. PA signals generated using catheter design A were higher in amplitude than those using catheter design B, as expected. However, despite the larger illumination spot of catheter design B, the signal extent achieved laterally with both designs is the same: ~5 mm before ablation, and ~ 3 mm after ablation. The black plastic absorber positioned after the tissue generated PA signals in all imaging cases. This means that both catheter designs transmitted enough light to penetrate the whole tissue slab.

3.3.3 Distance to catheter effect

The illumination spot size is expected to change with respect to the distance of the catheter from the tissue. Since we are imaging in an aqueous solution, we don't expect a large increase in light attenuation at the studied wavelengths, but we do expect decrease of fluence with increasing separation distance. We advanced the catheter farther and closer to the tissue to evaluate the effect of the catheter on imaging. When monitoring the formation of ablation lesions the catheter needs to lie against the tissue surface. The fact that the catheter tip is metallic (to conduct RF current) makes generation of PA signals at the catheter tip unavoidable.

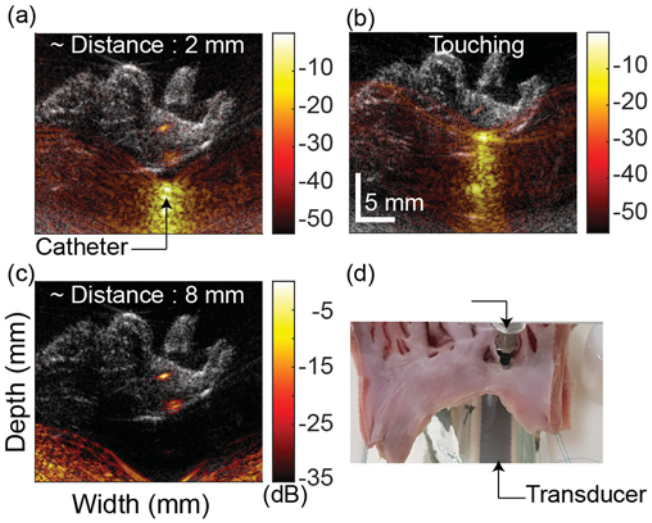

Figure 3.4 PA image variations due to varying the catheter-tissue distance prior to ablation. Overlay of US image (40dB dynamic range) in gray scale over PA image at 790 nm in yellow-red scale. (a) The catheter (Design A) is positioned 2 mm away from the tissue. (b) The catheter is slightly pushing against the tissue as can be noticed from the displaced tissue in gray scale. (c) The catheter is farther away from the tissue. (d) Photograph of the setup detailing the respective positioning of the catheter, tissue and transducer.

In Figure 3.4a the catheter shows a strong signal, generating significant echoic clutter around it. Figure 3.4 demonstrates how the image deteriorates (clutter, grating lobes) with the catheter in plane. As can be seen from the scale of the images in Figure 3.4, the metallic catheter tip saturates the image as it gets closer to the tissue. The dynamic range needs to be extended because the strongest PA emitting source in view is now the catheter rather than the tissue (Figure 3.4a,c). The intensity value of the PA signal generated by tissue increases as the catheter gets closer to the tissue, however the increase of tissue signal is not comparable to that of the signal from the catheter. When the catheter touched the tissue, the signal from the catheter tip was inseparable from the tissue signal at the endocardium.

We expected the imaging area to change with the distance of the catheter from the tissue, especially because we integrated optical fibers of high numerical aperture (NA). However this was not the case. The portion of tissue generating a signal is about 3 mm laterally and 5 mm in depth regardless of the catheter position. In Figure 3.4b, the signal from the tissue endocardial side is present, even when the catheter is in contact with the tissue.

When imaging ablated tissue (Figure 3.5), we observed that the detected signals were weaker (Figure 3.5a) at depth than prior ablation, but that the imaged region extended in a wider range laterally: ~4.5 mm. When we advanced the catheter closer, the signal from the catheter tip became more dominant, as in the pre ablation case.

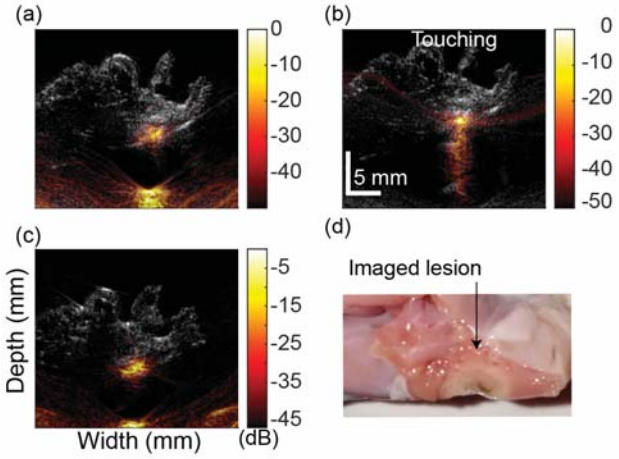

Figure 3.5 Overlay of US image (40dB dynamic range) in gray scale over PA image at 790 nm in yellow-red scale of fresh porcine tissue after ablation for different catheter-tissue distances. (a) The catheter (Design A) is positioned ~ 6 mm away from the tissue. (b) The catheter is slightly pushing against the tissue as can be noticed from the displaced tissue in gray scale. (c) The catheter is farther and laterally displaced illuminating a different portion of the tissue. (d) Photograph of the lesion made.

The PA signal from ablated tissue is stronger than from untreated tissue; this is noticeable when comparing the signal of tissue to that from the catheter tip. While Figure 3.4 and 3.5 were obtained with catheter design A, similar results were obtained when using catheter design B.

3.3.4 Identifying lesions

In Figures 3.4b and 3.5b, the tissue signal is hardly separable from the catheter tip. This is a major issue, especially since the proposed solution suggests to monitor the formation of lesion while ablating with the same probe.

Previously, we have shown that lesion progression and extent can be identified in contrast to untreated tissue by taking the PA image ratios at 790 nm over that at 930 nm [6] (Chapter 2). We showed that these dual wavelength images were more robust at lesion identification than single wavelength images. If we take such ratio images (Figure 3.6) we can see that the cluttering, artefact caused by the catheter touching the surface of the tissue is eliminated. Prior to ablation (Figure 3.6c,d), this ratio, based on the spectral differences found between ablated and untreated tissue, is lower than 1. Since the catheter response is spectrally flat, its signal is also eliminated from the images by thresholding to a ratio value of unity. This yields images without any PA signal prior to ablation. The ratio value for ablated tissue is higher than 1. In Figure 3.6a,b, the signal from the lesion becomes quite clear whether the catheter is in contact with the tissue or not, and the clutter due to the signal from the catheter tip is eliminated.

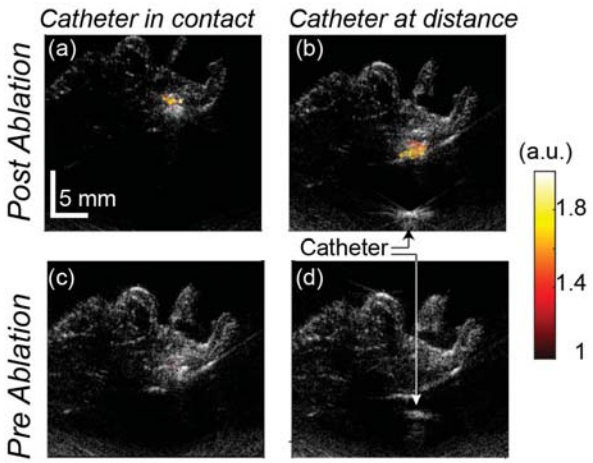

Figure 3.6 Dual wavelength image (PA790/PA930) overlaid on 40 dB US images (a) Ablated tissue with the catheter touching the tissue. (b) Ablated tissue with the catheter not in contact. (c) Non-ablated tissue with the catheter in contact. (d) Non-ablated tissue with the catheter not in contact.

3.4 Discussion

3.4.1 Generalization of results

The results obtained show capability of imaging ablated and untreated atrial tissue with a limited-view, catheter-based illumination source. We performed the experiments in a HEPES buffer solution, where optical path may be different than in blood. Therefore, the observations made on the tissue signal extent for different tissue-catheter distances may not be directly generalizable to the real case scenario. We observed that we could image a bigger region of the ablated tissue than the fresh tissue probably due to an increased optical scattering characteristic [9]. Perhaps, tissue perfusion and blood would increase the imaged surface as well.

In the future, a PA-enabled catheter could also provide depth temperature profiles during monitoring, as PA generation efficiency is temperature dependent [10]. This valuable information is unavailable to the physician at present.

3.4.2 Effect of Fluence disparity

In this study, we observed that a larger illumination area does not necessarily imply a larger imaged area. Indeed, the photoacoustic pressure is proportional to the delivered fluence as described by Equation 1.

$$p_0(z,\lambda) = \Gamma(z)\cdot\mu_a(z,\lambda)\cdot F(z,\lambda) \tag{1}$$

where F is the optical fluence, μa the local optical absorption coefficient and Γ the Grüneisen coefficient. With catheter design B we achieved a larger illumination area, but not necessarily sufficient fluence to generate a detectable signal in the entire illuminated volume. Therefore, we did not clearly observe a difference in image size, but rather observed a difference in image absolute signal intensity, which was weaker with design B. In other words, it seems that the minimum detectable signal is limited by a specific fluence threshold which is only reached near the center of the beam. We thus have a tradeoff between the area probed and the minimum signal detected by the transducer system for a certain coupled energy.

By taking the ratio of PA image at 790 nm to that at 930 nm, we circumvented the problems arising with fluence asymmetry and with signals at the catheter tip. Indeed, as long as sufficient light is sent to penetrate and generate detectable signals along the tissue depth then dual wavelength images will identify the presence/absence of lesion as well as its geometrical span. However, lesions bigger than $\sim$ 4mm in lateral extent may require moving the catheter along the tissue surface for a better volumetric evaluation of the lesion size.

3.5 Conclusion

The ideal PA-enabled RF ablation catheter shall deliver sufficient light to generate signals from the largest achievable tissue volume. Both designs presented here achieved similar minimum detectable fluence spot size contours in tissue despite their original difference in fluence profile at the catheter output. Dragging the catheter along the tissue surface would provide a more complete lesion extent laterally, overcoming the limitations of illumination with a small optical beam at the output of the catheter. Thus, catheter design shall target maximum fluence at depth. In this study, we observed that a dual wavelength method circumvents any saturation effects due to the PA signal generated at the catheter tip as well as mitigated effects of illumination asymmetry, making any further effort in catheter design optimization needless. However, it is important that any future catheter design takes into account an optimal light delivery to tissue for different catheter-tissue angular appositions.

References

[1] S. Nath and D. E. Haines, "**Biophysics and pathology of catheter energy delivery systems,**" *Progress in Cardiovascular Diseases,* vol. **37**, pp. 185-204, Jan-Feb 1995.

[2] D. E. Haines, "**The biophysics of radiofrequency catheter ablation in the heart - the importance of temperature monitoring,**" *Pace-Pacing and Clinical Electrophysiology,* vol. **16**, pp. 586-591, Mar 1993.

[3] N. P. Gallagher, E. C. Fear, E. J. Vigmond, and I. A. Byrd, "**Cathether contact geometry affects lesion formation in radio-frequency cardiac catheter ablation,**" *Conf Proc IEEE Eng Med Biol Soc,* vol. **2011**, pp. 243-6, 2011.

[4] G. A. Pang, E. Bay, X. DeÁN-Ben, and D. Razansky, "**Three-dimensional optoacoustic monitoring of lesion formation in real time during radiofrequency catheter ablation,**" *Journal of cardiovascular electrophysiology,* vol. **26**, pp. 339-345, 2015.

[5] N. Dana, L. Di Biase, A. Natale, S. Emelianov, and R. Bouchard, "**Iphotoacoustic visualization of myocardial ablation lesions,**" *Heart Rhythm,* vol. **11**, pp. 150-157, Jan 2014.

[6] S. Iskander-Rizk, P. Kruizinga, A. F. W. van der Steen, and G. van Soest, "**Spectroscopic photoacoustic imaging of radiofrequency ablation in the left atrium,**" *Biomedical Optics Express,* vol. **9**, pp. 1309-1322, Mar 1 2018.

[7] A. Nikoozadeh, J. W. Choe, S.-R. Kothapalli, A. Moini, S. S. Sanjani, A. Kamaya, Ö. Oralkan, S. S. Gambhir, and P. T. Khuri-Yakub, "**Photoacoustic imaging using a 9f microlinear cmut ice catheter**," in *Ultrasonics Symposium (IUS), 2012 IEEE International*, 2012, pp. 24-27.

[8] J. Rebling, F. J. Oyaga Landa, X. L. Dean-Ben, A. Douplik, and D. Razansky, "**Integrated catheter for simultaneous radio frequency ablation and optoacoustic monitoring of lesion progression,**" *Opt Lett,* vol. **43**, pp. 1886-1889, Apr 15 2018.

[9] J. Swartling, S. Palsson, P. Platonov, S. B. Olsson, and S. Andersson-Engels, "**Changes in tissue optical properties due to radio-frequency ablation of myocardium,**" *Medical & Biological Engineering & Computing,* vol. **41**, pp. 403-409, Jul 2003.

[10] E. V. Petrova, A. A. Oraevsky, and S. A. Ermilov, "**Red blood cell as a universal optoacoustic sensor for non-invasive temperature monitoring,**" *Applied Physics Letters,* vol. **105**, Sep 1 2014.

Chapter 5

Catheter design for intravascular photoacoustics

Sophinese Iskander-Rizk, Min Wu, Geert Springeling, Frits Mastik,
Robert H.S. Beurskens, Antonius F.W. van der Steen and Gijs van Soest.

Published in
Diagnostic and Therapeutic Applications of Light in Cardiology 2018
(Vol. 10471, p. 1047111). International Society for Optics and Photonics (SPIE).

Abstract

Intravascular photoacoustic/ultrasound imaging (IVPA/US) can image the structure and composition of atherosclerotic lesions identifying lipid-rich plaques ex vivo and in vivo. In the literature, multiple IVPA/US catheter designs were presented and validated both in ex-vivo models and preclinical in-vivo situations. Since the catheter is a critical component of the imaging system, we discuss here a catheter design oriented to imaging plaque in a realistic and translatable setting. We present a catheter optimized for light delivery, manageable flush parameters and robustness with reduced mechanical damage risks at the laser/catheter joint interface. We also show capability of imaging within sheath and in water medium. The optimized catheter allows imaging of human atherosclerotic coronary artery ex-vivo as well as of porcine diseased coronaries in-vivo.

5.1 Introduction

Coronary artery diseases (CAD) are the leading cause of death worldwide, posing a substantial health care and economic burden to society.[1] The first clinical manifestation of CAD is commonly acute coronary syndrome (ACS), which is mainly triggered by the rupture of vulnerable plaque and thrombosis.[2, 3] To treat ACS, percutaneous coronary interventions (PCI) are usually performed, placing a stent at the culprit lesion site in coronary artery. In PCI, an intravascular imaging modality which would potentially identify (asymptomatic) vulnerable plaque in addition to the culprit lesion is highly desirable for optimal stent placement, stent sizing, and for pre-emptive treatment of high-risk sites. In clinics, several imaging technologies are currently used for diagnostic assessment of coronary atherosclerosis, such as Intravascular UltraSound (IVUS), IntraVascular Optical Coherence Tomography (IVOCT) and Near InfraRed Spectroscopy (NIRS). However, none of the available imaging modalities provide conclusive identification of vulnerable plaque.[4]

Combined intravascular photoacoustic and ultrasound (IVPA/US) imaging is a powerful and promising alternative to identify vulnerable plaque.[5, 6] By using optical absorption contrast, IVPA imaging can discern the different components in a vulnerable plaque, and the co-registered IVUS imaging provides information on the artery wall structure. Successful plaque visualization was previously demonstrated ex vivo on animal or human samples.[7-9] Research efforts are ongoing to further develop IVPA/US imaging for clinical imaging. Recently, we demonstrated the first in vivo volumetric plaque imaging in a pig model [6], indicating the practicality of clinical translation of IVPA imaging. The dual modality catheter is critical for the imaging capability of the IVPA system.

Since IVPA imaging is based on transmitting light and receiving ultrasound, both a light delivery port and an acoustic transducer form an integral part of the IVPA catheter. Their relative configuration defines different catheter designs. There are mainly two types of IVPA catheter designs: one is with an offset (longitudinal or lateral) between the optical output and the acoustic transducer and the other is a co-linear catheter. The latter design can achieve a full overlap between the optical and acoustic beams and can thus accomplish a high signal sensitivity.[10, 11] However, this design is more prone to imaging artifacts due to near field optical scattering. The former design is more preferable for miniaturization despite its curved PA point spread function .[12] The smallest IVPA imaging catheter (0.9 mm) reported so far was fabricated based on the offset design.[13]

To achieve in vivo imaging, the IVPA imaging catheter must satisfy the following technical requirements: miniature, flexibility, safety, and robustness. Most implementations of IVPA to date have relied on clearance of the blood, meaning that the catheter should support flushing of the artery under study. A miniature, flexible, IVPA catheter capable of in vivo lipid imaging in pig model was developed in our previous

work.[6] In this paper, we discuss several design parameters and optimize the design of our previous catheter for practical in vivo imaging to optimize sensitivity and robustness. We quantified the optical and acoustical attenuation of different sheath materials and we show that by modifying the design of the distal optics we could minimize the imaging complications introduced by the sheath. The capability of the modified IVPA catheter is validated on ex-vivo measurements of human atherosclerotic coronary artery specimens through sheath and in water.

5.2 Materials and Methods

5.2.1 Modified catheter design

A typical IVPA imaging catheter mainly consists of a light delivery part, an acoustic transducer, a torque coil and an outer sheath. The different choices of material and configurations of these components lead to different imaging performances. We discuss here an offset design. There are two common configurations for the light delivery component: an angle-polished fiber or a forward-looking fiber ending at the surface of a reflecting mirror. The former configuration is easy to implement within a miniature tip design but comes at the expense of low optical coupling efficiency; the latter configuration has a better optical coupling efficiency but presents high risk of optical damage at the mirror end.

Our previous IVPA catheter used a 100 μm angle-polished (34˚) optical fiber for light delivery. Although it is capable of in vivo IVPA imaging, more than half of the laser light was lost in the path (only about 40% of input optical power was delivered out of the catheter). Another light delivery problem, though not related to the configuration of the light delivery at the tip, was a high susceptibility of optical and mechanical damage at the surface between the catheter and the optical rotary joint. To solve these problems, a modified light delivery part was developed. Figure 5.1a is an illustration of the new catheter tip. The diameter of the tip is of 0.8 mm without sheath. The length of the rigid tip is 2.2 mm. In the catheter, a 0.3 mm right angle prism (N-BK7 Edmund Optics) modified by silver sputtering (Agar Scientific Ltd., Essex, UK) in house was used to deflect the light beam from a 200 μm multi-mode fiber. The damage threshold of the modified prism is about 200 mJ/cm^2. To reduce the mechanical damage at the optical input of the catheter, an optical rotary joint coupling a 100 μm, 0.22 NA stationary beam of light to the rotating 200 μm fiber through a 50 μm air gap was developed in house (Figure 5.1b). This way we have reduced the susceptibility of damage (optically and mechanically) at the catheter and rotary joint surfaces. With the new optical rotary joint and the modified catheter design, 70 to 80% of the input laser light can be delivered out of the catheter. The same ultrasound transducer as used previously (40 MHz central frequency with 50% bandwidth, Blatek, USA) was placed at a distance of 0.4 mm and was tilted at 10˚ to

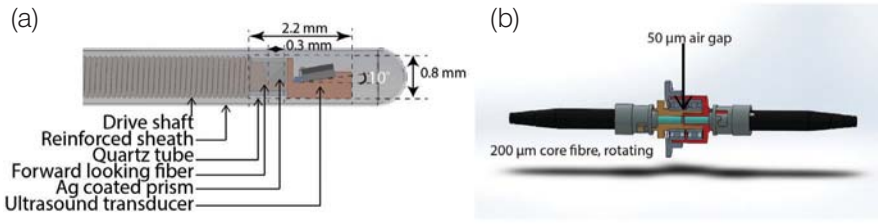

Figure 5.1 (a) Illustration of the catheter tip. (b) Illustration of the rotary joint. Ag: silver.

avoid the direct reflection from the sheath and to increase the dual beam overlap. The dual beam overlap starts at about 0.8 mm from the transducer. To prevent optical damage and contamination at the surface of the prism, we sealed the optical part (fiber and prism) with a small quartz tube. This prevents the formation of silver oxide, which impairs the optical damage threshold.

5.2.2 Outer sheath

The outer sheath is an essential component of the catheter for practical IVPA imaging because it prevents further damage to the artery wall than is already caused by the PCI. Identifying the ideal outer sheath material is one of the major challenges for the development of IVPA. The sheath material for IVPA imaging should be transparent for both ultrasound and light (at the wavelength of lipid detection), as well as offering enough mechanical support for intravascular application. With these requirements in mind, we performed an evaluation test on different types of medical sheath materials. The test was performed in water at room temperature at the wavelength of 1718 nm, using a 100 μm metal wire imaging target. We compared the peak to peak amplitude of the PA and US signals of the metal wire with and without sheath to quantify the PA and US attenuation due to the sheath. Figure 5.2 shows a typical PA and US signal of the metal wire with and without sheath. The PA and US attenuation ($Att_{PA/US}$) is defined as the lost PA (US) energy of the target signal in dB:

$$\mathrm{Att}_{\mathrm{PA/US}} = (\mathrm{E}^{\mathrm{PA/US}}_{\mathrm{no\ sheath}} - \mathrm{E}^{\mathrm{PA/US}}_{\mathrm{no\ sheath}})\mathrm{dB} \quad (1)$$

where $\mathrm{E}^{\mathrm{PA/US}}$ denotes the PA or US signal energy. Simply, by pulse-echo US imaging, the one-way acoustic attenuation,$Att_{acoustic}$, can be regarded as half of the US attenuation defined in Equation (1). While the optical attenuation, $Att_{optical}$, can be calculated as the difference between the PA attenuation and the one-way acoustic attenuation. Both the acoustic and optical attenuation should be positive.

$$\mathrm{Att}_{\mathrm{acoustic}} = 0.5 \cdot \mathrm{Att}_{\mathrm{US}} \quad (2)$$

$$Att_{optical} = \max(0, Att_{PA} - Att_{acoustic}) \quad (3)$$

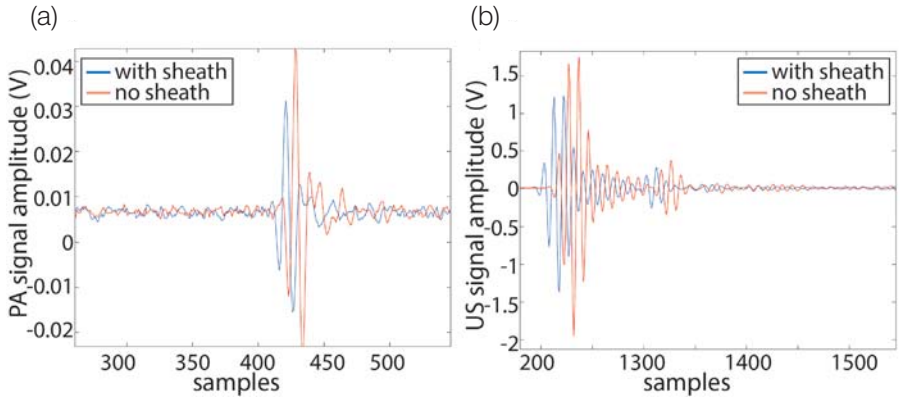

Figure 5.2 Typical signals received from (a) photoacoustic excitation of a 100 μm wire at 1718 nm and (b) pulse echo of that same wire. In blue are the signals received in presence of a sheath covering the catheter, and in red are the signals received without a sheath.

5.2.3 Real-time IVPA imaging system

The real-time IVPA imaging system capable of 20 fps includes: 5 kHz pulse rate laser source (FQ-OPO, Elforlight Ltd., Daventry, UK), scanning devices (rotation and translation), control unit and data display. Further details of the imaging system were previously described in.[14] Data were acquired in a continuous stream of frames, consisting of 250 A-lines per frame (PA and US) and 4000 samples per A-line at a sampling rate of 400 MHz.

5.2.4 Imaging of a funnel phantom

In order to evaluate experimentally the imaging depth and the intersection of the acoustic and optical beams along depth, we image a metallic funnel. The diameter of the inner circle at one of the extremities is of 1.5 mm and is increasing to 10 mm at the other extremity over a distance of 10 mm. Since the phantom is metallic we expect high amplitude echo and PA signal. The echo might saturate the receive chain. The measurement, done in water in the absence of sheath, provides us with a realistic measure of the optical and acoustic beam overlap within a medium which optical attenuation is well characterized in the literature. We repeat this measurement multiple times to evaluate the repeatability of the characterization. Indeed, because the catheter is flexible, it is not possible to control the orientation of the catheter with respect to the phantom wall; this makes the signal received dependent on the angle with which the transducer is facing the funnel wall.

5.2.5 Ex-vivo IVPA imaging on human coronary sample

A human coronary artery sample (LCX) was collected at autopsy from the Department of Pathology of Erasmus Medical Center (MC), after obtaining consent from the relatives. The research protocol was sanctioned by the Medical Ethics Committee of Erasmus MC (MEC-2007-081). The coronary artery was frozen within 2h after autopsy and stored at -80° until analysis a few months later. Prior to analysis, the artery was thawed and measured within a few hours. The volumetric IVPA/US measurement was performed at room temperature at the wavelength of 1720 nm using a maximum fluence of 35 mJ/cm^2 at the tissue surface. To evaluate the capability of the IVPA catheter, we performed a series of measurements on the same tissue sample under different conditions: without PE sheath in D_2O saline, with PE sheath in D_2O saline, without PE sheath in normal saline and with PE sheath in normal saline. This way we evaluated the effects of increased optical attenuation when using H_2O at 1700 rather than D_2O, as well as the effects of increased acoustical attenuation when using the catheter sheath, on the image interpretation and information conveyed. At least 200 frames of data were acquired for one pullback and the pullback speed was set to 0.5mm/s. All the IVPA/IVUS images were non-averaged. All the received data were filtered (band pass, median filter) and converted for display as in our previous work. After the measurement, we cut the imaged part of the artery sample, embedded in Optimal Cutting Temperature compound (Tissue-Tek®, Sakura Finetek Europe B.V., Alphen a/d Rijn, The Netherlands), and stored it at -80°C until further processing. For histology, we sliced the whole frozen artery block into a series of 10 μm thick sections. Oil Red O (ORO) staining was applied to all these sections to detect lipids.

5.3 Results

5.3.1 Sheath attenuation

Table 5.1 summarizes the decoupled optical and acoustic attenuation of all the sheath material we obtained. We find that FEP, PTFE and ETFE have no measurable optical attenuation based on their PA performance. Indeed, carbon–fluorine bonds (C-F) in the material do not absorb optical energy at the chosen wavelength. In other materials, carbon-hydrogen bonds (C-H) are responsible for the loss in optical power observed. Comparing all the listed materials, we find the PE sheath to be the best candidate for IVPA catheter if we also take into account malleability for artery accessibility. The NIRS tube shows the best performance for IVPA imaging, but its manufacturer or exact formulation is proprietary.

5.3.2 Catheter characterization

The imaging results from the funnel phantom are shown in Figure 5.3. Figure 5.3a shows the PA images at one selected A-line along the pullback direction. In the figure,

Table 5.1 Measured US and PA signal attenuation due to different sheath materials.

Sheath material	Optical attenuation(dB)	Acoustic attenuation(dB)
PE	1.5	1.2
FEP	0	12.5
ETFE	0	15.5
PTFE	0	6
Pebax	8.3	1.2
OCT sheath	3.4	3.3
NIRS sheath	0.5	0.3

PE = polyethylene, FEP = fluorinated ethylene propylene, ETFE = Ethylene tetrafluoroethylene , PTFE = Polytetrafluoroethylene.

the fundamental PA signal from the phantom and its multiple reverberations are clearly visible. Figure 5.3b shows the mean and standard deviation of the PA Signal to Noise Ratio (SNR) at different imaging depths. The statistics are computed from two pullback image sequences of the metallic funnel phantom and using the signals from all A-lines. The 20-dB imaging range is from 0.7 mm to 2.2 mm with the optimal imaging response observed at a depth of 1 mm. Since the measurement was performed in water we plot the attenuation of light by water vs. travelled distance (depth) for comparison. The attenuation from 1 to 1.5 mm attenuation could be attributed to water, the dip right before 2 mm to the design.

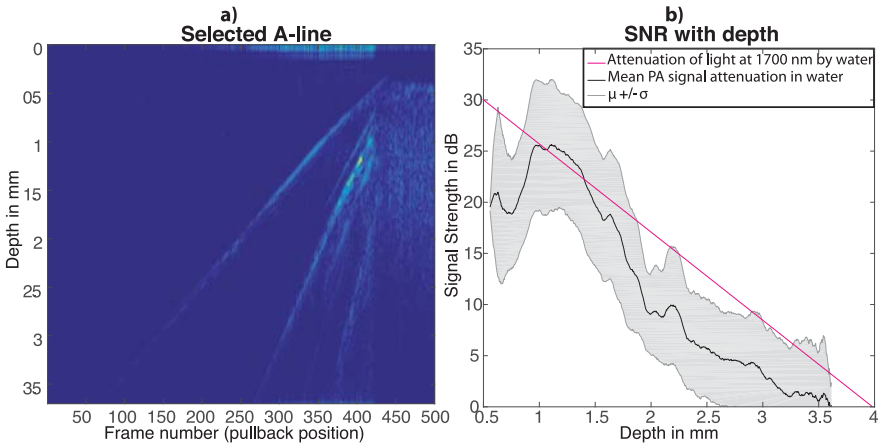

Figure 5.3 Evaluation of the PA signal with depth.(a) Selected A-line for different catheter positions along a metallic funnel length. (b) Variation in PA signal strength from a metallic funnel for different depths of imaging.

5.3.3 Ex vivo human coronary sample imaging

We imaged the same artery ex vivo in different settings. The same image frame for all acquisition settings was selected and displayed in Figure 5.4 The presence of the sheath (PE sheath) affects the ultrasound image significantly. Indeed, it impairs a clear identification of the lumen. On the photoacoustic images we are capable of identifying the plaque even through H_2O saline flush and tubing. The corresponding histology sections are shown in Figure 5.4e. We used the calcium to match the frames with one another and with the histology. The PA signal picked up through water and tube is ~10 dB lower than that through D_2O. In addition to that, comparing the signal strength in a peri-advential fat region at about 1.4 mm depth, we find that the PA signal is 1 to 2 dB lower when the tube is inserted, consistent with the wire test result presented in Table 5.1. We also find that the PA signal is about 10 dB lower in H_2O than in D_2O. The ultrasound signal is about 4 dB lower when the tube is inserted. These values are slightly different than the numbers reported in Table 5.1, perhaps due to the nature of the measurement being a fully processed pullback, with no beam-target angular control, versus a static measurement.

5.4 Discussion

Our work demonstrated a modified IVPA/US catheter design for the translation of IVPA/US to a clinical setting. A similar design was reported in[13, 15, 16], but not at this miniaturized level and with a protective glass tube. The miniaturization was challenging in terms of designing an optical delivery mechanism which is durable, resistant to damage due to contaminants and withstanding high energy fluences.

This modified IVPA/US catheter shows the big advantage of highly effective light coupling while significantly reducing the risk of optical and mechanical damage. The efficient light delivery is achieved by the unique combination of home-made silver coated micro-prism, the protective quartz tube as well as the air coupled rotary joint. We presented here the first evaluation report on different catheter sheath materials, a crucial step in making an IVPA catheter for practical imaging. Although the current PE sheath attenuates the PA signal, we still managed to image lipid-rich plaque human coronary artery samples in normal water ex vivo. The result can be significantly improved by changing the sheath material to the material used in the commercial NIRS catheter sheath or other fluorinated polymers. This work shows the capability of imaging lipid-rich plaques with IVPA in a more realistic setting, which allows flushing with normal saline instead of expensive heavy saline as used in most current IVPA experiments. Since blood and water have similar optical attenuation and diffraction properties at ~ 1700 nm, it could eventually be possible to achieve IVPA imaging of plaque without flushing[17].

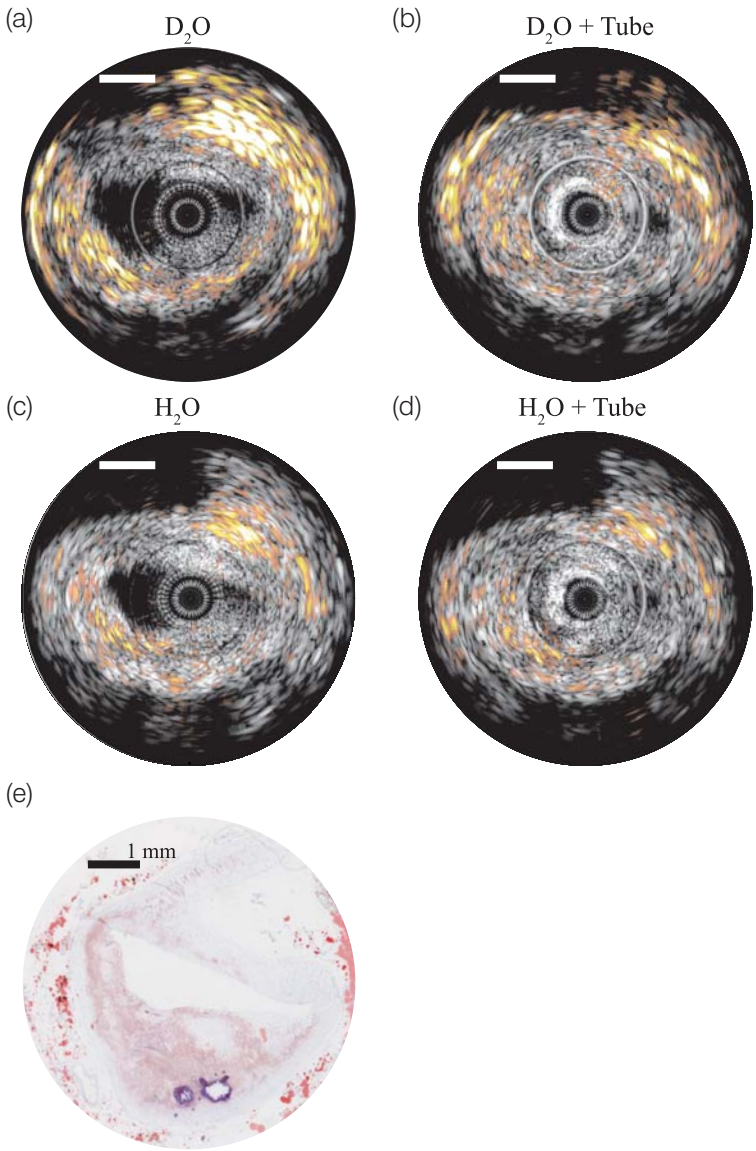

Figure 5.4 (a) Merged PA and US image on human coronary plaque acquired in D_2O saline and without sheath. (b) Merged PA and US image on human coronary plaque acquired in D_2O saline and through sheath. (c) Merged PA and US image on human coronary plaque acquired in normal saline and without sheath. (d) Merged PA and US image on human coronary plaque acquired in normal saline and through sheath. All images display a PA signal dynamic range of 15 dB and an US dynamic range of 35 dB. (e) The corresponding histology on the selected image cross section (Oil Red O staining, lipids are in red). Scale bar represents 1 mm.

We characterized the imaging depth of the catheter using a metallic phantom. During a pullback the angle between the phantom and the transducer is not necessarily perpendicular. This results in varying signal strength for a specified depth of image; this is reflected by the standard deviation of the PA signal attenuation (Fig. 5.3b). This angular variation affects in a similar fashion the US echo signal from the funnel as it is also variable for a set depth. Nonetheless, the PA signal amplitude variation matched the variation in acoustic echo.

The sheath effect is more prominent in imaging artefacts than in signal attenuation. In the absence of a sheath we could achieve very clear ultrasound images matching the structure on histology, while with the sheath, reverberations overlapped with the lumen border, affecting image interpretation. The photoacoustic images matched well with histology even with H_2O flush and through the tubing. Further work needs to be done to develop algorithms detecting sheath related artefacts on both PA and US images. Moreover, it may be possible to forgo flushing altogether, since optical scattering of blood at 1700 nm is small[18], but we did not test that situation.

5.5 Conclusion

The demonstrated modified flexible miniature IVPA catheter showed an improved imaging capability of lipid-rich plaque in addition to having a low damage risk (robustness), and manageable flushing. The proposed catheter design is thus closer to satisfying the requirements of an ideal IVPA imaging catheter for practical application. It would accelerate the translation of IVPA imaging to the clinics.

Acknowledgment

The authors would like to thank Andre Posthoorn, Astrid Moerman, Mirjam Visscher, Bowen Walen, Ruoyu Xing, Heleen van Beusekom, Ilona Peters.

References

[1] "**Cardiovascular diseases (cvds). ,**" *World Health Organization,* January 2015.

[2] E. Falk, P. K. Shah, and V. Fuster, "**Coronary plaque disruption,**" *Circulation,* vol. **92**, pp. 657-671, 1995.

[3] C. V. Bourantas, H. M. Garcia-Garcia, K. K. Naka, A. Sakellarios, L. Athanasiou, D. I. Fotiadis, L. K. Michalis, and P. W. Serruys, "**Hybrid intravascular imaging: Current applications and prospective potential in the study of coronary atherosclerosis,**" *Journal of the American College of Cardiology,* vol. **61**, pp. 1369-1378, 2013.

[4] G. van Soest, A. F. van der Steen, and E. Regar, "**Autofluorescence: A new nir on the block**," ed: Elsevier, 2016

[5] M. Wu, A. F. W. van der Steen, E. Regar, and G. v. Soest, "**Intravascular photoacoustic imaging of vulnerable atherosclerotic plaque: An emerging technology update,**" *International Cardiology review* vol. **11**, pp. 120-3, 2016.

[6] M. Wu, G. Springeling, M. Lovrak, F. Mastik, S. Iskander-Rizk, T. Wang, H. M. van Beusekom, A. van der Steen, and G. Van Soest, "**Real-time volumetric lipid imaging in vivo by intravascular photoacoustics at 20 frames per second,**" *Biomedical optics express,* vol. **8**, pp. 943-953, 2017.

[7] B. Wang, J. L. Su, J. Amirian, S. H. Litovsky, R. Smalling, and S. Emelianov, "**Detection of lipid in atherosclerotic vessels using ultrasound-guided spectroscopic intravascular photoacoustic imaging,**" *Optics express,* vol. **18**, pp. 4889-4897, 2010.

[8] M. Wu, K. Jansen, A. F. van der Steen, and G. van Soest, "**Specific imaging of atherosclerotic plaque lipids with two-wavelength intravascular photoacoustics,**" *Biomedical optics express,* vol. **6**, pp. 3276-3286, 2015.

[9] K. Jansen, M. Wu, A. F. van der Steen, and G. van Soest, "**Lipid detection in atherosclerotic human coronaries by spectroscopic intravascular photoacoustic imaging,**" *Optics express,* vol. **21**, pp. 21472-21484, 2013.

[10] Y. Cao, J. Hui, A. Kole, P. Wang, Q. Yu, W. Chen, M. Sturek, and J.-X. Cheng, "**High-sensitivity intravascular photoacoustic imaging of lipid–laden plaque with a collinear catheter design,**" *Scientific reports,* vol. **6**, p. 25236, 2016.

[11] P. Wang, T. Ma, M. N. Slipchenko, S. Liang, J. Hui, K. K. Shung, S. Roy, M. Sturek, Q. Zhou, and Z. Chen, "**High-speed intravascular photoacoustic imaging of lipid-laden atherosclerotic plaque enabled by a 2-khz barium nitrite raman laser,**" *Scientific reports,* vol. **4**, p. 6889, 2014.

[12] M. Wu, K. Jansen, G. Springeling, A. F. van der Steen, and G. van Soest, "**Impact of device geometry on the imaging characteristics of an intravascular photoacoustic catheter,**" *Applied optics,* vol. **53**, pp. 8131-8139, 2014.

[13] Y. Li, X. Gong, C. Liu, R. Lin, W. Hau, X. Bai, and L. Song, "**High-speed intravascular spectroscopic photoacoustic imaging at 1000 a-lines per second with a 0.9-mm diameter catheter,**" *J. Biomed. Opt,* vol. **20**, p. 065006, 2015.

[14] M. Wu, G. Springeling, M. Lovrak, F. Mastik, S. Iskander-Rizk, T. S. Wang, H. M. M. van Beusekom, A. F. W. van der Steen, and G. Van Soest, "**Real-time volumetric lipid imaging in vivo by intravascular photoacoustics at 20 frames per second,**" *Biomedical Optics Express,* vol. **8**, pp. 943-953, Feb 1 2017.

[15] A. B. Karpiouk, B. Wang, and S. Y. Emelianov, "**Development of a catheter for combined intravascular ultrasound and photoacoustic imaging,**" *Review of Scientific Instruments,* vol. **81**, Jan 2010.

[16] X. S. Bai, X. J. Gong, W. Hau, R. Q. Lin, J. X. Zheng, C. B. Liu, C. Z. Zeng, X. Zou, H. R. Zheng, and L. Song, "**Intravascular optical-resolution photoacoustic tomography with a 1.1 mm diameter catheter,**" *Plos One,* vol. **9**, Mar 20 2014.

[17] B. Wang, A. Karpiouk, D. Yeager, J. Amirian, S. Litovsky, R. Smalling, and S. Emelianov, "**In vivo intravascular ultrasound-guided photoacoustic imaging of lipid in plaques using an animal model of atherosclerosis,**" *Ultrasound in Medicine and Biology,* vol. **38**, pp. 2098-2103, Dec 2012.

[18] S. L. Jacques, "**Optical properties of biological tissues: A review,**" *Phys Med Biol,* vol. **58**, pp. R37-61, Jun 7 2013.

Chapter 6

In vivo intravascular photoacoustic imaging of plaque lipid in coronary atherosclerosis

Sophinese Iskander-Rizk*, Min Wu*, Geert Springeling, Heleen van Beusekom, Frits Mastik, Maaike te Lintel Hekkert, Robert Beurskens, Ayla Hoogendoorn, Eline Hartman, Antonius van der Steen, Jolanda Wentzel and Gijs van Soest.

Based on
EuroIntervention, 10.4244/EIJ-D-19-00318, 2019

Abstract

Aims: Intravascular photoacoustic (IVPA) imaging can visualize plaque composition in coronary arteries affected by atherosclerosis. Lipid-rich atherosclerotic plaques are the substrate of the majority of acute coronary syndromes (ACS). In the so-called "vulnerable plaque" paradigm, detection of such plaques would enable pre-emptive treatment of ACS, while also providing improved guidance of percutaneous coronary intervention. We present the first IVPA images of lipids in coronary atherosclerosis, obtained in vivo in an hyperlipidemic animal model.

Methods and results: Atherosclerosis was induced in familial-hypercholesterolemia Bretoncelles Meishan (FBM) swine fed a high-fat diet for 9 months. A custom-built IVPA/intravascular ultrasound (IVUS) catheter and imaging system were used to image coronary artery segments. Intravascular optical coherence tomography (IVOCT) and near-infrared spectroscopy (NIRS/IVUS) were deployed in the same vessels. After sacrifice, the coronary arteries were dissected from the heart and prepared for histological processing. IVPA showed an intimal lipid signal in areas where histology also showed positive lipid staining. When histology showed no lipids, IVPA was negative. In IVPA lipid-positive segments, IVOCT also suggested the presence of lipids locally, while NIRS was negative in absence of necrosis.

Conclusions: Plaque lipids were successfully imaged in vivo with IVPA in an animal model of coronary atherosclerosis.

6.1 Introduction

Ischemic heart disease, caused by impaired circulation in the coronary arteries, is the leading cause of death worldwide and is likely to remain in that position with globalization of Western diets and lifestyles to low- and middle-income countries. Lipid-rich atherosclerotic plaques in the coronary circulation are the culprit of the majority of acute coronary syndromes (ACS) and cardiac deaths [1, 2]. Such lesions have also been associated with adverse events after percutaneous coronary interventions (PCI) [3-5]. The clinically validated features that predispose a plaque for triggering an adverse event include the presence of a lipid-rich necrotic core, covered by a thin fibrous cap (thin-cap fibroatheroma; TCFA), plaque burden greater than 70%, and a minimal lumen area smaller than 4 mm^2 [4]. Prospective detection of such "vulnerable" plaques may enable pre-emptive interventions, and requires imaging of the composition and morphology of the lesion. Today's clinically available intravascular imaging technology cannot characterize all these features simultaneously [6]. While the high resolution of intravascular optical coherence tomography (IVOCT) is sufficient to identify the thin cap, it relies on subjective image interpretation for lipid detection [7]. IVOCT cannot directly quantify plaque burden, which is accessible by intravascular ultrasound (IVUS) only [8]. Near-infrared spectroscopy (NIRS), the only validated technology for lipid-core plaque detection [9, 10], lacks depth resolution so cannot measure cap thickness, although the combination with IVUS [11] does provide morphological imaging.

A technology to comprehensively characterize coronary atherosclerotic plaques is needed, and intravascular photoacoustic (IVPA) imaging has been proposed as a candidate [12]. Photoacoustic imaging relies on the detection of ultrasound waves that propagate after transient thermoelastic expansion, generated by optical absorption of short laser pulses [13]. Through the acoustic propagation delay, optical absorbers can be localized in the structure that can be conveniently imaged with ultrasound. Different tissue types and compositions can be imaged when varying laser wavelength. In photoacoustic imaging of atherosclerosis, plaque lipid has been the most prominent target [14-16]. IVPA has frequently been combined with IVUS, since the transducer used for photoacoustic signal detection can also make ultrasound images in pulse-echo mode. Multimodal IVPA/IVUS data provides a rich combination of structural and composition plaque imaging [15, 17]. The imaging resolution of IVPA is comparable with IVUS: down to 50 μm × 120 μm (axial × lateral) [18].

The intrinsically multimodal nature of IVPA implies that engineering a robust and sufficiently sensitive imaging catheter, coupled to a real-time imaging system [19, 20] is challenging. In vivo IVPA imaging of atherosclerotic lipids has been demonstrated in rabbit aorta injury models [21, 22] and peripheral vessels of hyperlipidemic swine [23], while imaging in the highly mobile and tortuous coronary arteries has been limited to artificial lipid targets [19]. In this study, we demonstrate IVPA imaging of intimal lipids in an animal model of coronary atherosclerosis, a crucial step in the clinical translation of this new modality.

6.2 Methods

6.2.1 Imaging system

The imaging system we used is schematically shown in Figure 6.1[19]; the catheter design was presented in Chapter 5, Figure 5.1a [24]. Briefly, a delay generator (BNC 575, Berkeley Nucleonics Corporation, San Rafael, CA, USA) triggered two lasers (FQ-OPO, Elforlight Ltd., Daventry, UK), an ultrasound pulser and a digital acquisition card (DAQ) (PX14400, Signatec, New York, NY, USA). Every A-line acquisition was composed of one pulse-echo and two photoacoustic acquisitions at a wavelength $\lambda \approx 1725$ nm. The compound A-line acquisition rate was 5 kHz, limited by the laser pulse repetition frequency. The catheter was rotated at 1200 rpm, resulting in 20 frames per second of 250 A-lines per frame. The pullback speed was 1 mm/s. The IVPA/IVUS catheter comprised a 40 MHz ultrasound single element transducer (50% bandwidth, Blatek, USA) and a 200 µm diameter optical fiber, enclosed in a flexible drive shaft (Asahi Intecc, outer diameter 0.8 mm). A silver coated prism deflected the light at the output of the catheter. The rotating core was fitted into the sheath of a commercially available NIRS/IVUS catheter (TVC Insight Coronary Imaging Catheter, Infraredx, Burlington, MA, USA), which had radiopaque markers. The lasers were coupled to the rotating optical fibre of the IVPA/IVUS catheter through a home-built rotary joint (Chapter 5, Fig5.1b). The laser pulse energy at the output of the catheter ranged between 40 and 50 µJ. Acquired data were amplified (43 dB; AU1263, Miteq, Long Island, NY, USA) and band-pass filtered (13-60 MHz 5th order Butterworth; built in-house) before digitization (14-bit, 400 MHz), processing and visualization.

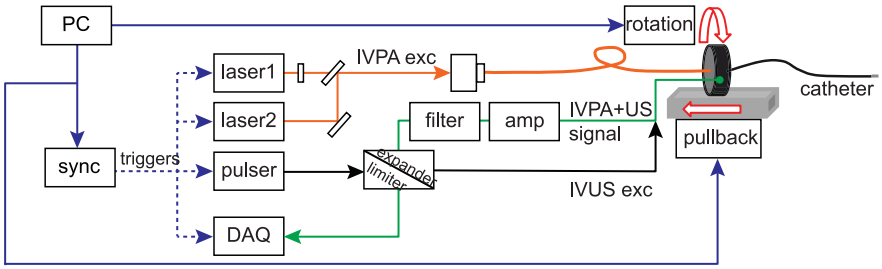

Figure 6.1 System diagram; purple: control and timing, orange: optical signal, black: analogue pulse signal, green: analogue received echo. DAQ: data acquisition; amp: amplifier.

6.2.2 Animal model and imaging protocol

Invasive imaging of the coronary arteries of a familial hypercholesterolemia Bretoncelles Meishan (FBM) mini swine [25] was performed. The swine was fed a restricted high fat diet (10% lard and 0.75% cholesterol, The National Institute of Agronomic Research,

France) for 9 months to promote atherosclerotic plaque development. The animal study, approved by the local animal ethics committee (DEC EMC3125 (109-12-25)) was performed according to the National Institutes of Health guide for the Care and Use of Laboratory animals [26]. The animal (castrated male, 74 kg) was sedated using a mix of Xylazine (2.25mg/kg, 20 mg/ml) and Zoletil 100 (tiletamine/zolazepam; 6 mg/kg, 100 mg/ml) injected intramuscularly. Anaesthesia was maintained by isoflurane inhalation (1–2.5% v/v). Through a sheath in the carotid artery, 250 mg of acetylsalicylic acid (Aspegic, Sanofi-Aventis Nederlands BV, Gouda, The Netherlands) and 10,000 I.U. of heparin (Heparine, Leo Pharma, Amsterdam, The Netherlands) were administered intra-arterially, the latter being subsequently injected every hour in dose of 5,000 I.U.

Access to the ostia of the right coronary artery (RCA) and the left anterior descending artery (LAD) was achieved by inserting a guiding catheter (Mach 1, 8F, Boston Scientific, Marlborough, MA, USA) through the carotid sheath. This process as well as imaging catheter positions (start and end of pullback) in the coronary arteries was guided by angiography. We imaged the coronary vasculature with three imaging modalities: IVPA/IVUS as described above, commercial IVOCT (Ilumien Optis with Dragonfly Optis catheter, St, Jude Medical, St. Paul, MN, USA) and NIRS/IVUS (TVC Insight Coronary Imaging Catheter, Infraredx, Burlington, MA, USA). The IVOCT pullback (36 mm/s) required the artery to be flushed from blood with contrast (Visipaque 320, GE Healthcare, Buckinghamshire, UK) under a constant flush rate of 4 ml/s (Medrad Injection System, Bayer HealthCare LLC, Whippany, NJ, USA). Similarly, the IVPA/IVUS pullback (1 mm/s) was performed under manual flushing of the artery from blood with a saline solution based on heavy water (deuterium oxide, D_2O), an optically clear liquid at the imaging wavelength. After imaging, animals were sacrificed by an overdose of pentobarbital (Euthasate AST farma, Oudewater, the Netherlands).

6.2.3 Data processing

Digital processing of the data acquired was performed on MATLAB (R2017b, The Mathworks, Natick, MA, USA). Ultrasound signals were band-pass filtered between 16 and 60 MHz, while photoacoustic signals were band-pass filtered between 14 and 21 MHz (4th order Butterworth). To accommodate for transmit artefacts, tubing artefacts and high frequency glitches, data were individually corrected for jitter and high-pass filtered across the A-lines to remove repeating signals. The samples representing the space within the catheter inner tube were blacked out. The two IVPA acquisitions in each A-scan were summed to improve signal-to-noise ratio (SNR). A 3D median filter of kernel 3×3×3 voxels was applied to suppress interference noise. Final images were used to assess lipid deposition in the vessel, and compared to histology and independent imaging.

Using angiographic guidance, it was confirmed that the NIRS/IVUS and IVOCT (pullback length of approximately 75 mm) fully covered the IVPA/IVUS pullbacks (length of 20-25 mm). The NIRS/IVUS and IVOCT pullbacks were matched by two

independent experts based on angiographic records and anatomic landmarks. IVPA/IVUS was matched to NIRS/IVUS based on angiographic position, side branches, and identifiable features on IVUS images of both modalities.

6.2.4 Histology

After imaging and animal sacrifice, the coronary arteries, including the ostium, were dissected from the epicardium, embedded for cryosectioning, and frozen on dry ice. Arteries were stored at -80˚C until further preparation for histology. For four locations (both vessel proximal and distal) we cut three sections separated by 4 mm; we estimate longitudinal vessel shrinking following dissection prior to freezing at 30%. These were stained with Oil-red-O (ORO), which stains lipids in pink/red, and counterstained by Hematoxylin.

6.3 Results

6.3.1 IVPA imaging results matched with OCT and NIRS/IVUS

The LAD and RCA of an FBM mini-pig were successfully imaged with IVPA/IVUS, NIRS/IVUS and IVOCT. In the LAD, stationary locations were imaged in both the distal and proximal segments of the artery. NIRS/IVUS did not detect lipid-rich plaque in either artery but revealed intimal thickening in the LAD and a near absence of abnormalities in the RCA. Inspection of the IVOCT confirmed these observations. Comparison of the IVUS images between the NIRS/IVUS and IVPA/IVUS data allowed matching of individual frames based on anatomical landmarks with high confidence; IVOCT could be matched using the same features.

6.3.2 IVPA/IVUS imaging

Inspection of the IVPA data in the LAD revealed a circumferential positive signal in the intimal layer (Figure 6.2a). A longitudinal section clearly shows that the signal has a repetitive pattern that follows the cardiac cycle, as is familiar from the well-known “sawtooth” artefact in IVUS pullbacks (Figure 6.2b). This supports the hypothesis that the signal originates from tissue and not from an artefactual source. The presence of circumferential dispersed lipids in the thickened intima is clearly visible in a histological section from the imaged vessel segment (Figure 6.2c), which also shows that there is no necrotic core. The intima in the IVOCT image at this site is heterogeneous, but not strongly attenuating as in advanced plaque [7], indeed suggestive of extracellular lipids. The NIRS-image is negative (Figure 6.2d), which is expected in the absence of necrosis.

More proximally in the LAD (Figure 6.3) the IVPA signal density in the intima diminishes. In Figure 6.3B, IVPA/IVUS indicates focal presence of intimal lipids (white arrowheads) and peri-adventitial lipids (blue arrowheads). IVOCT (Figure 6.3a) shows local areas with reduced signal, as observed in areas with extracellular lipid droplets

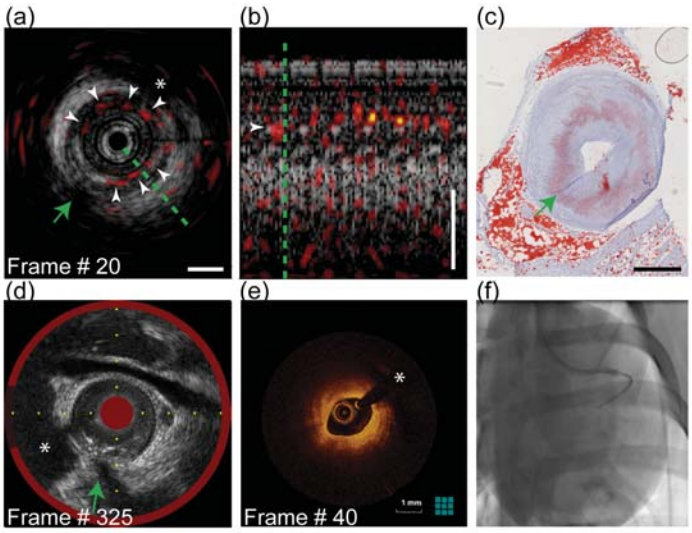

Figure 6.2 IVPA acquisition in the distal LAD of an FBM swine. (a) Overlay of IVPA images (red-yellow-white scale, dynamic range 20dB) on IVUS images (grayscale, dynamic range 30dB, scalebar represents 1 mm). Circumferential intimal lipids generate IVPA signal (white arrowheads). (b) Signal variation over seven heartbeats at the angular location indicated by the green line in A. (c) Corresponding histology indicates presence of lipids. (d) Corresponding NIRS/IVUS frame was negative for lipid-core plaque. (e) Matched IVOCT confirms presence of lipids. (f) Angiogram snapshot localizing the radio-opaque catheter. The green arrow in (a), (c) and (d) is the side branch ostium used for registration; * in (a), (d) and (e) is the guidewire artefact. IVPA: Intravascular photoacoustic imaging, LAD: left anterior descending artery, FBM: familial hypercholesterolemia Bretoncelles-Meishan, IVUS: intravascular ultrasound, NIRS: near-infrared spectroscopy, IVOCT: intravascular optical coherence tomography.

or proteoglycans. Histology (Figure 6.3d,e) also indicates that intimal lipid in this vessel segment is heterogeneously dispersed. The IVUS images acquired with IVPA show increased signal from the lumen, indicative of poor flush. The strongly absorbing H_2O water from blood mixed with D_2O flush media leads to an IVPA flush artefact as in IVOCT. Blood also attenuates the optical excitation. A strong guidewire-associated artefact is visible in the IVPA data in some of these images.

Compared to the LAD, less extensive disease was found in the RCA (Figure 6.4), according to the conventional imaging technologies IVOCT (Figure 6.4a), IVUS, and NIRS (Figure 6.4c). No intimal lipids were observed with IVPA (Figure 6.4b), with the exception of on small spot (white arrowhead). Detailed examination of this segment in Figure 6.4f demonstrates that the intimal signal does persist longitudinally and originates from tissue. Intimal lipids in the RCA could not be positively confirmed by histology (very faint coloring for lipids) or IVOCT (Figure 6.4a,d). A positive IVPA signal

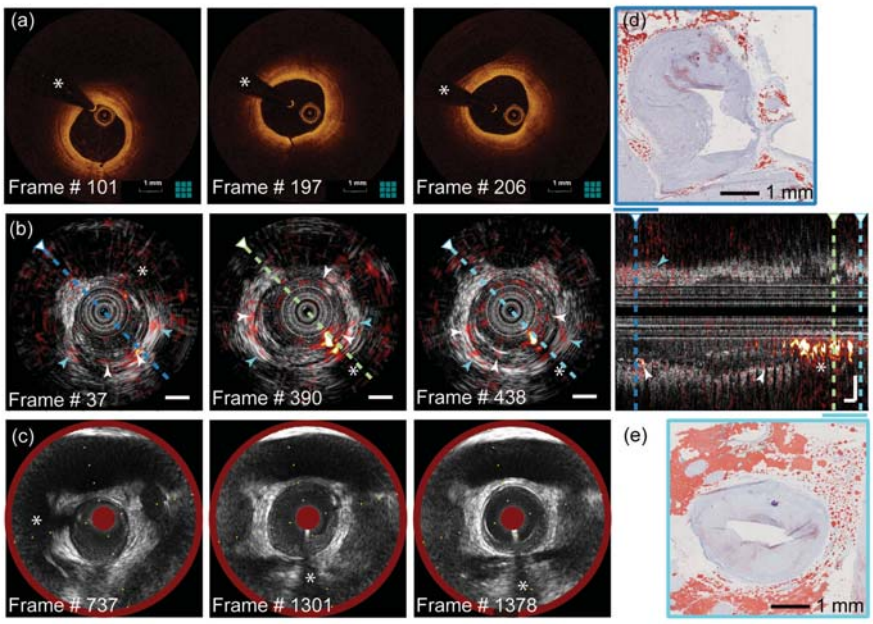

Figure 6.3 IVPA/IVUS acquisition in the proximal swine LAD. Selected frames and their matches in different modalities; (a) IVOCT; (b) IVPA/IVUS, including a longitudinal section; (c) NIRS/IVUS. Corresponding histological sections (d) in the distal and (e) proximal segments of the acquisition confirm that the vessel has focal intimal lipids as indicated by the images in (b) (white arrowheads), surrounded by perivascular fat (blue arrowheads). Scalebars are 1 mm; dynamic range as in Fig. 6.2. IVPA: Intravascular photoacoustic imaging, IVUS: intravascular ultrasound, LAD: left anterior descending artery, NIRS: near-infrared spectroscopy, IVOCT: intravascular optical coherence tomography.

close to the catheter does not coincide with tissue structure according to IVUS and is attributed to blood/flush media mixing Figure 6.4e). In the IVPA data in Figure 6.4b,e, peri-adventitial lipids are prominently visible (blue arrowheads).

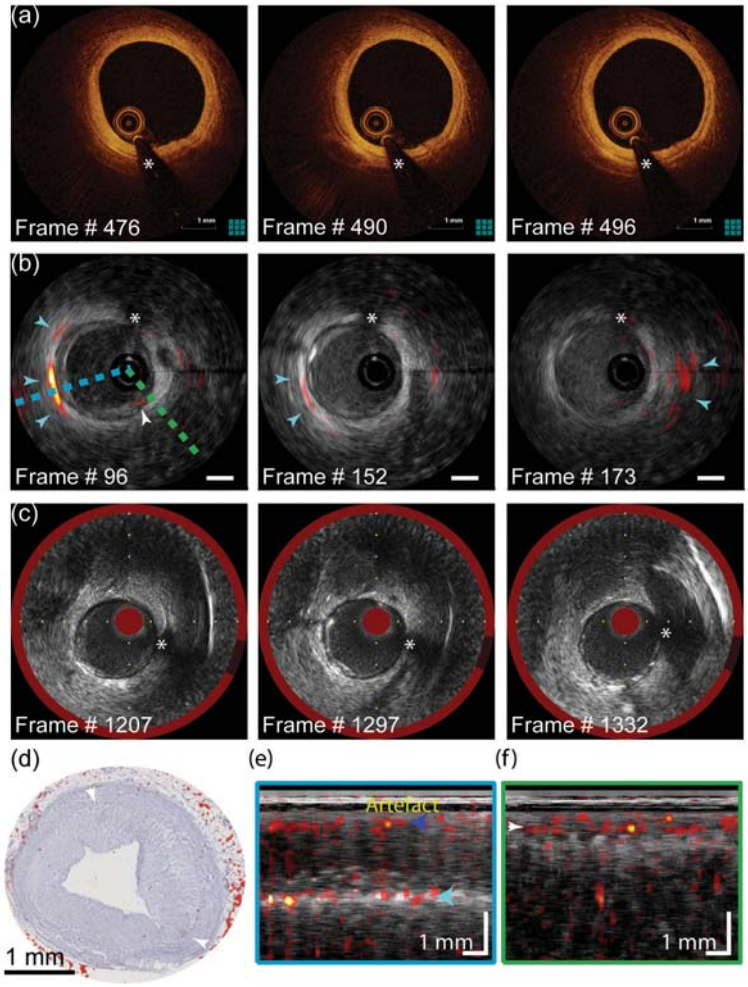

Figure 6.4 Matched IVOCT, IVUS/IVPA and NIRS/IVUS frames of pullback in the swine RCA. (a) IVOCT frames matched to locations in (b) and (c). (b) Merged IVPA/IVUS; the detected IVPA signal originates from peri-adventitial lipids (blue arrowheads). One site with intimal lipids is visible (white arrowhead). (c) NIRS/IVUS is negative for the whole RCA. (d) Histology confirms absence of major plaque lipids; white arrowheads indicate tiny positive spots for lipids. Longitudinal section through the IVPA/IVUS pullback in the swine RCA at the plane represented by the blue dotted line (e) and the green dotted line (f) shown in the cross-sectional images in (b). Arrows in (e) indicate peri-adventitial fat, and an artefact attributed to blood mixed with flush media. Scalebars are 1 mm; dynamic range as in Fig. 6.2. IVOCT: intravascular optical coherence tomography, IVUS: intravascular ultrasound, IVPA: intravascular photoacoustic imaging, NIRS: near-infrared spectroscopy, RCA: right coronary artery.

6.4 Discussion and Conclusion

6.4.1 In vivo coronary IVPA imaging

Lipids exhibit a few characteristic absorption bands [16, 27, 28] that photoacoustic imaging can target for identification and localization in tissue. In this study, we have shown that catheter-based IVPA can do this in vivo, in the highly mobile and difficult to access coronary circulation of an atherosclerotic swine model. Independent imaging with IVOCT, and histologic analysis, confirm the plaque lipid detection by IVPA. Compared to our previous in vivo work, improvements to the catheter geometry and data processing have enhanced the depth range of the IVPA signal. This makes it possible to see tissue lipids at various depths as evident from the images presented here. The imaging catheter and operation of the system are highly similar to clinically available IVUS; the difference being the need for flushing of the blood, at least at the wavelengths chosen in this experiment. Imaging of lipid-rich plaque during PCI may improve understanding of the risk for developing future ACS, and as such inform treatment strategy. Further development of the technology (e.g. catheter sheath, noise-suppressing electronics and dual-frequency transducer) and evaluation in clinical trials are needed to establish the utility of IVPA and imaging criteria that may improve outcomes.

6.4.2 Comparison to other modalities

Imaging of lipid-rich plaque has been a goal for intravascular imaging since the concept of the vulnerable plaque was established [29]. NIRS, a technology that we used in this study, aims to detect lipid-core plaque by doing optical reflection spectroscopy of the vessel wall through blood. A classification algorithm, trained on a large database of spectra in autopsy vessels, detects lipid-core plaque following a strict set of pathological criteria [9]. The NIRS colour scale represents the probability of finding lipid-core plaque in a circumferential arc. Since it is principally a sensing and not an imaging technology, it does not have depth resolution and cannot locate the lipid accumulation relative to the lumen boundary or other anatomical features. IVPA also uses the absorption spectrum to identify lipid, but in its current form uses fewer wavelengths and directly represents the signal amplitude, which is proportional to the absorption coefficient and the optical intensity [13]. In comparison with NIRS, IVPA assessment of lipids is not constrained by limited sampling of natural variability in an algorithm training set; however, IVPA may also detect perivascular adipose lipids and thus is potentially less specific. In the images presented in this study, peri-adventitial lipids signal could not be discriminated from plaque lipids by IVPA, whereas NIRS detects necrotic lipid-core plaque specifically [9]. Previous work has demonstrated that it is possible to make this distinction with dual [30] or multi [31] wavelength imaging. In this study, we did not pursue lipid differentiation due to the relatively high noise level in the IVPA data. Enhanced sensitivity of the catheter to photoacoustics signals below

the IVUS band [32], and other improvements in immunity to environmental noise sources in the system, may enable this distinction in future studies. Increased sensitivity will also eliminate the need for flushing with expensive D_2O, which also leads to artefacts similar to IVOCT imaging. IVPA lipid imaging through blood has been demonstrated [33]: 15-20 dB of imaging dynamic range through blood appears to be feasible for imaging up to a depth of about 3 mm, as observed in Figure 6.4e.
An alternative approach to discriminate between atherosclerotic and adipose lipids relies on segmentation of IVPA data using the IVUS images. In such an approach, identification of a lipid spot as intimal or perivascular will depend on the resolution and contrast of the IVUS images. In its present form, the resolution of IVUS and IVPA is insufficient to measure cap thickness, which can currently only be done by OCT. It is possible to assess the plaque lipid "in contact with the lumen", a criterion that is also applied in IVUS-VH analyses for identification of TCFA [4, 5]. In IVUS-VH and related techniques, analysis of ultrasound echo radio-frequency data identifies "necrotic core" tissue type; but the correspondence to actual tissue composition has proved challenging in the past [34, 35]. In contrast, IVPA robustly capitalizes on the well-documented absorption spectra of lipid molecules [36] to establish chemical tissue composition.

6.4.3 Limitations

This is a preclinical study, performed in a large-animal model of coronary atherosclerosis. Animal models cannot represent all aspects of human disease. We found extensive lipid-rich plaque in this animal, but no clear signs of necrotic core according to histology or NIRS, although necrotic core plaque was observed in this animal model previously [25]. Studies with IVPA on human autopsy coronary arteries have demonstrated consistent and strong signal from necrotic core plaque [15]. Future animal trials will have to demonstrate this capability with improved SNR. Data were acquired in one animal only; as a result, we do not have sufficient data to quantify the diagnostic accuracy of IVPA. These aspects of the study limit the scope of the conclusions that can be drawn from the results.

6.5 Conclusions

We have demonstrated in vivo IVPA imaging of coronary lipid-rich atherosclerotic plaque in a preclinical setting. Two arteries were examined. In one artery, extensive plaque was found in which IVPA showed a positive signal for intimal lipids. The other artery exhibited mild intimal thickening with sparse or no lipid. Both findings were confirmed by IVOCT imaging and histology. We realized a miniaturized, flexible catheter that could successfully be deployed in the coronary circulation of a swine for pullback imaging in an acquisition sequence similar to IVUS imaging. These results constitute a crucial step in the translation of IVPA towards clinical trials.

This study highlights the potential for future clinical translation of a new catheter-based technology for imaging lipids in atherosclerotic plaque, intravascular photoacoustic imaging. It identifies the presence of lipid-rich plaque, but importantly, it also locates the depth of these lipids relative to the lumen boundary as outlined by intravascular ultrasound, allowing an assessment of cap thickness. In the future, such data may provide a prospective, lesion-specific risk assessment for adverse cardiac events.

Acknowledgements

We thank Mathijs Stam for his assistance in preparation of histology.

Funding

This work was supported by the Netherlands Organization for Scientific Research (NWO), Vici 16131; NWO Applied and Engineering Sciences 12706 and the European Research Council (grant agreement 310457).

Conflicts of interest statement

The authors declare that there are no conflicts of interest.

References

[1] R. Virmani, F. D. Kolodgie, A. P. Burke, A. Farb, and S. M. Schwartz, "**Lessons from sudden coronary death - a comprehensive morphological classification scheme for atherosclerotic lesions,**" *Arterioscler Thrombosis And Vascular Biology,* vol. **20**, pp. 1262-1275, May 2000.

[2] E. Falk, M. Nakano, J. F. Bentzon, A. V. Finn, and R. Virmani, "**Update on acute coronary syndromes: The pathologists' view,**" *European Heart Journal,* vol. **34**, pp. 719-728, 2013.

[3] L. Xing, T. Higuma, Z. Wang, A. D. Aguirre, K. Mizuno, M. Takano, H. L. Dauerman, S. J. Park, Y. Jang, C. J. Kim, S. J. Kim, S. Y. Choi, T. Itoh, S. Uemura, H. Lowe, D. L. Walters, P. Barlis, S. Lee, A. Lerman, C. Toma, J. W. C. Tan, E. Yamamoto, K. Bryniarski, J. Dai, T. Zanchin, S. Zhang, B. Yu, H. Lee, J. Fujimoto, V. Fuster, and I. K. Jang, "**Clinical significance of lipid-rich plaque detected by optical coherence tomography: A 4-year follow-up study,**" *J Am Coll Cardiol,* vol. **69**, pp. 2502-2513, May 23 2017.

[4] G. W. Stone, A. Maehara, A. J. Lansky, B. de Bruyne, E. Cristea, G. S. Mintz, R. Mehran, J. McPherson, N. Farhat, S. P. Marso, H. Parise, B. Templin, R. White, Z. Zhang, and P. W. Serruys, "**A prospective natural-history study of coronary atherosclerosis,**" *N Engl J Med,* vol. **364**, pp. 226-235, Jan 20 2011.

[5] P. A. Calvert, D. R. Obaid, M. O'Sullivan, L. M. Shapiro, D. McNab, C. G. Densem, P. M. Schofield, D. Braganza, S. C. Clarke, K. K. Ray, N. E. J. West, and M. R. Bennett, "**Association between ivus findings and adverse outcomes in patients with coronary artery disease: The viva (vh-ivus in vulnerable atherosclerosis) study,**" *JACC: Cardiovascular Imaging,* vol. **4**, pp. 894-901, 2011.

[6] G. van Soest, L. Marcu, B. E. Bouma, and E. Regar, "**Intravascular imaging for characterization of coronary atherosclerosis,**" *Current Opinion in Biomedical Engineering,* vol. **3**, pp. 1-12, 2017/09/01/ 2017.

[7] G. J. Tearney, E. Regar, T. Akasaka, T. Adriaenssens, P. Barlis, H. G. Bezerra, B. Bouma, N. Bruining, J.-m. Cho, S. Chowdhary, M. A. Costa, R. de Silva, J. Dijkstra, C. Di Mario, D. Dudeck, E. Falk, M. D. Feldman, P. Fitzgerald, H. Garcia, N. Gonzalo, J. F. Granada, G. Guagliumi, N. R. Holm, Y. Honda, F. Ikeno, M. Kawasaki, J. Kochman, L. Koltowski, T. Kubo, T. Kume, H. Kyono, C. C. S. Lam, G. Lamouche, D. P. Lee, M. B. Leon, A. Maehara, O. Manfrini, G. S. Mintz, K. Mizuno, M.-a. Morel, S. Nadkarni, H. Okura, H. Otake, A. Pietrasik, F. Prati, L. Räber, M. D. Radu, J. Rieber, M. Riga, A. Rollins, M. Rosenberg, V. Sirbu, P. W. J. C. Serruys, K. Shimada, T. Shinke, J. Shite, E. Siegel, S. Sonada, M. Suter, S. Takarada, A. Tanaka, M. Terashima, T. Troels, S. Uemura, G. J. Ughi, H. M. M. van Beusekom, A. F. W. van der Steen, G.-A. van Es, G. van Soest, R. Virmani, S. Waxman, N. J. Weissman, and G. Weisz, "**Consensus standards for acquisition, measurement, and reporting of intravascular optical coherence tomography studies: A report from the international working group for intravascular optical coherence tomography standardization and validation,**" *Journal of the American College Of Cardiology,* vol. **59**, pp. 1058-1072, 2012.

[8] S. J. Nicholls, A. Hsu, K. Wolski, B. Hu, O. Bayturan, A. Lavoie, K. Uno, E. M. Tuzcu, and S. E. Nissen, "**Intravascular ultrasound-derived measures of coronary atherosclerotic plaque burden and clinical outcome,**" *J Am Coll Cardiol,* vol. **55**, pp. 2399-2407, May 25 2010.

[9] C. M. Gardner, H. Tan, E. L. Hull, J. B. Lisauskas, S. T. Sum, T. M. Meese, C. Jiang, S. P. Madden, J. D. Caplan, A. P. Burke, R. Virmani, J. Goldstein, and J. E. Muller, "**Detection of lipid core coronary plaques in autopsy specimens with a novel catheter-based near-infrared spectroscopy system,**" *JACC: Cardiovascular Imaging,* vol. **1**, pp. 638-648, Sep 2008.

[10] S. Waxman, S. R. Dixon, P. L'Allier, J. W. Moses, J. L. Petersen, D. Cutlip, J.-C. Tardif, R. W. Nesto, J. E. Muller, M. J. Hendricks, S. T. Sum, C. M. Gardner, J. A. Goldstein, G. W. Stone, and M. W. Krucoff, "**In vivo validation of a catheter-based near-infrared spectroscopy system for detection of lipid core coronary plaques: Initial results of the spectacl study,**" *J Am Coll Cardiol Img,* vol. **2**, pp. 858-868, July 1, 2009 2009.

[11] S. Garg, P. W. Serruys, M. van der Ent, C. Schultz, F. Mastik, G. van Soest, A. F. van der Steen, M. A. Wilder, J. E. Muller, and E. Regar, "**First use in patients of a combined near infra-red spectroscopy and intra-vascular ultrasound catheter to identify composition and structure of coronary plaque,**" *EuroIntervention,* vol. **5**, pp. 755-756, Jan 2010.

[12] K. Jansen, G. van Soest, and A. F. W. van der Steen, "**Intravascular photoacoustic imaging: A new tool for vulnerable plaque identification,**" *Ultrasound in Medicine & Biology,* vol. **40**, pp. 1037-1048, 2014.

[13] P. Beard, "**Biomedical photoacoustic imaging,**" *Interface Focus,* vol. **1**, pp. 602-31, Aug 6 2011.

[14] B. Wang, J. L. Su, J. Amirian, S. H. Litovsky, R. Smalling, and S. Emelianov, "**Detection of lipid in atherosclerotic vessels using ultrasound-guided spectroscopic intravascular photoacoustic imaging,**" *Opt. Express,* vol. **18**, pp. 4889-4897, 2010.

[15] K. Jansen, A. F. W. van der Steen, H. M. M. van Beusekom, J. W. Oosterhuis, and G. van Soest, "**Intravascular photoacoustic imaging of human coronary atherosclerosis,**" *Opt. Lett.,* vol. **36**, pp. 597-599, 2011.

[16] P. Wang, H.-W. Wang, M. Sturek, and J.-X. Cheng, "**Bond-selective imaging of deep tissue through the optical window between 1600 and 1850 nm,**" *Journal of Biophotonics,* vol. **5**, pp. 25-32, 2012.

[17] S. Sethuraman, S. R. Aglyamov, J. H. Amirian, R. W. Smalling, and S. Y. Emelianov, "**Intravascular photoacoustic imaging using an ivus imaging catheter,**" *Ieee Transactions on Ultrasonics Ferroelectrics and Frequency Control,* vol. **54**, pp. 978-986, May 2007.

[18] M. Wu, K. Jansen, G. Springeling, A. F. W. van der Steen, and G. van Soest, "**Impact of device geometry on the imaging characteristics of an intravascular photoacoustic catheter,**" *Applied Optics,* vol. **53**, pp. 8131-8139, Dec 1 2014.

[19] M. Wu, G. Springeling, M. Lovrak, F. Mastik, S. Iskander-Rizk, T. Wang, H. M. M. van Beusekom, A. F. W. van der Steen, and G. Van Soest, "**Real-time volumetric lipid imaging in vivo by intravascular photoacoustics at 20 frames per second,**" *Biomedical Optics Express,* vol. **8**, pp. 943-953, 2017/02/01 2017.

[20] D. VanderLaan, A. Karpiouk, D. Yeager, and S. Emelianov, "**Real-time intravascular ultrasound and photoacoustic imaging,**" *IEEE Transactions on Ultrasonics, Ferroelectrics, and Frequency Control,* vol. **PP**, pp. 1-1, 2016.

[21] B. Wang, A. Karpiouk, D. Yeager, J. Amirian, S. Litovsky, R. Smalling, and S. Emelianov, "**In vivo intravascular ultrasound-guided photoacoustic imaging of lipid in plaques using an animal model of atherosclerosis,**" *Ultrasound in Medicine and Biology,* vol. **38**, pp. 2098-2103, Dec 2012.

[22] J. Zhang, S. Yang, X. Ji, Q. Zhou, and D. Xing, "**Characterization of lipid-rich aortic plaques by intravascular photoacoustic tomography,**" *Ex Vivo and In Vivo Validation in a Rabbit Atherosclerosis Model With Histologic Correlation,* vol. **64**, pp. 385-390, 2014.

[23] A. Kole, Y. Cao, J. Hui, I. A. Bolad, M. Alloosh, J.-X. Cheng, and M. Sturek, "**Comparative quantification of arterial lipid by intravascular photoacoustic-ultrasound imaging and near-infrared spectroscopy-intravascular ultrasound,**" *Journal of Cardiovascular Translational Research,* November 28 2018.

[24] S. Iskander-Rizk, M. Wu, G. Springeling, F. Mastik, R. H. S. H. Beurskens, A. F. W. van der Steen, and G. van Soest, "**Catheter design optimization for practical intravascular photoacoustic imaging (ivpa) of vulnerable plaques,**" *Diagnostic and Therapeutic Applications of Light in Cardiology 2018,* vol. **10471**, 2018.

[25] T. Thim, M. K. Hagensen, L. Drouet, C. Bal Dit Sollier, M. Bonneau, J. F. Granada, L. B. Nielsen, W. P. Paaske, H. E. Botker, and E. Falk, "**Familial hypercholesterolaemic downsized pig with human-like coronary atherosclerosis: A model for preclinical studies,**" *EuroIntervention,* vol. **6**, pp. 261-8, Jun 2010.

[26] National Research Council Committee for the Update of the Guide for the Care and Use of Laboratory Animals, ***Guide for the care and use of laboratory animals***. Washington (DC): National Academies Press (US), National Academy of Sciences., 2011.

[27] K. Jansen, M. Wu, A. F. van der Steen, and G. van Soest, "**Photoacoustic imaging of human coronary atherosclerosis in two spectral bands,**" *Photoacoustics,* vol. **2**, pp. 12-20, 2014.

[28] R. R. Anderson, W. Farinelli, H. Laubach, D. Manstein, A. N. Yaroslavsky, J. Gubeli, 3rd, K. Jordan, G. R. Neil, M. Shinn, W. Chandler, G. P. Williams, S. V. Benson, D. R. Douglas, and H. F. Dylla, "**Selective photothermolysis of lipid-rich tissues: A free electron laser study,**" *Lasers Surg Med,* vol. **38**, pp. 913-9, Dec 2006.

[29] J. A. Schaar, J. E. Muller, E. Falk, R. Virmani, V. Fuster, P. W. Serruys, A. Colombo, C. Stefanadis, W. S. Casscells, P. R. Moreno, A. Maseri, and A. F. W. van der Steen, "**Terminology for high-risk and vulnerable coronary artery plaques,**" *European Heart Journal,* vol. **25**, pp. 1077-1082, June 2, 2004 2004.

[30] M. Wu, K. Jansen, A. F. W. van der Steen, and G. van Soest, "**Specific imaging of atherosclerotic plaque lipids with two-wavelength intravascular photoacoustics,**" *Biomedical Optics Express,* vol. **6**, pp. 3276-3286, 2015/09/01 2015.

[31] K. Jansen, M. Wu, A. F. van der Steen, and G. van Soest, "**Lipid detection in atherosclerotic human coronaries by spectroscopic intravascular photoacoustic imaging,**" *Optics Express,* vol. **21**, pp. 21472-21484, Sep 9 2013.

[32] V. Daeichin, M. Wu, N. De Jong, A. F. W. van der Steen, and G. van Soest, "**Frequency analysis of the photoacoustic signal generated by coronary atherosclerotic plaque,**" *Ultrasound in Medicine & Biology,* vol. **42**, pp. 2017-2025, 2016.

[33] B. Wang, A. Karpiouk, D. Yeager, J. Amirian, S. Litovsky, R. Smalling, and S. Emelianov, "**Intravascular photoacoustic imaging of lipid in atherosclerotic plaques in the presence of luminal blood,**" *Opt. Lett.,* vol. **37**, pp. 1244-1246, 2012.

[34] T. Thim, M. K. Hagensen, D. Wallace-Bradley, J. F. Granada, G. L. Kaluza, L. Drouet, W. P. Paaske, H. E. Botker, and E. Falk, "**Unreliable assessment of necrotic core by virtual histology intravascular ultrasound in porcine coronary artery disease,**" *Circ Cardiovasc Imaging,* vol. **3**, pp. 384-391, July 1, 2010 2010.

[35] E.-S. Shin, H. M. García-García, J. M. R. Ligthart, K. Witberg, C. J. Schultz, A. F. W. van der Steen, and P. W. Serruys, "**In vivo findings of tissue characteristics using imap™ ivus and virtual histology™ ivus,**" *EuroIntervention,* vol. **6**, pp. 1017-1019, 2011.

[36] R. T. Holman and P. R. Edmondson, "**Near-infrared spectra of fatty acids and some related substances,**" *Analytical Chemistry,* vol. **28**, pp. 1533-1538, 1956.

Chapter 7

Photoacoustic imaging of sub-diffraction objects with spectral contrast

Sophinese Iskander-Rizk, Pieter Kruizinga, Geert Springeling, Hendrik Vos, Antonius van der Steen and Gijs van Soest.

Published in
Optics letters, 42(2), 2017

Abstract

Photoacoustic imaging couples the chemical specificity of optical absorption with the viewing depth of ultrasound. Systems based on linear array transducers have the versatility to be applied in various (pre-) clinical scenarios, but face a tradeoff between viewing depth and image resolution depending on transducer frequency and aperture. We propose here a method to disentangle, with precision, small, closely spaced targets with optical spectral contrast, without impairing the imaging depth. Photoacoustic datasets were recorded at two different optical wavelengths. We accurately recovered object separation distances (mean error= 2.3±6 %) from the phase difference between signals across the array, down to a spacing of 1/20th of the system's beamformed lateral resolution. The proposed method may enable the translation of super-resolution microscopy to deep tissue imaging.

Photoacoustic imaging (PAI) is an emerging modality for biomedical imaging. It is based on the absorption of optical energy by chromophores in the tissue, which induces a thermoelastic expansion that can be detected by an acoustic transducer. PAI capitalizes on optical contrast, which has the potential to discern biological structures at the molecular level [1], and on ultrasound propagation, which has less wavefront distortion and thus a much larger penetration depth than regular optical imaging. Generally, there are three ways of implementing PAI. The first is PA microscopy, scanning a focused light source and/or a focused acoustic receiver across the object of interest. The second is PA computed tomography, enclosing the object with acoustic receivers and relying on a relatively large laser beam, propagating diffusely into scattering tissue, for illumination. The third, and most of interest to this study, is using broad-area illumination, and receiving with a limited transducer aperture [1]. This geometry is commonly called limited-view photoacoustic tomography (PAT). It is the easiest to translate into a clinical setting, because it allows the use of conventional handheld ultrasound transducers, requiring only the addition of a light source. It also has the potential for real-time imaging of either macroscopic details or microscopic ones; this is referred to as 'scalability' of PAT. However, this scalability has its limits: it is currently impossible to image both macroscopic and microscopic structures simultaneously; indeed, there is a tradeoff between imaging depth and resolution. Therefore, multiple imaging systems need to be deployed to assess different length scales [2].

Much effort has been put into improving the resolution of PAI. Several studies used custom-made ultrasound detectors with large apertures or large transverse sampling density to achieve a better image [3, 4]. Spatial modulation of the illumination pattern to improve the lateral resolution enabled imaging of structures 1.5 to 6 times smaller than the acoustic diffraction limit [5, 6]. In this work, we discuss a method based on a standard limited-view PAT setup, relying on imaging algorithms to enhance the imaging of microscopic structures at depth. It is inspired by super-resolution and single-molecule microscopy techniques [7, 8] and their acoustic analogue [9], enabling the localization of point-like sources by activating only one source per resolution cell at a time. We propose here to use spectral contrast between different objects to separate their signals [8, 10]. The presented method extracts sub-resolution spatial information from the difference in signal phase of PA data sets acquired at different optical wavelengths, without using heuristic classification criteria [11], to achieve source localization to a scale of a fraction of the diffraction-limited acoustic resolution.

In limited-view PAT imaging, the received signals are a superposition of the waves emitted by all PA sources. In the process of image reconstruction, these signals are backpropagated towards the source locations, but the accuracy of this procedure is fundamentally limited by acoustic wave diffraction in the detection setup (determined by aperture size, element size, and bandwidth). As a result, structures cannot be resolved below the typical size of the point-spread function (PSF) of the

imaging system. Ideally, we want to separate all PA sources of any size and at any mutual distance. A family of image processing techniques, based on centroid fitting of the impulse response in an image, achieves this by capturing the signal from one source at a time [7-10, 12]. A common approach , in limited-view PAT, to selectively acquire and discriminate the signals from different classes of photoacoustic absorbers is making use of spectral contrast. In vasculature imaging for example, the variation in optical absorption with blood oxygenation enables selective targeting of arteries in one acquisition and veins in another, by tuning the excitation source to different wavelengths. Each data set then represents an image of the distribution of the targeted PA source. Overlapping objects in the frames indicate the presence of a small artery and a small vein, within one resolution cell. Reporter gene expression, contrast delivery in microvascular networks, and cleavable molecular beacons are other applications where spectral contrast is available and deep, high-resolution in vivo imaging is an asset [2, 13]. We show here that the phase difference between PA acquisitions can detect multiple sources in a resolution cell, and measure the distance between those sources. In principle, as many wavelengths are needed as there are different source types; here, we present the algorithm and demonstrate its functionality with two different sources per cluster.

The principle stems from the following features of PAI. Neighboring sources with optical contrast, as opposed to aggregates of PA sources of similar absorption spectra, emit, in theory, separable PA signals [14, 15]. The signal of a point-like source as recorded by a linear transducer array is described by a hyperbola (Figure 7.1a,b). If both sources are geometrically identical or smaller than the imaging system's PSF, then their individual recorded photoacoustic signals are similar but shifted laterally (to adjacent elements), axially (in time), or according to a superposition of these, depending on the two objects' relative positions [16]. The phase difference between the signals across the array provides detailed and accurate information on the relative positioning of the sources, with distinct signatures of lateral and axial separation (Figure 7.1c). Thus, if we could image one PA object type per frame, then the phase difference across the transducer's elements between those frames provides an accurate

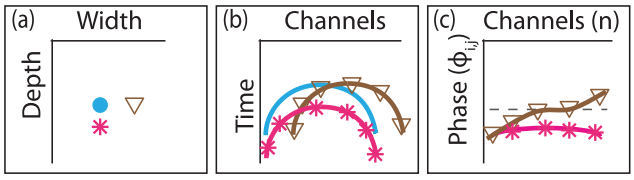

Figure 7.1 Concept of the differential phase photoacoustic algorithm. (a) Neighboring PA sources and (b) their respective signals received by an array of transducers. (c) Phase difference ϕ between laterally (triangle) and axially shifted sources (star) relative to zero (dashed line).

estimate of the localization of different clusters of PA sources. Path length differences can be estimated by cross-correlation, but this requires upsampling and region selection, without finally delivering per-pixel estimates.

Phase differences between ultrasound frames acquired at high frame rate were previously utilized to detect submicron displacement of artery walls [16]. The differential phase photoacoustic (DPPA) algorithm uses an analogous approach to improve the accuracy of localization of PA sources imaged with a limited-view PAT setup, by using the phase difference between frames acquired at different wavelengths. The algorithm assumes point-like sources, and wavelengths are chosen to produce contrasting and known PA responses.

It applies the following steps: first, two different wavelengths λ_1 and λ_2 are tuned to acquire two frames targeting two different chromophores A and B. Second, the channel data is converted to analytical signals (i.e., in In-phase Quadrature, IQ, format) through the Hilbert transform. Third, low signal regions are masked out to remove noise and spurious signals. Fourth, the phase difference ϕ_n between the two frames is calculated for all elements and is converted to a path length difference using $\theta_n = \phi_n \cdot \frac{c}{2\pi f_c}$, where c is the speed of sound and f_c the center frequency of the transducer.

Choosing the sampling frequency (f_s) above the Nyquist rate ensures that the minimal detectable ϕ_n becomes independent of f_s. Assuming source A is located at the pixel center (x_i, z_j), we refer to the quantity $\theta_{(i,j),n}$ as the additional path delay from source B to transducer element n located at $(x_n, 0)$. Here, x is the coordinate along the transducer array, and z is the depth coordinate. In conventional image beamforming, the travel paths used in the delay-and-sum algorithm to reconstruct pixel (i,j) are:

$$S_{(i,j),n} = \sqrt{z_f^2 + (x_n - x_i)^2} \tag{1}$$

For the second frame, we compute a second set of travel paths $D_{(i,j),n} = S_{(i,j),n} + \theta_{(i,j),n}$ using the information contained in the path delay. As a rule, the analyzed pixels display a high signal at both imaging wavelengths, indicating the presence of both sources at the selected location (x_i, z_j). Setting the position estimate of source A at λ_1 $(\hat{x}_a, \hat{z}_a) = (x_i, z_j)$, the second set of travel paths yields multiple possible locations (a set of equidistant points to transducer n at distance $D_{(i,j),n}$) for source B at λ_2. To reduce the set of possible locations, we solve for the intersections $I_{(i,j),k}$, $(k \in [1\ \frac{1}{2}n\ (n-1)])$, of the circles centered at pairs of transducers $\{n_a\ ,\ n_b\}$, with radii $D_{(i,j),n_a}$ and $D_{(i,j),n_b}$. Taking the median of the set of intersections $I_{(i,j),k}$ obtained from all possible pairs of transducer elements provides an estimate of the position $(\hat{x}_b, \hat{z}_b)$ of the unresolved source B, relative to the source A at (x_i, z_j). However, generally, at the chosen illumination wavelengths, both targeted sources emit PA waves. If these sources cannot be resolved, the resulting signal as detected by a transducer is a superposition of both. With the following steps, we can further disentangle the PA sources. Signals appear

to be originating from one PA source located at the center of mass of those two sources, weighted by their PA response, μ_A and μ_B, depending on the absorption coefficient and potentially other parameters, which are assumed to be known [11]. The center of mass O_{λ_1} at wavelength λ_1 located at $(\hat{x}_a, \hat{z}_a)$ or O_{λ_2} at wavelength λ_2 located at $(\hat{x}_b, \hat{z}_b)$ is related to the location of the targeted PA sources A (x_A, z_A) responding at λ_1 and B (x_B, z_B) responding at λ_2 as described by the following vector relation:

$$\overline{AO_\lambda} = \frac{\mu_{B,\lambda}}{\mu_{B,\lambda} + \mu_{A,\lambda}} \overline{AB} \tag{2}$$

The true positions for sources A $(x_A, z_A)$and B (x_B, z_B) are obtained by solving Eq.2 for both frames at λ_1 and λ_2.

Three experiments were performed to test the algorithm. Because lateral resolution is worse than axial resolution in limited-view PAT systems, and because $\phi_{(i,j),n}$ is more challenging to analyze for laterally separated sources, we set up the first experiment to evaluate the DPPA algorithm on a pair of laterally separated wires. We imaged two parallel wires, with a diameter of 40 μm, colored red and blue. The blue wire is movable to adjust the separation distance. Light at 440 nm, 680 nm and 540 nm was delivered to the phantom by a fiber connected to a tunable laser (Vibrant B-355II, Opotek, Santa Clara, CA, USA); at 440 nm the red wire PA signal is dominant, at 680 nm the blue wire PA signal is dominant and at 540 nm both wires emit equally (Figure 7.2a). A phased array transducer (ATL P4-1, 1-4 MHz bandwidth, 295μm pitch) connected to an ultrasound research system (Vantage 256, Verasonics, Redmond, Washington, USA) collected the PA signal from the two wires at the three mentioned illumination wavelengths. The lateral resolution in the reconstructed images was 0.8 mm (-3 dB lateral width, at ~2 cm depth). Simultaneously, a needle hydrophone (20MHz, Precision Acoustics, Dorset, UK), perpendicular to the wires, also collected the PA signals. Cross-correlation of the hydrophone traces at 680 nm and 440 nm provided an accurate estimate of the distance between the two wires. Comparisons with peak-to-peak distance measurements on the traces obtained at 540 nm for distances greater than 100 μm yield a maximum position error of ± 3 μm.

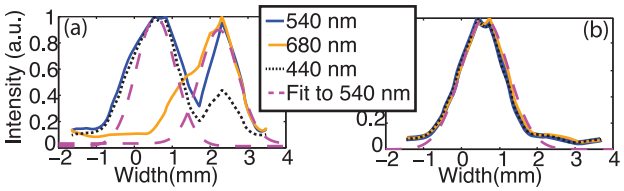

Figure 7.2 Lateral cut through the beamformed envelope of two wires at different distances (a) 1.4 mm and (b) 71 μm separation distance at three imaging wavelengths and the Gaussian fit to the 540 nm profile.

We analyzed the data from red and blue parallel wires using two different pairs of wavelengths. When using the combination of 680 nm and 440 nm, it is as though we are imaging each of the wires individually (since at both those wavelengths one wire is clearly dominant). When using the combination of 540 nm and 680 nm, we are actually analyzing a frame where both wires emit equally and a frame where one wire is dominant, as shown by Figure 7.2a. In Figure 7.2b we see that at small separation distances, the PA signal does not reveal the presence of two wires, but rather suggests the presence of only one PA source at either of the illumination wavelengths. In these cases, spectral unmixing algorithms cannot disentangle the two sources. Applying the DPPA algorithm we recover a range of separation distances spanning from 40 μm (wires touching) to a maximum separation distance of 1.6 mm (equal to the illumination spot size). For distances greater than 0.8 mm, the wires are clearly separable, and the DPPA algorithm is not needed. Nevertheless, we evaluated the precision of the proposed algorithm in those cases as well for generality. In order to estimate separation distances that are larger than the image resolution, meaning $\theta_{(i,j),n} > \frac{c}{f_c}$, the phase $\phi_{(i,j),n}$ is unwrapped prior to the analysis. In Figure 7.3, we plotted the estimated separation distance against the distance extracted from the hydrophone measurement (which we take as a ground truth). We fitted the data to a linear regression model ($y=ax+b$), resulting in [$a = 0.98 \pm 0.06$, $b = (1 \pm 5)\cdot10^{-5}$, $R^2 = 0.97$] from the frames at 540/680 nm, and [$a = 0.99 \pm 0.05$, $b = (1 \pm 5)\cdot10^{-5}$, $R^2 = 0.98$] from the 440/680 nm combination. The difference with the ground truth was not significant in either case. We also found that in both analyses we are able to recover the separation distance with a mean percentage error of 2.3% and a standard deviation of 6%. Figure 7.3 also shows distances recovered using Gaussian fits (red/blue crosses) to the lateral profile at the centerline of the beamformed image (dashed

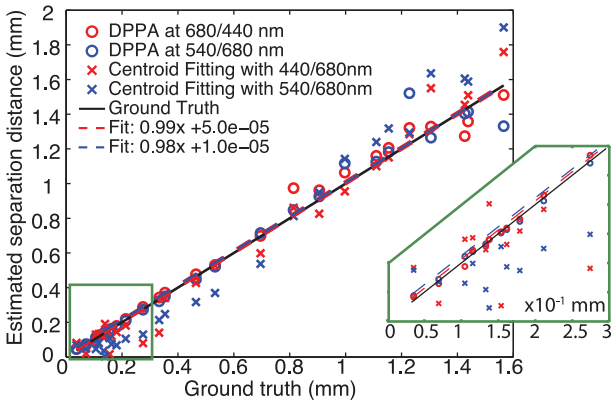

Figure 7.3 Separation distance estimates using two different pairs of wavelengths for both centroid fitting and DPPA. The fits to the DPPA are approximately equal to the unity line.

lines in Figure 7.2a,b). The separation distance from the centroid fits is defined as the position difference of the maxima of the fitted curves at both wavelengths, using the 440/680 and 540/680 nm combinations. We observe that DPPA is superior to Gaussian fitting, especially at estimating small distances. We note that the algorithm is robust for a range of object separations and contrast ratios.

In a second experiment, we assessed the capacity of the DPPA to isolate multiple targets using a phantom consisting of three pairs of 40 μm red and blue wires, axially and laterally offset as shown on Figure 7.4a. The intrapair distances were 160 μm, 283 μm and 539 μm by mechanical design; the actual distances may be slightly different in water. The beamformed images indicate the presence of a single PA source at each cluster (Figure 7.4b). We selected clusters containing mixed signals, i.e. image regions with a beamformed signal greater than a preset threshold at both illumination wavelengths, and isolated the RF signals. Application of the DPPA algorithm indicates the presence of more than one absorber. Figure 7.4c shows both the ground truth and the reconstructed dots. The blue circles in Figure 7.4c are the local maxima, representing the position of the PA sources at λ_1, and the red circles are the reconstructed positions of the second PA source. Crosses in Figure 7.4c indicate the true object positions. The estimated separation distances and angles were recovered with 5% accuracy.

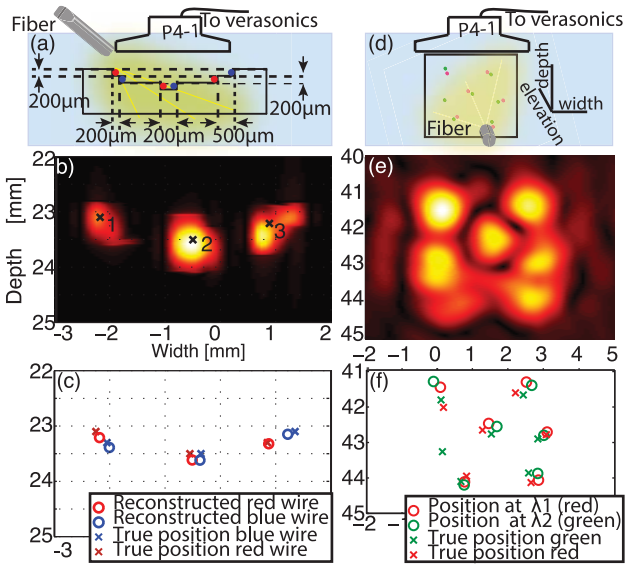

Figure 7.4 True vs. reconstructed position of multiple complex sources. (a) Experimental setup for three wire pairs. (b) Beamformed image and selected maxima. (c) Separation of the unresolved sources. (d) Experimental setup for dot pattern. (e) Combined 500 nm and 680 nm images. (f) Reconstructed dots using DPPA vs. measured position.

Finally, we created a more complex object, mimicking a cross sectional view of microvascular structures, consisting of six pairs of ~260 μm diameter green and red dots along with a single green dot, printed on transparent film. The excitation wavelengths were 500 nm (red absorbing), and 680 nm (green absorbing). The film was placed in the acoustic imaging plane, parallel to the beam, and illuminated from the side (Figure 7.4d). This experiment is more challenging because the complex sources were located farther from the transducer, leading to poorer PSF. Figure 7.4f shows the ground truth as printed on the transparent film as well as the dots reconstructed with DPPA, showing adequate identification of multiple sources in the resolution cell and a relatively accurate estimate of their positions. The DPPA algorithm also successfully identifies the unpaired green dot as not containing a complex source. We observe a larger separation error, and an overall image distortion because the beamforming does not account for heterogeneity in the speed of sound in the film/water medium. Regardless, the DPPA algorithm enables us to create a reconstruction of the phantom, which reflects the clustered sources that remain hidden in the beamformed image in Figure 7.4e.

It must be noted that the lower boundary in the distance measurements we present here was the result of experimental limitations. So far, we assume that each cluster contains no more than two sources. If more sources with optical contrast are expected within a cluster, the relative positions may be resolved by using as many wavelengths as there are expected source types, a common strategy in optical microscopy [17]. Use of more than two wavelengths can help to account for predictable absorption coefficient changes, such as varying oxygen saturation in microvessels. We have not studied the effect of extended sources, where object shape affects the wavefront. We anticipate that a solution, employing a library of signal characteristics related to a range of source configurations, combined with the distance measurement based on median phase difference estimates, will be able to handle structured objects. Moreover, the accuracy of the obtained results is representative of a highly controlled environment with limited acoustic heterogeneity and optimal imaging geometry. We assumed that the excitation fluence is constant throughout the phantom at the two wavelengths; variations in fluence are small for nearby sources. We do observe in the first experiment that the error increases at larger separation, which we attribute to fluence variation in the beam across the 1.6 mm distance in the optically clear medium. Scattering by tissue will homogenize the light distribution and hence increases the accuracy of our method, competing with an SNR decrease due to loss of light at the target. Potential variations in fluence due to spectral coloring in more complex scenarii could be tackled using estimation methods, such as described in [18, 19]. Also, in vivo applications will benefit from motion correction based on ultrasound-measured tissue displacement [16]. The slow pulse rates of commonly used tunable lasers make it easy to interleave ultrafast ultrasound and PA imaging. Extension to 3D imaging with matrix probes is straightforward; even sparse arrays will

provide sufficient phase difference measurements to extract high-accuracy position estimates.

To conclude, differential phase imaging successfully determines the sub-resolution distance between sources of a-priori known optical absorption contrast. The algorithm can detect structure in a target that appears as a single object in a PA image, discriminating clustered sources from simple ones. We measured the distance between spectrally contrasting point absorbers with a standard deviation of 6% for pairs of targets that were separated by 1/20th of the PSF width. We quantitatively demonstrated the accuracy of reconstruction on a single pair of wires, and on multiple targets with both lateral and axial offsets. Potential applications are imaging of micro-vasculature, and superlocalization of contrast agents deep inside tissue.

References

[1] L. H. V. Wang and S. Hu, "**Photoacoustic tomography: In vivo imaging from organelles to organs,**" *Science,* vol. **335**, pp. 1458-1462, Mar 2012.

[2] X. Cai, L. Li, A. Krumholz, Z. Guo, T. N. Erpelding, C. Zhang, Y. Zhang, Y. Xia, and L. V. Wang, "**Multi-scale molecular photoacoustic tomography of gene expression,**" *PloS one,* vol. **7**, p. e43999, 2012.

[3] E. Z. Zhang, J. G. Laufer, R. B. Pedley, and P. C. Beard, "**In vivo high-resolution 3d photoacoustic imaging of superficial vascular anatomy,**" *Physics in medicine and biology,* vol. **54**, p. 1035, 2009.

[4] S. Vaithilingam, T.-J. Ma, Y. Furukawa, I. O. Wygant, Z. Xuefeng, A. De La Zerda, O. Oralkan, A. Kamaya, R. B. Jeffrey, and B. T. Khuri-Yakub, "**Three-dimensional photoacoustic imaging using a two-dimensional cmut array,**" *Ultrasonics, Ferroelectrics, and Frequency Control, IEEE Transactions on,* vol. **56**, pp. 2411-2419, 2009.

[5] T. Chaigne, J. Gateau, M. Allain, O. Katz, S. Gigan, A. Sentenac, and E. Bossy, "**Super-resolution photoacoustic fluctuation imaging with multiple speckle illumination,**" *Optica,* vol. **3**, pp. 54-57, 2016.

[6] D. B. Conkey, A. M. Caravaca-Aguirre, J. D. Dove, H. Ju, T. W. Murray, and R. Piestun, "**Super-resolution photoacoustic imaging through a scattering wall,**" *Nature Communications,* vol. **6**, 2015.

[7] E. Betzig, G. H. Patterson, R. Sougrat, O. W. Lindwasser, S. Olenych, J. S. Bonifacino, M. W. Davidson, J. Lippincott-Schwartz, and H. F. Hess, "**Imaging intracellular fluorescent proteins at nanometer resolution,**" *Science,* vol. **313**, pp. 1642-1645, 2006.

[8] L. S. Churchman, Z. Ökten, R. S. Rock, J. F. Dawson, and J. A. Spudich, "**Single molecule high-resolution colocalization of cy3 and cy5 attached to macromolecules measures intramolecular distances through time,**" *Proceedings of the National Academy of Sciences of the United States of America,* vol. **102**, pp. 1419-1423, February 1, 2005 2005.

[9] C. Errico, J. Pierre, S. Pezet, Y. Desailly, Z. Lenkei, O. Couture, and M. Tanter, "**Ultrafast ultrasound localization microscopy for deep super-resolution vascular imaging,**" *Nature,* vol. **527**, pp. 499-502, 2015.

[10] A. M. van Oijen, J. Köhler, J. Schmidt, M. Müller, and G. J. Brakenhoff, "**Far-field fluorescence microscopy beyond the diffraction limit,**" *Journal of the Optical Society of America A,* vol. **16**, pp. 909-915, 1999/04/01 1999.

[11] H. Ammari, E. Bossy, V. Jugnon, and H. Kang, "**Mathematical modeling in photoacoustic imaging of small absorbers,**" *SIAM review,* vol. **52**, pp. 677-695, 2010.

[12] M. J. Rust, M. Bates, and X. Zhuang, "**Sub-diffraction-limit imaging by stochastic optical reconstruction microscopy (storm),**" *Nature methods,* vol. **3**, pp. 793-796, 2006.

[13] K. Yang, L. Zhu, L. Nie, X. Sun, L. Cheng, C. Wu, G. Niu, X. Chen, and Z. Liu, "**Visualization of protease activity in vivo using an activatable photo-acoustic imaging probe based on cus nanoparticles,**" *Theranostics,* vol. **4**, pp. 134-41, 2014.

[14] R. K. Saha and M. C. Kolios, "**A simulation study on photoacoustic signals from red blood cells,**" *The Journal of the Acoustical Society of America,* vol. **129**, pp. 2935-2943, 2011.

[15] Z. J. Guo, L. Li, and L. H. V. Wang, "**On the speckle-free nature of photoacoustic tomography,**" *Medical Physics,* vol. **36**, pp. 4084-4088, Sep 2009.

[16] P. Kruizinga, F. Mastik, J. G. Bosch, N. de Jong, A. F. van der Steen, and G. van Soest, "**Measuring submicrometer displacement vectors using high-frame-rate ultrasound imaging,**" *IEEE Trans Ultrason Ferroelectr Freq Control,* vol. **62**, pp. 1733-44, Oct 2015.

[17] P. Zhang, S. Lee, H. Yu, N. Fang, and S. H. Kang, "**Super-resolution of fluorescence-free plasmonic nanoparticles using enhanced dark-field illumination based on wavelength-modulation,**" *Scientific reports,* vol. **5**, 2015.

[18] A. Q. Bauer, R. E. Nothdurft, T. N. Erpelding, L. V. Wang, and J. P. Culver, "**Quantitative photoacoustic imaging: Correcting for heterogeneous light fluence distributions using diffuse optical tomography,**" *Journal of biomedical optics,* vol. **16**, pp. 096016-096016-7, 2011.

[19] B. T. Cox, S. R. Arridge, K. P. Kostli, and P. C. Beard, "**Quantitative photoacoustic imaging: Fitting a model of light transport to the initial pressure distribution**," in *Biomedical Optics 2005*, 2005, pp. 49-55.

Chapter 8

Discussion and Conclusion

8.1 PA imaging: hearing colors

Both light and sound are waves. Their interaction with matter, and their absorption by matter in particular, differs fundamentally, though. Ultrasound absorption has a smooth dependence on frequency, while optical radiation is absorbed by excitation of electronic or vibrational transitions, which tend to have a finely structured frequency spectrum. One of the interesting implications of that difference is that optical excitation of acoustic signals in photoacoustics enables us to acoustically probe optical absorption contrast: we can hear colors.

Biomedical photoacoustic imaging is a modality which fundamentally maps tissue absorption. However, on single wavelength photoacoustic images, which does not capitalize on this aspect of color audio, it is often challenging to correctly interpret an image, with no a-priori knowledge. Single wavelength photoacoustic signal variations across an image are the result of a mix of multiple factors. Indeed, for one, efficiency of the photoacoustic effect relies on the thermoelastic properties of the tissue, which usually also vary with ambient temperature. Thus, signal variations in one image could reflect temperature variations. Second, signal intensity distribution, in a single wavelength image, could also map the illumination/heat function (fluence distribution) within one object, which reflects tissue scattering and absorption properties. Finally, of importance to the majority of photoacoustic studies, the signal distribution reveals the location and/or concentration of different chromophores. Thus, in photoacoustic imaging, just like in any other imaging modality, we must carefully ask ourselves: what are we looking at? In a laboratory environment, careful manipulations may shed light on the nature of the signal observed: varying the illumination geometry, use of external sensors (e.g. thermometers), additional imaging modalities (e.g. ultrasound imaging) and tissue manipulation can isolate the source of the signal. In an in-vivo situation, the freedom in manipulating the object is more limited. The need for multimodal or multispectral imaging emerges, to identify features with certainty and understand the origin of the PA signal. These techniques are always built on thorough ex-vivo validations.

Multiple studies demonstrated how combination of information from multiple images can improve photoacoustic image quality. For instance, Kruizinga et al., showed that using information from ultrasound images can improve photoacoustic image interpretation [1]. More popularly, multi spectral optoacoustic tomography (MSOT), a wide subfield of photoacoustic imaging, capitalizes on signal feature variation with imaging wavelength to isolate targeted compounds from background [2, 3], using a family of analysis techniques that are collectively called spectral unmixing. MSOT can also be used as a means to correct for signal variations due to the fluence distribution in tissue and isolate those due to chromophores absorption [4]. One unifying research target among all MSOT studies is determining the smallest number of wavelengths needed to extract the desired features. This minimum varies with application,

depending on the number of chromophores to be identified, their spectral (dis) similarity, the spectral structure of the background, and the signal-to-noise ratio of the image. In this thesis we explored dual-wavelength photoacoustic methods, built on knowledge extracted from spectroscopic studies, as a means to improve visualization of cardiac features for two specific cardiovascular applications, and as a means to localize PA sources. In the following paragraphs we discuss the capability to translate laboratory experiments to the 'real' situation. We question the ability to reliably extract the same information under different circumstances, evaluating the methods we developed and the scientific reasoning we have followed to answer the question: what are we looking at?

8.2 RF ablation lesion monitoring

In chapters 2, 3 and 4 we have spectroscopically studied the features of RF ablation lesion and developed a robust imaging solution which can be translated in vivo. Based on the ratio of PA images obtained at two wavelengths 790 nm and 930 nm we were capable of robustly imaging RF ablation lesions with a diagnostic accuracy of 0.97.

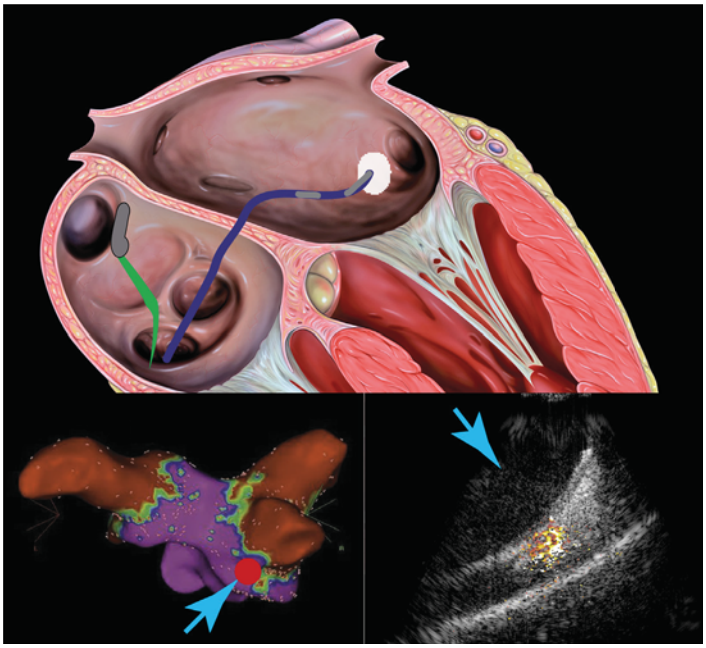

Figure 8.1 Envisioned use of the proposed technology. ICE catheter in green; PA-enabled RF ablation catheter in blue. Blue arrows point at the lesion site.

The performance of any single wavelength (410 nm to 1000 nm) imaging technique is inferior. The spectroscopic analysis showed that the lesion identification accuracy was possible regardless of the initial oxygenation state of the tissue. We have demonstrated that this solution can be applied within the context of a beating heart with circulating blood. A PA-enabled ablation catheter was used as the illumination source, demonstrating a good SNR and realizing sufficient lateral imaging extent for 2D lesion sizing, as well as for detection of gaps between lesions.

The currently envisioned solution to RF ablation treatment monitoring for atrial fibrillation is illustrated in Figure 8.1 where our imaging method based on a PA-enabled catheter and ICE probe is integrated with electro-anatomical mapping systems. Two-wavelength PA imaging is the first imaging modality that has demonstrated visualization of lesions as they are created during an ablation procedure. With continued development, this initial result may impact the electrophysiology field by providing the operating physician with real-time feedback on the treatment effect that is delivered by the ablation, showing the location and extent of lesions relative to the atrial wall and relative to each other.

8.2.1 Applicability of the results in this thesis

PA considerations for transmural imaging

Two-wavelength ratio-based imaging improves both lesion delineation and detection. For this dual-wavelength imaging method to work in identifying lesions at depth, it is important for the light at the chosen wavelengths to undergo similar levels of attenuation with depth through the imaged slab of tissue. Variable attenuation with wavelength introduces a spectral variation of optical fluence, an effect that is called spectral coloring. In Figure 8.2, illuminating ablated tissue through the endocardium exhibits spectral coloring, visible as a change in the spectral response with depth in the image for both lesion and untreated tissue parts in the visible range. However, in the near-infrared the spectral features of both regions remained unchanged. We verified that the differences in spectra resulted from spectral coloring, and not from the presence of different chromophores, by cutting through the tissue at the imaging plane and illuminating the whole plane homogeneously (Figure 8.2c,d). We observed then that the lesion and non-ablated tissue spectra are similar throughout the depth, meaning that the PA sources are identical across the depth. The examined depth was of $\sim$3mm. This observation confirms the use of the proposed dual wavelength method to map lesion signals at depth and assess lesion transmurality in tissue slabs of 3 mm or less. It ensures homogenous (equal) ratio signal values across depth for lesion tissue, which we have observed in our images.

In addition to that, the optical fluence distribution affects the received PA signal and the interpretation of the resulting image. For instance, the absence of PA signal may either reflect the absence of absorbing chromophores, or insufficient local fluence to generate detectable signal. In the spectroscopic study we have conducted,

we differentiated between these two states by placing a strong absorber as a reference on the far side (relative to the light source) of the imaged tissue slab. When the reference absorber emitted a PA signal, we were certain that sufficient light went through the imaged tissue slab and created a homogenous fluence throughout. Manipulation of the absorber position along with the use of a point source illumination can be used to assess the optical parameters, such as transmission, reflection, absorption and scattering, of the tissue slab as a whole. These can be used to model tissue optics and correct the PA images for illumination heterogeneity, and may shed light on the origins of the imaging contrast changes, which may result from tissue scattering differences or from variations in chromophore concentration and types.

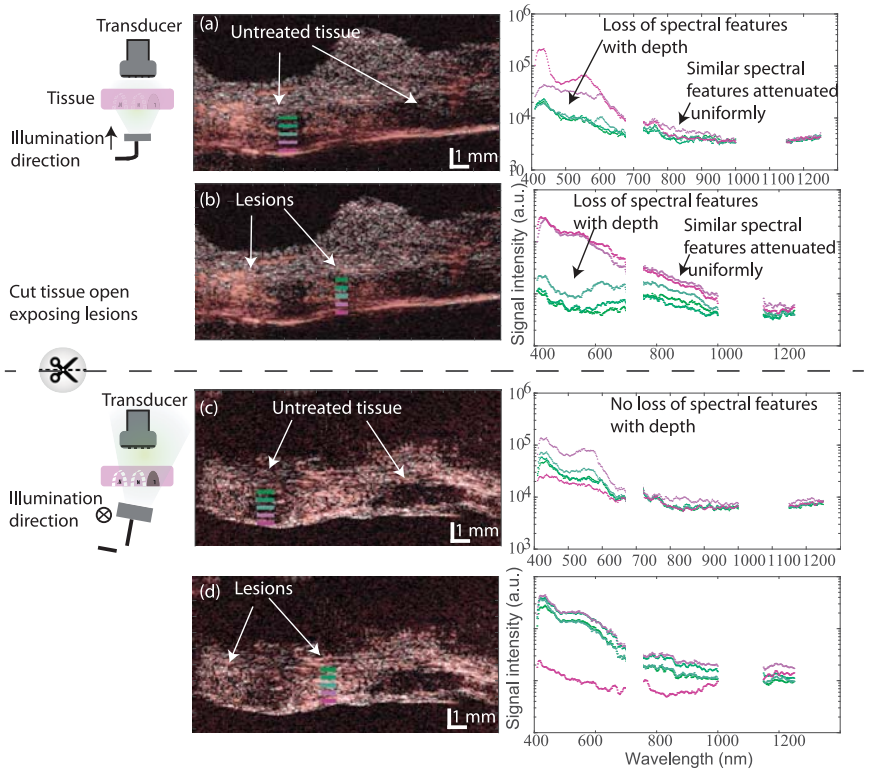

Figure 8.2 Transmission mode photoacoustic setup of fresh ablated porcine tissue. (a) Evaluation of PA spectra of untreated tissue areas and (b) ablated tissue areas as the tissue is illuminated from the endocardium (transmission mode PA setup). (c) Evaluation of PA spectra of untreated tissue areas and (d) ablated tissue areas as the tissue is cut and illuminated en face (orthogonal mode PA setup). Right column: PA spectra extracted from different depths at the regions indicated by colored rectangles in the photoacoustic (red scale) ultrasound (gray scale) image overlay.

In this thesis we chose our wavelengths to ensure full tissue depth illumination. We have shown in Chapter 2 that the dual wavelength methods proposed showed better transmurality assessment for RF ablation lesions than any other single wavelength method in the range of (410 to 1000 nm). It has the advantage of homogenizing the signal across depth and removing clutter artefacts due to the catheter tip. Under broad illumination we have observed that fluences between 0.3 and 1 mJ/cm^2 were sufficient to penetrate through a tissue slab of up to 8 mm. However, a systematic study on the extent and transmurality of a large number of lesions in different tissue thicknesses is still needed, especially under catheter based illumination. In addition to that, for better imaging precision, a resolution study for the minimum gap size detection is also needed.

Comparison between human and porcine tissue

All the results we have presented in this thesis regarding ablation lesion monitoring were predominantly demonstrated on porcine tissue. We foresee our results to generalize to human atrium tissue. In order to be a tad more confident, we compared PA spectroscopy signals from fresh and ablated human left atrium appendage to those we have obtained from porcine specimen in Chapter 2 (Figure 8.3). The ablated tissue PA signal is the same across wavelengths, suggesting that the method is potentially directly applicable on human tissue. Comparison between fresh human tissue and material that was kept in frozen storage does show large changes to the spectrum. For this reason we always worked with fresh specimens.

8.2.2 Future research topics

Lesion types

In general, PA spectroscopy is a good stepping stone to any PA study focusing on the capability of PA to identify tissue molecular composition. Not only does it allow optimizing for the best imaging wavelength, but it also allows understanding and identifying other potential sources of signal. Thus, similarly to Dana et al. [5] and Pang et al. [6], we investigated spectroscopically optimal settings for RF ablation lesion contrast. Unlike the other two groups, the illumination range we investigated extended to the visible range, covering wavelengths from 410 nm to 1000 nm. The visible range is obviously impractical for imaging since, optical penetration depth is limited in tissue in that range. However, looking at the full spectrum helped us identify some of the chromophores in play, and the effect of their concentration variations, in healthy and ablated myocardium tissue.

For instance, we identified different tissue oxygenation levels in the studied ex-vivo porcine specimens, and also the likely presence of hemichromes in the lesions formed (Chapter 2). Despite initial varying oxygenation levels in tissue, we could consistently identify ablation lesions with high accuracy. This leads us to think that the imaging method we have proposed is robust for different tissue oxygenation levels. In addition to that, in the study we have conducted, it was straightforward to

identify myoglobin variants and lipids or collagen from their optical spectra, for they are very well documented in the literature. Ablation lesion components on the other hand were less researched. The optical properties of denatured proteins, necrosis coagulum, hemichromes, metmyoglobin, etc., are not fully documented in the literature. We foresee that the full spectra we have acquired are only the beginning for further studies of the different tissue components and tissue ablation stages related to different ablation settings. In fact, one future step in ablation lesion characterization is to look at the differences in spectral characteristics between the different types of lesions. An identification method for different lesion stages and components could potentially be useful in the comparison between EP catheters and other ablative

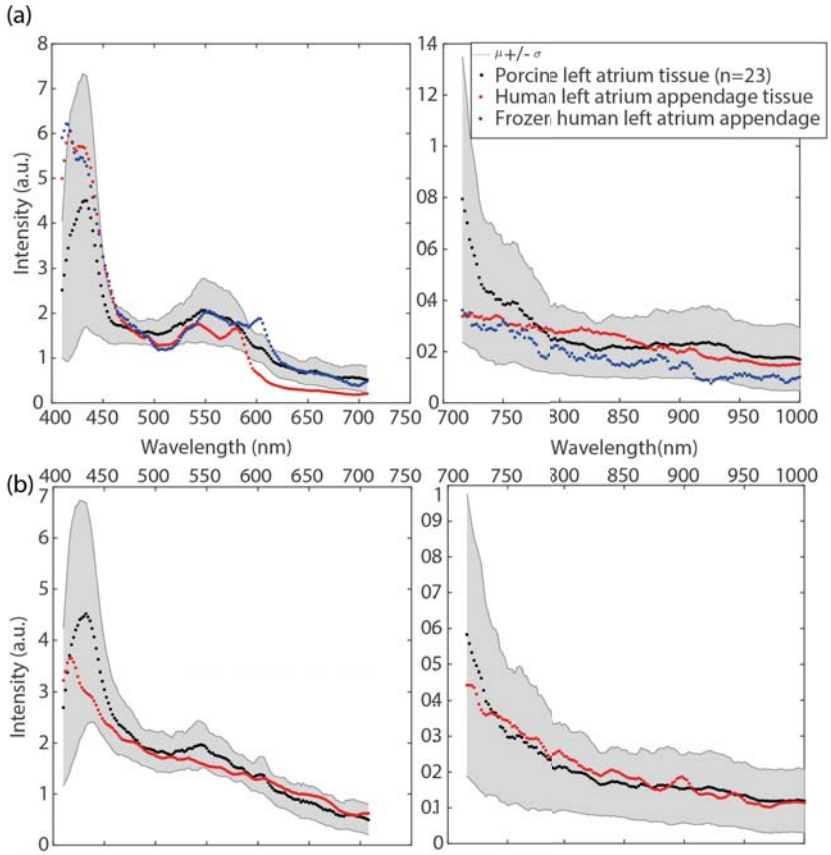

Figure 8.3. Porcine vs Human PA spectroscopy of (a) untreated atrial tissue and (b) ablated (lesion) atrial tissue. The visible and near infrared ranges were split for better visualization, due to the high difference in signal intensity. The fresh human sample (n=1) was more oxygenated than the averaged porcine samples included in this study. Initial oxygenation state does not affect the ablated spectrum.

devices. PA imaging would provide a window on the different lesion stages along the temperature gradient, as well as the differences between the lesions formed through alternative energy applications such as laser light or cryotherapy.

An additional advantage to performing a wide range photoacoustic spectroscopy is developing understanding with respect to the observed signal. Atrial myocardium is a three-tissue layer structure, and the coupling between the layers may have a role in the appearance of conduction disorders. These tissue layers look optically different to the eye. They thus should have different photoacoustic signatures. However, we found it difficult to isolate single spectra from different tissue components with the setup we have developed. Band-limited detection in PA imaging tends to emphasize differential contrast across boundaries, rather than bulk absorption [7]. Therefore, in PA spectroscopy of layered tissue, it is important to understand that we are not directly mapping the absolute absorption of the components within that layer, but rather the difference in absorption at the interface between two layers (cf. Figure 8.2d signal from the endocardium (pink) in orthogonal mode PA setup). For the purposes of our study, obtaining full characterization of the tissue in two states, ablated and fresh, was the goal. For fundamental research, this is an important point to consider.

Another important observation achieved by means of spectroscopy is the effect of freezing tissue on the experimental protocol. Very early on, we have noticed that freezing tissue for conserving human left atrial appendages changes the PA spectrum observed. We noticed a bigger effect of metmyoglobin on the frozen tissue than in its other forms (Figure 8.3 blue curve, peak at 600 nm). This may have an impact on translation of the imaging results achieved on RF ablation to the other forms of ablation, namely laser and cryo ablation. This topic thus needs to be investigated further.

Frequency domain-analysis

We did not explore and use the differences in PA signal frequency spectra between ablated and untreated myocardium tissue (Figure 8.4). This is a point which can further be exploited when integrating with a dedicated US solution.

Figure 8.4, shows spectra differences when measuring signals in transmission mode with two different transducer bandwidths. One is a linear array transducer (192 channels, L12-3v, f_c = 7.8 MHz, Verasonics, Kirkland, Washington) and the other is a hydrophone (20 MHz bandwidth, Precision Acoustics). We definitely observe an increase in the energy of higher frequencies for ablated tissue in comparison to untreated tissue when using the hydrophone. The limited bandwidth of the array transducer attenuates this contrast. We verified that these changes were not the result of other unknown parameters by checking that the PA signals from the water interface or the optical fiber metallic tip remained the same. This needs to be further examined.

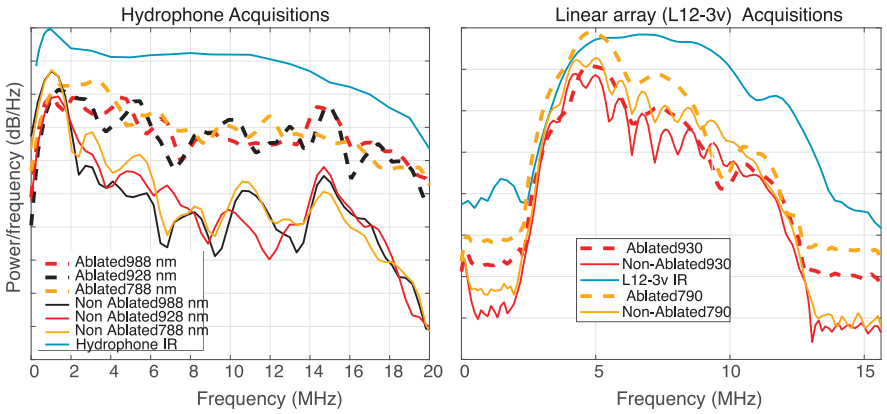

Figure 8.4 Frequency spectra of PA signals of ablated and untreated myocardium tissue at different wavelengths acquired by two different acoustic transducers.

Integration with echocardiography?

Other research groups also investigated ways of robustly imaging ablation lesions and proposed different methods using other imaging modalities. Ultrasound imaging studies [8, 9] showed promising results in monitoring RF ablation lesions. Ultrasound features such as crater formation, wall thickness increase, echogenicity changes [10-12], were correlated with different lesion characteristics such as edema or necrosis. However, these were inconsistent between the studies. Our PA spectroscopic measurements were always accompanied by ultrasound measurements, and our echo observations corroborate the inconsistency observed in the literature (Figure 8.5). Contrast is variable across specimens, across lesions, and appears to be unstable, with a clear impact on identification and delineation of lesions. Initial echogenicity will vary with respective imaging plane and myofibers orientation [13]. Hyperechoic regions may look (according to some studies in the literature [14]) as lesions even though they are not (Figure 8.5, Lesion 3 pre-ablation). Perhaps more information may be extracted through advanced analysis, but in its raw B-mode imaging state, lesion identification by echo is challenging.

Ultrasound elastography methods were also shown to be promising [15, 16]. Lesions do exhibit higher stiffness than the surrounding tissue. However, in-vivo US elastography imaging across the ablation catheter in an erratically beating heart remains quite complex and difficult. This solution is thus not very well suited for monitoring of lesion progression, and may require long manipulation time. We have observed slight variations in the SNR of the PA signals collected during RF ablation through the (applied) cardiac cycle (Chapter 4). We have observed the same phenomenon in intravascular PA imaging (Chapter 6). There seems to be a relationship between signal strength and tissue stretch, and potentially tissue softness. This variation

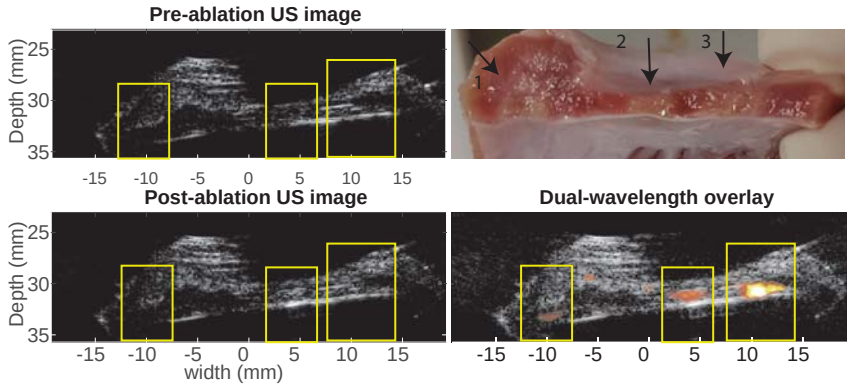

Figure 8.5. Contradictory appearance of lesions on ultrasound. Lesion 1 is probably hypoechoic and a bit out of the imaging plane. Lesion 2 changes echogenicity as reported in the literature. Lesion 3 is hyperechoic before and after ablation. Lesion gaps and transmurality cannot be derived from US alone.

in signal was dealt with in RF ablation PA signal processing by averaging throughout the heartbeat. This was possible because ablation is a slow process, for which feedback in the seconds range is affordable. However, we shall further exploit and research this feature in both RFPA and IVPA for assessing tissue mechanical properties. Since US is integral part of both solutions, US elastography methods could also be modified and integrated into a new algorithm using PA signal information.

Imaging system

In this initial work we focused on proving that the proposed dual wavelength imaging method is feasible in real-time acquisition and works as well in a heart beating mimicking setup as it does in a static one. Integration of information from the acquired single wavelength images to the current imaging technique could open to a wealth of information. For instance, in the imaging method proposed, the absence of lesion is represented as an absence of signal. Absence of signal could also occur if the imaging and ablation catheters are misaligned. Feedback from single wavelength images should thus be integrated to compensate for catheter position/orientation and its contact with tissue. In addition to that, if studied, single wavelengths images could provide a tissue temperature profile in depth, which is valuable information in EP procedures and EP research. There is thus further potential for a full PA based solution for EP integrating in depth temperature profile mapping, tissue elastography assessment and differentiation between different lesion types.

8.2.3 Potential impact on interventional electrophysiology

Low success rates of AF therapy by means of a pulmonary vein isolation have positioned this specific intervention at the center of various research studies. Two hypotheses were presented to explain this low procedural outcome.

On the one hand, it is argued that the understanding of the underlying electropathology is erroneous. Current ablation strategies assume that the heart rhythm is perturbed by high frequency electrical activity of ectopic foci disturbing the normal pattern of atrial conduction. Isolation of these ectopic foci discharging at fast rates prevents propagation to the rest of the myocardium, restoring normal cardiac rhythm. This ablation strategy is derived from the open-chest surgery, the 'Cox-Maze', where determined conductive areas are cut and sewn, generating non-conductive scar tissue to prevent electrical wave propagation from the isolated areas to the rest of the myocardium. Emerging research in the electrophysiology field has revealed that recurrences of AF after pulmonary vein isolation are due to the presence of an extensive arrhythmogenic substrate. This arrhythmogenic substrate may consist of rotational or endo-epicardial activity [17, 18]. Electrophysiologists shall thus rather identify areas of electropathology, and ablate at these sites, which are involved in persistence of AF, to free the patient from arrhythmia.

On the other hand, it is argued that insufficient treatment delivery is the leading cause for atrial fibrillation recurrence in patients who have undergone RF ablation procedures. Gaps in the lesion traces as well as superficial (non-transmural) lesions allow for propagation of electrical waves from the ectopic foci to the rest of the myocardium [19]. These gaps are very plausible to occur because during the procedure, cardiologists have no visual feedback on the lesions they are creating; instead they rely on indirect parameter readouts, tissue models and heuristics. Indeed, much literature is available on the different parameters influencing lesion types and sizes. Different power settings must be selected for different atrium areas; impedance readouts predict different lesion sizes or other complications such as thrombus formation. Only recently did catheter makers integrate contact force sensors, for this also affects the lesion size. There remains a glaring information gap on the formed lesion extent and depth. It is this need, this uncertainty in lesion outline that drove multiple research centers into investigating ways of imaging RF ablation lesions. This problem also drove multiple ablation catheter companies into developing alternative catheters, such as contact-force sensing catheters, and looking into alternative energy modalities for ablation, such as laser ablation.

The truth about AF can only be unraveled by testing the hypotheses. Capability of delivering continuous transmural lesions, with certainty, is a means to test to the 2nd hypothesis. Thus, the imaging system presented in this thesis capable of RF ablation lesion transmurality and continuity evaluation, may serve as a tool in the research to determine the reasons for the low success rates of catheter-based ablation. The results demonstrated in this thesis, when applied to the clinic may even

contribute to increasing the procedural success rates. We demonstrated a method which evaluates lesion extent, as well as monitors lesion formation in real-time. Monitoring capability has the potential of preventing procedural complications related to excess of RF energy delivery. Indeed, delivering excessive energy may lead to cardiac perforation, tamponade, phrenic nerve or esophageal injuries etc. all serious life-threatening complications.

8.3 Intravascular photoacoustic imaging

IVPA can potentially target several of the hypothesized plaque features of interest. IVPA was previously demonstrated to image lipids [20, 21], macrophages [22], intraplaque hemorrhage [23] and temperature [24]. The complementarity with intra-vascular ultrasound imaging adds the capability of evaluation of plaque morphology, calcification and stiffness [25]. Key components of an IVPA/US system are:

- Laser source (wavelength, pulse length and pulse repetition frequency)
- Transducer center frequency and bandwidth
- Rotary joint and slip ring
- Real-time processing algorithm/software
- Receive electronics
- Catheter (sheath, optical and acoustical beam overlap, flexibility, miniaturization)

All of these components need to be engineered to the specific demands of IVPA imaging. Choices about the catheter sheath material, the transducer bandwidth and the laser source depend on the imaging targets. Catheters sheaths are necessary to limit damage to the artery wall as a result of imaging. For the IVPA/IVUS system, the catheter needs to minimize both optical absorption at the imaging wavelength(s) and acoustic attenuation. The laser source PRF needs to be high enough to allow real-time imaging, and the pulse duration short enough for a good SNR. The wavelength(s) need(s) to be targeted toward discriminating plaque features of interest. The transducer center frequency needs to be high for IVUS high resolution images, but also needs to accommodate the large bandwidth of the PA signals generated by the targeted plaque features.

Our current IVPA system and catheter model is optimized for imaging plaque lipids. In chapters 5 and 6 we have demonstrated imaging of atherosclerotic coronary specimens ex-vivo and porcine coronary arteries in-vivo. Indeed the system is coupled to two tunable lasers in the wavelength range of 1720 nm (targeting lipid). The catheter sheath was also optimized for that wavelength range and the transducer bandwidth (40 MHz, 50% bandwidth) was optimized for IVUS plaque morphology imaging. By coupling the laser static fiber to the catheter's larger rotating fiber through

an 50 µm air-gap, optical output was increased, and requirements on expensive D_2O flushing were shown to be more lenient. Tubing artefacts were reduced by using a silver sputtered prism to deflect the light orthogonally to the catheter axis, which won't immediately reach the 10° acoustic beam axis.

Perivascular lipids were previously hypothesized to predict development of atherosclerosis. In Chapter 6, peri-adventitia lipids were successfully imaged and identified at different imaging depths in vivo. Thus, in its current state, the IVPA/US system and catheter showcased in this thesis is ready to test this particular hypothesis; especially that safety of laser energy used on cells viability has been established [26]. In addition to that, we have shown that imaging of plaque lipids in-vivo with an IVPA/IVUS system was feasible. Further work is needed to robustly reject imaging artefacts in the near field imaging field, to highlight the presence of true lipid signals. Full characterization of artefacts generated as a result of blood swirls and tubing in a control setting may help improving the imaging modality.

We have also compared IVPA/US to two other clinical intravascular imaging modalities. These were in agreement when there was no lipid-rich plaque but in disagreement when these were present. We conjecture that this may be the result of NIRS/IVUS being more sensitive to necrotic cores rather than lipids, or that the pig model used is not as representative of human atherosclerosis as expected.

We also studied capability of dual wavelength imaging, however the noise level, the broad lasers' spectral linewidths and the digital processing used to enhance the images corrupted the threshold levels for lipid identifications. Thus for lipid-rich plaque imaging with IVPA, further effort in electronics and systems engineering are needed to reduce imaging noise levels emerging from the motors and the slip ring. In addition to that, perhaps a better suited transducer bandwidth, or a lower illumination wavelength range (930/960 nm) for spectroscopic imaging is worth investigating to increase the signal to noise ratio (SNR). This will require further research into catheter design. At this stage, IVPA of atherosclerotic plaque in tortuous arteries was shown to be feasible, however further developments in the hardware in receive is still needed. A catheter design and a fast processing routine to incorporate more information on plaques from multiple perspectives (e.g. mechanical, optical, thermal etc.) would enable total plaque characterization and better understanding of disease progression.

8.4 Differential phase photoacoustic imaging

Resolution is an important image characteristic to bear in mind when looking at an image. In PA imaging, the illumination source and the acoustic detector will determine the imaging resolution achieved. One of the easiest PA imaging setups to translate to the clinics relies on commercial, medical ultrasound detectors to which a broad illumination source is added. This type of setup is called limited-view photoacoustic

tomography and its resolution cell (lateral and axial) are determined by the acoustic detector.

Light absorption occurs at the molecular level, as can be elegantly visualized by super-resolution optical microscopy [27]. Optical-resolution PA microscopy probes tissue absorption at a resolution of approximately 1 μm, but this technique relies on a good quality optical focus which rapidly degrades at depths when light scattering disperses the excitation. Often, for deep tissue imaging, the acoustic resolution cell is hundreds of micrometers. In chapter 7, we have shown that if two spectrally different photo-acoustic sources were localized within one acoustic resolution cell, then they could be detected and separated with high accuracy (down to 1/20th of the point spread function) by using two wavelengths photoacoustic images. The method presented in Chapter 7 is a powerful tool to interpret and understand PA images.

This method is still at its infancy though. In this thesis we have solely evaluated capability of disentangling sources on phantoms. It is natural to ask oneself, what is the minimum separation distance which could be achieved? Super-localization accuracy will be limited by the system's noise, and the transducer's bandwidth. The PA source size will also be a parameter, since the frequency spectrum and source dimension are related in PA. Nonetheless, super-localization has been shown recently to be one of the routes to super-resolution [27-29]. This method, in the future, might go in the same direction, with the right application. These could span from a study on the different gut microbe interactions, to the study of targeted contrast agents attachment and detachment after drug delivery.

In sum, spectral PA methods have great potential for multiple cardiovascular applications spanning from super-localization and image enhancement methods to treatment monitoring and guidance. This thesis, though barely touching the tip of that potential, has in the least answered a short cohort of all the "what are we looking at?" questions. We have identified:

- ✓ *A transmural ablation lesion*
- ✓ *A healthy myocardium*
- ✓ *An ablation lesion gap*
- ✓ *A PA-enabled ablation catheter tip*
- ✓ *A lesion in the process of being formed*
- ✓ *Peri-adventitial lipids*
- ✓ *Atherosclerotic plaque-lipids*
- ✓ *….. more than two PA sources localized within a precise amount of unit distance.*

References

[1] P. Kruizinga, F. Mastik, N. De Jong, A. F. M. Van der Steen, and G. Van Soest, "**Ultrasound-guided photoacoustic image reconstruction,**" *Photons Plus Ultrasound: Imaging and Sensing 2012,* vol. **8223**, 2012.

[2] J. Glatz, N. C. Deliolanis, A. Buehler, D. Razansky, and V. Ntziachristos, "**Blind source unmixing in multi-spectral optoacoustic tomography,**" *Optics express,* vol. **19**, pp. 3175-3184, 2011.

[3] M. R. Tomaszewski, I. Quiros-Gonzalez, J. Joseph, and S. E. Bohndiek, "**Measurement of changes in blood oxygenation using multispectral optoacoustic tomography (msot) allows assessment of tumor development,**" *Photons Plus Ultrasound: Imaging and Sensing 2016,* vol. **9708**, 2016.

[4] F. M. Brochu, J. Joseph, M. Tomaszewski, and S. E. Bohndiek, "**Light fluence correction for quantitative determination of tissue absorption coefficient using multi-spectral optoacoustic tomography,**" *Opto-Acoustic Methods and Applications in Biophotonics Ii,* vol. **9539**, 2015.

[5] N. Dana, L. Di Biase, A. Natale, S. Emelianov, and R. Bouchard, "**In vitro photoacoustic visualization of myocardial ablation lesions,**" *Heart Rhythm,* vol. **11**, pp. 150-7, Jan 2014.

[6] G. A. Pang, E. Bay, X. DeÁN Ben, and D. Razansky, "**Three dimensional optoacoustic monitoring of lesion formation in real time during radiofrequency catheter ablation,**" *Journal of cardiovascular electrophysiology,* vol. **26**, pp. 339-345, 2015.

[7] Z. J. Guo, L. Li, and L. H. V. Wang, "**On the speckle-free nature of photoacoustic tomography,**" *Medical Physics,* vol. **36**, pp. 4084-4088, Sep 2009.

[8] M. Granier, P. F. Winum, M. Granier, P. Liaud, G. Cayla, P. Messner, J.-L. Pasquie, and I. Schuster, "**Real-time atrial wall imaging during radiofrequency ablation in a porcine model,**" *Heart Rhythm,* vol. **12**, pp. 1827-1835, 2015.

[9] M. Wright, E. Harks, S. Deladi, S. Fokkenrood, R. Brink, H. Belt, A. F. Kolen, D. Rankin, W. Stoffregen, D. A. Cockayne, J. Cefalu, and D. E. Haines, "**Characteristics of radiofrequency catheter ablation lesion formation in real time in vivo using near field ultrasound imaging,**" *JACC Clinical Electrophysiology,* vol. **4**, pp. 1062-1072, Aug 2018.

[10] G. Cismaru, S. Schiau, L. Muresan, R. Rosu, M. Puiu, G. Gusetu, D. Pop, and D. Zdrenghea, "**Intravascular pulmonary venous ultrasound imaging for catheter ablation of atrial fibrillation,**" *Expert Rev Med Devices,* vol. **14**, pp. 309-314, Apr 2017.

[11] E. Chu, J. M. Kalman, M. A. Kwasman, J. C. Y. Jue, P. J. Fitzgerald, L. M. Epstein, N. B. Schiller, P. G. Yock, and M. D. Lesh, "**Intracardiac echocardiography during radiofrequency catheter ablation of cardiac-arrhythmias in humans,**" *Journal of the American College of Cardiology,* vol. **24**, pp. 1351-1357, Nov 1 1994.

[12] J. F. Ren, F. E. Marchlinski, D. J. Callans, and E. S. Zado, "**Lesion imaging characteristics associated with successful ablation of appropriate sinus tachycardia: An intracardiac echocardiographic study,**" *Journal of the American College of Cardiology,* vol. **37**, pp. 128a-128a, Feb 2001.

[13] J. G. Mottley and J. G. Miller, "**Anisotropy of the ultrasonic backscatter of myocardial tissue: I. Theory and measurements in vitro,**" *J Acoust Soc Am,* vol. **83**, pp. 755-61, Feb 1988.

[14] D. N. Stephens, U. T. Truong, A. Nikoozadeh, Ö. Oralkan, C. H. Seo, J. Cannata, A. Dentinger, K. Thomenius, A. De La Rama, and T. Nguyen, "**First in vivo use of a capacitive micromachined ultrasound transducer array–based imaging and ablation catheter,**" *Journal of Ultrasound in Medicine,* vol. **31**, pp. 247-256, 2012.

[15] W. Shi, A. Anand, S. Sethuraman, S. W. Huang, H. Xie, H. Agarwal, P. Yan, J. Azevedo, J. Kruecker, G. Ng, V. Shamdasani, W. Pritchard, J. Karanian, and B. Wood, "**Monitoring of radiofrequency ablation with shear wave delay mapping,**" *2015 Ieee International Ultrasonics Symposium (Ius),* 2015.

[16] J. Grondin, E. Wan, A. Gambhir, H. Garan, and E. E. Konofagou, "**Intracardiac myocardial elastography in canines and humans in vivo,**" *Ieee Transactions on Ultrasonics Ferroelectrics and Frequency Control,* vol. **62**, pp. 337-349, Feb 2015.

[17] A. A. Schricker, G. G. Lalani, D. E. Krummen, and S. M. Narayan, "**Rotors as drivers of atrial fibrillation and targets for ablation,**" *Curr Cardiol Rep,* vol. **16**, p. 509, Aug 2014.

[18] N. de Groot, L. van der Does, A. Yaksh, E. Lanters, C. Teuwen, P. Knops, P. van de Woestijne, J. Bekkers, C. Kik, A. Bogers, and M. Allessie, "**Direct proof of endo-epicardial asynchrony of the atrial wall during atrial fibrillation in humans,**" *Circulation-Arrhythmia and Electrophysiology,* vol. **9**, May 2016.

[19] F. Ouyang, M. Antz, S. Ernst, H. Hachiya, H. Mavrakis, F. T. Deger, A. Schaumann, J. Chun, P. Falk, D. Hennig, X. Liu, D. Bansch, and K. H. Kuck, "**Recovered pulmonary vein conduction as a dominant factor for recurrent atrial tachyarrhythmias after complete circular isolation of the pulmonary veins: Lessons from double lasso technique,**" *Circulation,* vol. **111**, pp. 127-35, Jan 18 2005.

[20] M. Wu, K. Jansen, A. F. W. van der Steen, and G. van Soest, "**Specific imaging of atherosclerotic plaque lipids with two-wavelength intravascular photoacoustics,**" *Biomedical Optics Express,* vol. **6**, pp. 3276-3286, Sep 1 2015.

[21] K. Jansen, M. Wu, A. F. W. van der Steen, and G. van Soest, "**Lipid detection in atherosclerotic human coronaries by spectroscopic intravascular photoacoustic imaging,**" *Optics Express,* vol. **21**, pp. 21472-21484, Sep 9 2013.

[22] S. Sethuraman, S. R. Aglyamov, J. H. Amirian, R. W. Smalling, and S. Y. Emelianov, "**Development of a combined intravascular ultrasound and photoacoustic imaging system - art. No. 60860f,**" *Photons Plus Ultrasound: Imaging and Sensing 2006,* vol. **6086**, pp. F860-F860, 2006.

[23] M. U. Arabul, M. Heres, M. C. M. Rutten, M. R. van Sambeek, F. N. van de Vosse, and R. G. P. Lopata, "**Toward the detection of intraplaque hemorrhage in carotid artery lesions using photoacoustic imaging,**" *Journal of biomedical optics,* vol. **22**, p. 041010, 2016.

[24] B. Wang and S. Emelianov, "**Thermal intravascular photoacoustic imaging,**" *Biomed Opt Express,* vol. **2**, pp. 3072-8, Nov 1 2011.

[25] J. A. Schaar, C. L. de Korte, F. Mastik, R. Baldewsing, E. Regar, P. de Feyter, C. J. Slager, A. F. W. van der Steen, and P. W. Serruys, "**Intravascular palpography for high-risk vulnerable plaque assessment,**" *Herz,* vol. **28**, pp. 488-+, Sep 2003.

[26] T. Sowers, D. VanderLaan, A. Karpiouk, E. M. Donnelly, E. Smith, and S. Emelianov, "**Laser threshold and cell damage mechanism for intravascular photoacoustic imaging,**" *Lasers Surg Med,* Oct 10 2018.

[27] E. Betzig, G. H. Patterson, R. Sougrat, O. W. Lindwasser, S. Olenych, J. S. Bonifacino, M. W. Davidson, J. Lippincott-Schwartz, and H. F. Hess, "**Imaging intracellular fluorescent proteins at nanometer resolution,**" *Science,* vol. **313**, pp. 1642-1645, 2006.

[28] C. Errico, J. Pierre, S. Pezet, Y. Desailly, Z. Lenkei, O. Couture, and M. Tanter, "**Ultrafast ultrasound localization microscopy for deep super-resolution vascular imaging,**" *Nature,* vol. **527**, pp. 499-502, 2015.

[29] S. Vilov, B. Arnal, and E. Bossy, "**Overcoming the acoustic diffraction limit in photoacoustic imaging by the localization of flowing absorbers,**" *Opt Lett,* vol. **42**, pp. 4379-4382, Nov 1 2017.

Summary

According to the world health organization reports, ischemic heart disease and stroke, two cardiovascular diseases were the major global causes of death, in 2016, in middle and higher-income countries (15.2 million deaths globally); and this has been the case for the past 15 years. Cardiovascular diseases (CVDs) are often intertwined, and multifactorial from a clinical standpoint. It has, for instance, been shown that atherosclerosis may be a factor in atrial fibrillation development [1, 2]. Since CVDs often display specific biomarkers, photoacoustics may, one day, help in unravelling the condition's intricate web of causes and effects.

Many cardiovascular conditions that used to require surgery, such as coronary artery disease or atrial fibrillation, can now be treated using catheters. Minimally-invasive interventions rely heavily on imaging. What used to be in the direct line of sight of the cardiologist, uncovered to the eye, tangible and palpable, is now hidden behind layers of opaque tissue. Thus, without imaging and guidance, cardiologists would be totally incapacitated, completely blind. To start, navigating catheters through vessels located in the groin, neck or arm to reach the heart, is in itself quite challenging if not for fluoroscopic guidance. Secondly, identifying the treatment location requires a panoply of dedicated diagnostic devices identifying targeted abnormalities. Finally, monitoring and feedback of treatment requires yet other complex multi-purpose smart catheters. This reliance drives a billion-dollar industry of cardiac catheters and imaging technology. Indeed, besides cardiologist's experience, technology is the one essential element to the success of minimally-invasive surgery.

Photoacoustic imaging is an emerging technology with an exponentially growing number of published papers in biomedicine over the past decade. The photoacoustic principle describes the phenomenon through which acoustic waves are generated as a result of light absorption. Analysis of the signal generated for different illumination wavelengths and experimental configurations carries a wealth of information regarding tissue properties. This radiation-free technology can image tissue molecular composition at multiple scales, depending on the choice of instrumentation configuration.

Thus, we focused in this thesis on how photoacoustics could solve issues related to two particular cardiac interventions, namely Radiofrequency (RF) ablation for atrial fibrillation and percutaneous coronary intervention (PCI) for coronary atherosclerosis.

The first application we addressed, in the field of interventional electrophysiology, targets ablation of abnormal conductive tissue substrate. In RF ablation for atrial fibrillation the procedural success rate is varying between 60-70%; this staggering low number does even include patients given a redo surgery and following post-procedural anti-arrhythmic drug treatments. This low success rate is often attributed to inadequate treatment delivery. Ablation lesions are at the core of the procedure, whereby applying RF energy to tissue destroys its capability to conduct electrical potentials, blocking undesired conductive pathways. Lacking visual feedback on

delivered treatment, lesions often tend to lack transmurality or continuity. Occurrence of gaps in-between lesions (lesion ***dis****continuity*), and between lesion and epicardial surface (lesion ***sub****murality*) allows for electrical pathways to propagate defeating the purpose of the procedure.

In the first chapters of this thesis we developped a photoacoustic solution for RF ablation lesion monitoring of atrial fibrillation procedures with photoacoustic imaging. The solution comprised a modified ablation catheter for localized light delivery at the treated area, and an intracardiac echography probe for reception of the photoacoustic signals generated. In **Chapter 2**, we studied in depth photoacoustic characteristics of ablation lesions with respect to the surrounding tissue. We found that for a range of wavelengths greater than 600 nm (up to the maximum wavelength studied 1350 nm), light in the range of few miliJoules per cm^2 is sufficient to penetrate through the whole atrial tissue slab to generate photoacoustic signals. We also found that illumination at 640 nm generated best lesion-to-tissue- contrast for acoustic transducer center frequency of 7 MHz and 100% bandwidth. Finally, we determined an imaging method founded on the ratio of two photoacoustic images acquired at 790 nm and 930 nm to delineate and identify lesion with a diagnostic accuracy of 97%. Armed with this robust method of evaluating ablation lesions depth and lateral extents, we investigate in **Chapter 3**, methods of delivering light to the area treated. We designed and tested two photoacoustic-enabled RF ablation catheters for simultaneous ablation via RF current and illumination for photoacoustic imaging. We showed that in terms of illumination area and SNR a simple model comprising a single optical fiber at the center of the catheter is equivalent to a more complicated design of fibers surrounding the ablation electrode. In addition to that, we showed how the dual wavelength imaging method developed in chapter 2, solves clutter problems related to the catheter tip. Finally, with all devices ready at hand, within suitable sizes and configurations for ease of translation, we monitored RF ablation lesion formation. In **Chapter 4**, we showed feasibility of monitoring RF ablation lesion formation in real time in a readily translatable setup. The dual wavelength imaging method allowed us to successfully monitor lesion continuity and transmurality, in an ex-vivo porcine heart through circulating blood. Strong photoacoustic signals generated by blood, as well as by the catheter tip were correctly classified as non-lesion signals. This experiment also taught us that perhaps the more complex ablation catheter design with multiple optical fibers surrounding the tool shaft was after all a better design when taking into account experimental maneuverability and the resulting different catheter positions against the cardiac wall. In this first part, we conclude that photoacoustic imaging is a strong contender to solving the problems currently faced in interventional electrophysiology interventions for atrial fibrillation treatment.

The second interventional cardiology application we address in this thesis is percutaneous coronary intervention. Narrowing of coronary arteries impedes blood flow, and subsequently nutrition and oxygen provisions to cardiac tissue. This endangers the long term viability of the concerned myocardial areas. Rupture of 'vulnerable' atherosclerotic plaque can provoke myocardial infarcts. Thus, at the onset of the very first symptoms, such as chest pain, a PCI is performed; in narrowed vessel areas a stent is deployed maintaining the artery wall open to recover blood flow. Of imminent importance is the localization of the culprit area, which is believed to be a lipid-rich plaque. Photoacoustic imaging was previously shown to provide information on plaque lipid content. In **Chapter 5** we designed and tested a miniature intravascular photoacoustic imaging catheter for robustness and SNR. The design was oriented towards imaging plaque in a realistic and translatable setting. We optimized the catheter for light delivery, manageable flush parameters and robustness with reduced mechanical damage risks at the laser/catheter joint interface. We also showed capability of imaging atherosclerotic plaque through sheath and in water medium ex vivo. In **Chapter 6** we used the designed catheter to image the coronary arteries of an atherosclerotic pig model. We could successfully identify peri-adventitial lipids as well as lipid rich plaques in flushed D_2O as well as through blood. We compared the images to two other clinically-approved imaging modalities, namely NIRS and OCT and showed good accordance with OCT but surprisingly poor correlation to NIRS, a modality which theoretically also images tissue lipid content. The technology is promising, but more work is needed from the systems engineering point of view as well as from the imaging point of view in terms of photoacoustic spectral methods for better plaque vulnerability specificity.

Photoacoustic signals contain information that goes beyond tissue absorption. Processing and analysis of signals already enabled us to increase ablation lesion identification rates. We showed in **Chapter 7** that by manipulating signals of two photoacoustic acquisitions at two different wavelengths we can detect whether certain signal regions contain more than one photoacoustic source. We further showed that with a-priori knowledge of the expected photoacoustic sources absorption contrast ratio we can separate and co-localize them with high accuracy, down to the $1/20^{th}$ of the imaging system's beamformed lateral resolution. This processing technique holds promise in co-localization of targeted dual-modality contrast agents. If tweaked, this method could also be implemented to track and localize with high accuracy catheter tip position in an electrophysiology setup.

In a nutshell, this thesis describes novel photoacoustic imaging solutions to improve guidance and treatment of two specific minimally-invasive procedures in cardiology. Albeit, identification of tissue molecular markers with photoacoustic imaging will guide the future of disease pathways understanding and improve treatment strategies.

[1] K. Willeit and S. Kiechl, "**Atherosclerosis and atrial fibrillation–Two closely intertwined diseases**," *Atherosclerosis,* vol. **233**, pp. 679-681, 2014.

[2] S. A. Eryd, G. Östling, M. Rosvall, M. Persson, J. G. Smith, O. Melander*, et al.*, "**Carotid intima-media thickness is associated with incidence of hospitalized atrial fibrillation**," *Atherosclerosis,* vol. **233**, pp. 673-678, 2014.

Samenvatting

Volgens de Wereldgezondheidsorganisatie (WHO) was in 2016 hart- en vaatziekten wereldwijd doodsoorzaak nummer een in landen met een middel tot hoog bruto nationaal product. Het gaat om 15,2 miljoen doden wereldwijd en dit is de trend van de afgelopen 15 jaar. Hart- en vaatziekten hangen vaak samen met andere medische aandoeningen en klinisch gezien zijn er vaak meerdere aspecten die een rol spelen. Zo is bijvoorbeeld aangetoond dat aderverkalking een rol kan spelen bij de ontwikkeling van boezemfibrilleren. Met behulp van foto akoestische beeldvormingstechnieken is het mogelijk biologische signaalmoleculen weer te geven. Het is mogelijk dat we met behulp van deze signaalmoleculen dit complexe web van aandoeningen en oorzaak-gevolg kunnen ontrafelen.

Veel cardiovasculaire aandoeningen die vroeger een operatie vereisten, kunnen nu minimaal invasief worden behandeld met behulp van katheters. Deze minimaal-invasieve behandelingen zijn erg afhankelijk van beeldvormingstechnieken om deze procedures te begeleiden. Wat vroeger zichtbaar was voor de cardioloog, wat tastbaar was, is nu verborgen binnenin het lichaam. Dus zonder al deze beeldvorming zouden cardiologen niet kunnen handelen, hij zou volledig blind zijn. Angiografie, waarbij de hartslagaders in beeld worden gebracht door middel van röntgen en contrastmiddel, is nodig om de katheter op de juist plek te krijgen. Daarnaast moet de cardioloog de behandellocatie bepalen en daarna gecontroleerd hoe de behandeling verloopt en of deze succesvol is afgerond. Al deze stappen hebben beeldvormingstechnieken nodig om de cardioloog te ondersteunen. Dit heeft ervoor gezorgd dat er een miljarden-industrie is ontstaan rondom het ontwikkelen en produceren van nieuwe cardio-vasculaire katheters. Naast de expertise van de cardioloog zijn deze beeldvormings-katheters een essentieel onderdeel voor een succesvolle minimaal-invasieve interventie.

Foto akoestische beeldvorming is een opkomende technologie met een exponentieel groeiend aantal publicaties in biomedische wetenschappelijke tijdschriften in het afgelopen decennium. Het foto akoestische principe is gebaseerd op de omzetting van licht naar geluid, na absorptie van het licht. Door met verschillende golflengtes naar een weefsel te kijken, waarbij verschillende delen van het weefsel verschillende golflengtes absorberen, kan veel informatie worden vergaard over de eigenschappen van het weefsel. Deze stralingsvrije technologie kan de moleculaire samenstelling van weefsels op meerdere schalen afbeelden, afhankelijk van de keuze van de instrumentatie.

In dit proefschrift kijken we hoe we met behulp van foto akoestiek problemen omtrent twee verschillende cardiovasculair interventies kunnen verhelpen. Namelijk bij katheterablatie door middel van radiofrequente (RF) energie bij boezemfibrilleren en bij percutane coronaire interventie (PCI) voor aderverkalking, in de volksmond ook wel dotteren genoemd.

De eerste interventie waar we naar hebben gekeken op het gebied van interventie elektrofysiologie en richt zich op ablatie van abnormaal geleidend weefsel in het hart.

De slagingskans van zo'n procedure varieert tussen de 60 en 70 %. Dit lage aantal bevat ook patiënten die meermaals de procedure hebben ondergaan en daarnaast ook medicamenteuze behandeling krijgen voor hun boezemfibrilleren. Deze lage slagingskans wordt met name veroorzaakt door ontoereikende behandeling van het abnormaal geleidende weefsel. Tijdens radiofrequente ablatie wordt weefsel behandeld met als doel abnormale elektrische verbinding te onderbreken of om een structuur in het hart zodanig te wijzigen dat geen ritmestoornissen meer optreden. Het behandelde weefsel wordt een laesie genoemd. Bij gebrek aan visuele feedback op de geleverde behandeling, zijn laesies vaak niet transmuraal, over de gehele dikte van de hartwand, of zijn niet continue. Discontinuïteit en niet-transmurale laesies kunnen ervoor zorgen dat er alsnog abnormale geleiding en dus fibrillatie optreedt.

In de eerste paar hoofdstukken van dit proefschrift hebben we een methode ontwikkeld waarbij de laesies kunnen monitoren tijdens RF ablatie. De oplossing bevat een aangepaste ablatiekatheter waarbij lokaal licht wordt afgegeven op het behandelde gebied. Met een intracardiale tranducent die het gegenereerde foto akoestische geluid opvangt. In **Hoofdstuk 2** bestudeerden we de foto akoestische kenmerken van ablatielaesies in vergelijking met het omliggende, onbehandelde weefsel. We vonden dat vanaf 600 nm, tot en met de maximale onderzochte golflengte van 1350nm, een licht energie van een paar milli-joules per vierkante centimeter voldoende is om de volledige dikte van de boezem te kunnen bekijken. Daarnaast vonden we ook dat het foto akoestische signaal het meeste contrast geeft bij 640nm, in combinatie met de door ons gekozen transducent met een fundamentele frequentie van 7 MHz en een bandbreedte van 100%. Tenslotte hebben een beeldvormings-methode ontwikkeld voor het bepalen van de grootte van de laesie, deze is gebaseerd op de verhouding tussen de beelden bij 790nm en 930nm. We kunnen hiermee een laesie diagnosticeren met een nauwkeurigheid van 97%. Gewapend met deze robuuste methode om de diepte en de laterale omvang van ablatie-laesies te evalueren, onderzoeken we in **Hoofdstuk 3** methoden voor het afgeven van licht aan het behandelde gebied. We ontwierpen en testten twee ablatiekatheters voor gelijktijdige ablatie via RF-stroom en verlichting voor foto akoestische beeldvorming. We toonden aan de ons simpele ontwerp, waarbij we een enkele optische fiber door het midden van de ablatiekatheter plaatsen, net zo goed werkt als een complexer ontwerp waarbij meerdere fibers rondom de katheter worden geplaatst. Daarnaast laten we zien hoe de tweevoudige golflengtemethode die in hoofdstuk 2 is ontwikkeld, problemen met ruis met betrekking tot de kathetertip oplost. In **Hoofdstuk 4** lieten we de haalbaarheid zien van het direct volgen van RF-ablatie laesievorming in een naar de kliniek vertaalbare opstelling. De beeldvormingsmethode met dubbele golflengte stelde ons in staat de continuïteit van de laesie en transmuraliteit met succes te volgen, in een ex-vivo hart van een varken met circulerend bloed. Sterke foto akoestische signalen gegenereerd door bloed, evenals door de kathetertip werden correct geclassificeerd als niet-laesiesignalen. Dit experiment leerde ons ook dat misschien

het complexere ontwerp van de ablatiekatheter met meerdere optische vezels rondom de katheter toch een beter ontwerp was wanneer rekening word gehouden met manoeuvreerbaarheid en de resulterende verschillende katheterposities tegen de hartwand. In dit eerste deel concluderen we dat foto akoestische beeldvorming een goede kandidaat is voor het oplossen van de problemen die zich momenteel voordoen bij elektrofysiologische interventies voor atriale fibrillatiebehandeling.

De tweede interventionele cardiologische toepassing die we in dit proefschrift behandelen, is percutane coronaire interventie (PCI). In deze procedure wordt de vernauwing van kransslagaders, aderverkalking, verholpen. Deze vernauwing zorgt voor een verminderde doorbloeding en waardoor de voedings- en zuurstofvoorzieningen aan hartweefsel ontoereikend is. Op lange termijn brengt dit de gezondheid van het betrokken myocardiaal gebied in gevaar. Deze aderverkalking kan loskomen van de vaatwand of breken met als gevolg een hartinfarct. Wanneer hier symptomen van zijn, zoals pijn op de borst, wordt zo'n PCI uitgevoerd, er wordt dan een stent in het vernauwde bloedvat geplaatst, waarmee de slagader wordt opgehouden en doorbloeding wordt hersteld. Tijdens deze procedure is de locatie waar de stent wordt geplaatst van beland, het meest risicovolle gebied wordt behandeld. Er wordt vanuit gegaan dat dit het gebied is waar de plaque (aderverkalking) lipide rijk is. Met behulp van foto akoestische beeldvorming kan het lipide gehalte van de plaque worden bepaald. In **Hoofdstuk 5** hebben we een intravasculaire foto akoestische beeldvormingskatheter ontworpen en getest voor robuustheid en signaal ruis verhouding (SNR). Het ontwerp is zo gemaakt dat het zo realistische mogelijk en zoveel mogelijk op de klinische toepassing lijkt voor beeldvorming van plaque. We hebben de katheter geoptimaliseerd voor klinische toepasbaarheid en robuustheid met beperkte mechanische schade aan de laser / katheter-interface. We toonden aan dat we met deze katheter in een omhulsel, nodig voor klinische doeleinden, foto akoestische beeldvorming kunnen doen in een ex vivo kransslagader. In **Hoofdstuk 6** hebben we de ontworpen katheter gebruikt om de kransslagaders van een atherosclerotisch varkensmodel in beeld te brengen. We konden zowel peri-adventitiële lipiden als lipide-rijke plaques in een met D_2O doorgespoelde kransslagader en in een doorbloedde kransslagader met succes in beeld brengen. We vergeleken de beelden met twee beeldvormingsmodaliteiten die in de kliniek worden gebruikt, namelijk NIRS en OCT. De resultaten lieten een goede overeenkomst zien met OCT, maar een slechte correlatie met NIRS, want die theoretisch het necrotische kern van het weefsel visualiseert. De technologie is veelbelovend, maar voor een klinische toepassing is nog veel werk nodig om de katheter van een prototype naar een product te brengen en daarnaast is er ook nog werk nodig met betrekking tot foto akoestische analyse methoden voor een betere specificatie van de kwetsbaarheid van plaque.

Foto akoestische signalen bevatten meer informatie dan alleen de absorptie van weefsel. Verwerking en analyse van signalen hebben ons al in staat gesteld om robuuste ablatie-laesie-identificatie te bewerkstelligen. In **Hoofdstuk 7** toonden we

aan dat we door het manipuleren van signalen van twee foto akoestische acquisities bij twee verschillende golflengten kunnen detecteren of bepaalde signaalgebieden meer dan één foto akoestische bron bevatten. We toonden verder aan dat we met voorkennis van de verwachte absorptie contrast van de foto akoestische bronnen, we de bronnen kunnen scheiden en co-lokaliseren met een hoge nauwkeurigheid. Nauwkeurig tot aan de 1/20ste van de laterale resolutie van het beeldvormingssysteem. Deze verwerkingstechniek is veelbelovend in co-lokalisatie van gerichte contrastmiddelen met twee modaliteiten. Indien aangepast, zou deze methode ook kunnen worden geïmplementeerd om zeer nauwkeurig de kathetertippositie in een elektrofysiologische opstelling te volgen en te lokaliseren.

In een notendop beschrijft dit proefschrift nieuwe foto akoestische beeldvormingsoplossingen om de begeleiding en behandeling van twee specifieke minimaal invasieve procedures in de cardiologie te verbeteren. Wellicht zal de identificatie van moleculaire weefselmarkers met foto akoestische beeldvorming de toekomst van ziektetrajecten inzicht verschaffen en behandelingsstrategieën verbeteren.

About the author

Sophinese Iskander-Rizk was born in Marrakech, Morocco (مراكش، المغرب) on June 2nd 1988. After completion of her secondary education in Morocco she moved in 2006 to Cairo to pursue her undergraduate studies at the American University in Cairo (AUC), Egypt. She joined, in Cairo, multiple student associations such as AISEC, Cairo International Model United Nations (CIMUN) and the robotics club. Undergraduate meandering led to the obtaining of a Bachelor of electronics engineering in 2011, granting her the title of electronics engineer and much knowledge about power gating of VLSI circuits for low power applications. In 2013, she obtained her Master degree in biomedical engineering from Delft university of technology, with a thesis exploring the skin-electrode interface to improve contact and signal to noise ratio (SNR) of dry electro-encephalogram (EEG) headsets. Following her curiosity and passion to take on new topics and challenges, she then joined in 2014 the biomedical engineering department at Erasmus MC, university medical center in Rotterdam to pursue a doctoral degree on photoacoustic imaging. The work described in this thesis is the result of the research conducted along this pursuit.

Publications

Peer reviewed

Iskander-Rizk, S., Kruizinga, P., Springeling, G., Vos, H.J., van der Steen, A.F. and van Soest, G., 2017. Photoacoustic imaging of sub-diffraction objects with spectral contrast. Optics letters, 42(2), pp.191-194.

Wu, M., Springeling, G., Lovrak, M., Mastik, F., **Iskander-Rizk, S.**, Wang, T., Van Beusekom, H.M., Van Der Steen, A.F.W. and Van Soest, G., 2017. Real-time volumetric lipid imaging in vivo by intravascular photoacoustics at 20 frames per second. Biomedical optics express, 8(2), pp.943-953.

Iskander-Rizk, S., Kruizinga, P., van der Steen, A.F. and van Soest, G., 2018. Spectroscopic photoacoustic imaging of radiofrequency ablation in the left atrium. Biomedical optics express, 9(3), pp.1309-1322.

Iskander-Rizk, S., van der Steen, A.F. and van Soest, G., 2019. Photoacoustic imaging for guidance of interventions in cardiovascular medicine. Physics in Medicine & Biology.

Iskander-Rizk, S., Wu, M., Springeling, S., van Beusekom, H.M.M., Mastik,F., Te Lintel Hekkert, M., Beurskens, R.H.S, Hoogendoorn, A., Hartman, E.M.J, van der Steen, A.F.W., Wentzel, J.J. and van Soest, G., 2019. In vivo intravascular photoacoustic imaging of lipid plaque in coronary atherosclerosis. EuroInterventions.

Submitted for publication

Iskander-Rizk, S., Kruizinga, Beurskens, R.H., Springeling, G., Mastik, F., de Groot, N.M., Knops, P., van der Steen, A.F. and van Soest, G., 2019. Real-time photoacoustic assessment of radiofrequency ablation lesion formation in the left atrium.

Conference proceedings

Iskander-Rizk, S., Wu, M., Springeling, G., Mastik, F., Beurskens, R.H., van der Steen, A.F. and van Soest, G., 2018, February. Catheter design optimization for practical intravascular photoacoustic imaging (IVPA) of vulnerable plaques. In Diagnostic and Therapeutic Applications of Light in Cardiology 2018 (Vol. 10471, p. 1047111). International Society for Optics and Photonics.

Iskander-Rizk, S., Springeling, G., Kruizinga, P., Beurskens, R.H., van der Steen, A.F. and van Soest, G., 2018, October. Photoacoustic-Enabled RF Ablation Catheters for Lesion Monitoring. In 2018 IEEE International Ultrasonics Symposium (IUS) (pp. 1-4). IEEE.

Iskander-Rizk, S., Kruizinga, P., van der Steen, A.F. and van Soest, G., 2015, October. Differential phase photoacoustic imaging for high-resolution position sensing. In 2015 IEEE International Ultrasonics Symposium (IUS) (pp. 1-4). IEEE.

Phd portfolio

Courses	Year	ECTs
Advanced Ultrasound Imaging, Danish Technical University, Copenhagen, Denmark	2015	2,50
Cardiovascular imaging and diagnostics, Rotterdam, the Netherlands	2015	1,50
Verasonics course, Taipei, Taiwan	2015	0,20
Biomedical Photoacoustics: from bench to bedside, IEEE, Taipei Taiwan	2015	0,20
English biomedical writing and communication, Rotterdam, the Netherlands	2015	4,00
Tissue optics, SPIE, San Francisco, United States of America	2016	0,15
Arrhythmia research methodology	2016	1,50
Time-domain Ultrasound Simulation in Biological Tissue using k-Wave, IEEE, Washington, United states of America	2017	0,20
Medical ultrasound transducers, IEEE, Kobe, Japan	2018	0,20
Motion Estimation Algorithms in Ultrasound Imaging: Principles and Hands-On Development, IEEE, Kobe, Japan	2018	0,20
Pathophysiology of ischemic heart disease, Rotterdam, the Netherlands	2018	1,50

Workshops and Seminars		
COEUR PhD day	2014	0,60
COEUR PhD day	2015	0,60
Workshop: Photoshop and Illustrator CS5, Rotterdam, the Netherlands	2015	0,30
The role of biomarkers in the pathophysiology of atrial fibrillation, Rotterdam, the netherlands	2015	0,40
iMIT meeting, Delft, the Netherlands (Oral)	2015	0,60
NVMU spring meeting, Eindhoven, the Netherlands	2015	0,15
NVMU spring meeting, Rotterdam, the Netherlands (Oral)	2016	0,55
NVMU autumn meeting, Nijmegen, the Netherlands	2016	0,15
NVMU spring meeting, Delft, the Netherlands	2017	0,15
NVMU autumn meeting, Enschede, the Netherlands	2017	0,15
NVMU spring meeting, Eindhoven, the Netherlands	2018	0,15
iMIT meeting, Rotterdam, the Netherlands (Oral)	2017	0,60
iMIT meeting, Delft, the Netherlands (Oral)	2018	0,60
Solving the mysteries of atrial fibrillation: from basic science to clinical practice	2018	0,40

Symposia and congresses		
Symposium: New imaging strategies for the detection of atherosclerosis, Rotterdam, the Netherlands	2014	0,20
Symposium: Imaging of Cardiac Arrhythmias, Rotterdam, the Netherlands	2014	0,20
Optics in cardiology, Rotterdam, the Netherlands	2015	0,60
Artimino conference, Helsinborg, Sweden (Oral)	2015	1,90
IEEE International ultrasonic symposium, Taipei, Taiwan (Oral)	2015	1,70
BIOS, SPIE photonics West, San Francisco, United States of America (Oral)	2016	2,30
Design of medical devices-DMD/SMIT, Delft, the Netherlands	2016	0,60
International conference on Ultrasonic Biomedical Microscanning, kralendijk, Bonaire, the Netherlands (Oral)	2016	1,70
Gordon conference on lasers in medicine and biology, Mt Snow, West Dover, VT United States of America (Posters x2)	2016	2,40
BIOS, SPIE photonics West, San Francisco, United States of America (Oral)	2017	2,30
Design of medical devices-DMD/SMIT, Delft, the Netherlands (Oral)	2017	1,10
Optics in cardiology, Rotterdam, The Netherlands (Poster)	2017	0,90
IEEE International ultrasonic symposium, Washington,United States of America (Oral)	2017	1,70
BIOS, SPIE photonics West, San Francisco, United States of America (Poster)	2018	2,10
Optics in cardiology, Zurich, Switzerland (Oral, Invited)	2018	1,10
IEEE International ultrasonic symposium, Kobe, Japan (Oral, Chair)	2018	1,70
BIOS, SPIE photonics West, San Francisco, United States of America (Oral)	2019	2,30
	Total	**42,35**